ABSTRACT

Title of dissertation: CHARACTERIZING ATMOSPHERIC TURBULENCE WITH CONVENTIONAL AND PLENOPTIC APPROACHES

Jonathan Ko, Doctor of Philosophy, 2017

Dissertation directed by: Professor Christopher C. Davis
ECE Department, UMCP

Atmospheric turbulence is a phenomenon of interest in many scientific fields. The direct effects of atmospheric turbulence can be observed in everyday situations. The twinkling of stars is an indicator of weak atmospheric turbulence while the shimmering of objects above a hot surface is an indicator of strong atmospheric turbulence. The effects of atmospheric turbulence are generally considered a nuisance to optical applications. Image blurring effects are often present when observing distant objects through atmospheric turbulence. Applications that require maintaining the coherence of a laser beam, such as in free space optical communication, suffer from poor link quality in the presence of atmospheric turbulence.

Attempts to compensate for the effects of atmospheric turbulence have varied in effectiveness. In astronomical applications, weak cases of atmospheric turbulence have been successfully compensated with the use of a Shack-Hartmann wavefront sensor combined with adaptive optics. Software techniques such as “Lucky Imaging” can be useful when clear images briefly appear through the presence of weak turbulence. However, stronger cases of atmospheric turbulence often found in

horizontal or slant paths near the Earth's surface present a much more challenging situation to counteract.

This thesis focuses primarily on the effects of strong or "deep" atmospheric turbulence. The process of compensating for the effects of strong atmospheric turbulence begins with being able to characterize it effectively. A scintillometer measures the scintillation in the intensity of a light source to determine the strength of current turbulence conditions. Thermal fluctuation measurements can also be used to derive the strength of atmospheric turbulence. Experimental results are presented of a developed large aperture scintillometer, thermal probe atmospheric characterization device, and a transmissometer. While these tools are effective in characterizing atmospheric turbulence, they do not provide for a means to correct for turbulence effects. To compensate for the effects of atmospheric turbulence, the development of the Plenoptic Sensor is presented as a wavefront sensor capable of handling strong turbulence conditions. Theoretical and experimental results are presented to demonstrate the performance of the Plenoptic Sensor, specifically in how it leads to adaptive optics algorithms that can rapidly correct for the effects of turbulence.

CHARACTERIZING ATMOSPHERIC TURBULENCE WITH CONVENTIONAL AND PLENOPTIC APPROACHES

by

Jonathan Ko

Dissertation submitted to the Faculty of the Graduate School of the
University of Maryland, College Park in partial fulfillment
of the requirements for the degree of
Doctor of Philosophy
2017

Advisory Committee:

Professor Christopher C. Davis, Chair
Professor Douglas Currie
Professor Julius Goldhar
Professor Phillip Sprangle
Dr. Antonio Ting

Acknowledgments:

My thesis would not have been possible without the guidance and contributions of many individuals. I am very grateful to everyone involved and feel the need to acknowledge them.

I want to thank Professor Christopher Davis for being a wonderful advisor and mentor. Professor Davis mentored me while I was an undergraduate student at the University of Maryland and inspired me to pursue higher levels of education. His genuine passion in a variety of research topics energized my interest in further studying atmospheric turbulence and its effect on wave propagation. I am extremely grateful for the motivation and ever-present support provided by Professor Davis. His positive influence is something I will certainly carry with me onwards.

I want to thank everyone in the Maryland Optics Group for their support throughout the years. My colleagues Chensheng Wu, John Rzasa, William Nelson, Thomas Shen, and Daniel Paulson have always been available at any moment to provide advice and lend assistance. I feel very lucky to have worked with such a great group of people.

I want to thank the Joint Technology Office (JTO) and the Office of Naval Research (ONR) for their funding. Their belief in our research has made it possible for us to conduct experiments in both indoor lab environments, as well as in large scale outdoor environments at a variety of locations critical to our needs.

I want to thank the Army Research Lab (ARL) for their support and funding. The knowledge I gained through interactions with their researchers and experimental systems provided much insight for the direction of my work.

I want to thank Professor Larry Andrews, Professor Ron Phillips, Bob Crabbs and the rest of the UCF Wave Propagation Research Group for their continual support. Their combined knowledge, access to amazing experimental facilities, and constant willingness to provide hands-on assistance was crucial in enabling us to pursue our goals.

I want to especially thank my family. Their encouragement and motivation throughout my entire life generated an environment that fostered my personal and academic growth. I am very grateful for having their love in my life.

Publications:

- Jonathan Ko and Christopher C. Davis, "Comparison of the plenoptic sensor and the Shack- Hartmann Sensor," Appl. Opt. 56, 3689-3698 (2017).
- Chensheng Wu, Jonathan Ko, and Christopher C. Davis, "Plenoptic mapping for imaging and retrieval of the complex field amplitude of a laser beam," Opt. Express 24, 29852-29871 (2016).
- Chensheng Wu, Jonathan Ko, and Christopher C. Davis, "Using a plenoptic sensor to reconstruct vortex phase structures," Opt. Lett. 41, 3169-3172 (2016).
- Jonathan Ko, Chensheng Wu, Christopher C. Davis, "Implementation of a rapid correction algorithm for adaptive optics using a plenoptic sensor," Proc. SPIE 9979, Laser Communication and Propagation through the Atmosphere and Oceans V, 99790O (2016).
- Chensheng Wu, Jonathan Ko, Christopher C. Davis, "Complex wavefront sensing with a plenoptic sensor," Proc. SPIE 9979, Laser Communication and Propagation through the Atmosphere and Oceans V, 99790Y (2016).
- Chensheng Wu, Jonathan Ko, Christopher C. Davis, "Imaging through water turbulence with a plenoptic sensor," Proc. SPIE 9979, Laser Communication and Propagation through the Atmosphere and Oceans V, 99790Z (2016).
- Jonathan Ko, Chensheng Wu, Christopher C. Davis, "An adaptive optics approach for laser beam correction in turbulence utilizing a modified plenoptic camera," Proc. SPIE 9614, Laser Communication and Propagation through the Atmosphere and Oceans IV, 96140I (2015).

- Chensheng Wu, Jonathan Ko, and Christopher C. Davis, "Determining the phase and amplitude distortion of a wavefront using a plenoptic sensor," J. Opt. Soc. Am. A 32, 964-978 (2015).
- Chensheng Wu, Jonathan Ko, Christopher C. Davis, "Entropy studies on beam distortion by atmospheric turbulence," Proc. SPIE 9614, Laser Communication and Propagation through the Atmosphere and Oceans IV, 96140F (2015).
- Chensheng Wu, Jonathan Ko, and Christopher C. Davis, "Imaging through turbulence using a plenoptic sensor," Proc. SPIE 9614, Laser Communication and Propagation through the Atmosphere and Oceans IV, 961405 (2015).
- Chensheng Wu, Jonathan Ko, and Christopher Davis, "Object recognition through turbulence with a modified plenoptic camera," Proc. SPIE 9354, Free-Space Laser Communication and Atmospheric Propagation XXVII, 93540V (2015).
- Jonathan Ko, Chensheng Wu, and Christopher C. Davis, "Intelligent correction of laser beam propagation through turbulent media using adaptive optics," Proc. SPIE 9224, Laser Communication and Propagation through the Atmosphere and Oceans III, 92240E (2014).
- Chensheng Wu, Jonathan Ko, William Nelson, and Christopher C. Davis, "Phase and amplitude wave front sensing and reconstruction with a modified plenoptic camera," Proc. SPIE 9224, Laser Communication and Propagation through the Atmosphere and Oceans III, 92240G (2014).

- Chensheng Wu, William Nelson, Jonathan Ko, and Christopher C. Davis, "Experimental results on the enhanced backscatter phenomenon and its dynamics," Proc. SPIE 9224, Laser Communication and Propagation through the Atmosphere and Oceans III, 922412 (2014).

Table of Contents

1) Atmospheric Turbulence 1
1.1) Scintillation 2
1.2) Beam Wander 7
1.3) Beam spreading/break up 9
2) Plenoptic Wavefront Sensor 12
2.1) Basic structure and design 14
2.2) Wavefront Reconstruction 18
2.2.1) Checkerboard Reconstruction Algorithm 19
2.2.2) Graph Reconstruction Algorithm 23
2.3) Comparison with Shack-Hartmann Sensor 29
2.3.1) Hardware comparison 30
2.3.1.1) Shack-Hartmann Sensor 30
2.3.1.2) Plenoptic Sensor 32
2.3.2) Gradient Information Comparison: Tilt sensitivity, tilt dynamic range, gradient sample size 35
2.3.2.1) Scenario #1 38
2.3.2.2) Scenario #2 40
2.3.3) Sample Wavefront Scenarios 42
2.3.4) Indoor Experimental Images 47
2.3.5) Outdoor Experimental Images 52
3) Experimental Results 59
3.1) Indoor lab experiments 59
3.1.1) Adaptive optics correction of static distortions 61
3.1.2) Adaptive optics correction of live turbulence 69
3.2) Outdoor experimental results 80
3.2.1) Initial device calibration 80
3.2.1a) Large Aperture Scintillometer 80
3.2.1b) RTD Probe System 87
3.2.1c) Plenoptic Sensor 95
3.2.1d) Transmissometer 101

3.3) Field deployment of MOG equipment..... 105
4) Conclusions 113

List of Figures

Figure 1.1: Scintillation index versus Rytov variance (experimental data) [2]. 5
Figure 1.2: Long term vs short term beam radius [2]. 9
Figure 2.1: Extracting image depth from pinholes [9]. 13
Figure 2.2: Diagram of the Plenoptic Sensor. 15
Figure 2.3: Ray tracing diagram of Plenoptic Sensor. 17
Figure 2.4: Plenoptic image of undistorted beam with checkerboard units overlaid.. 20
Figure 2.5: Wavefront gradient information from checkerboard units. 21
Figure 2.6: Minimum degree spanning tree of deformable mirror actuators. 24
Figure 2.7: Actuator tree overlaid onto plenoptic image of undistorted beam. 25
Figure 2.8: Plenoptic image of a distorted beam with actuator tree overlaid. 26
Figure 2.9: Selected edges between nodes and associated phase map. 27
Fig. 2.10 Shack-Hartmann sensor operation. 31
Figure 2.11: Plenoptic Sensor diagram. 32
Figure 2.12 Plenoptic Sensor operation [48]. 34
Figure 2.13: Significant wavefront distortion scenario [48]. 44
Figure 2.14: Double beam scenario [48]. 46
Figure 2.15: Shack-Hartmann sensor images (a) Beam 1; (b) Beam 2; (c) Beam 1 and 2; (d) Beam 1 with vortex phase plate [48]. 47
Figure 2.16: (a) Plenoptic image of double beam with small tilt; (b) Plenoptic image of double beam with large tilt; (c) Plenoptic image of double beam with large tilt and phase plate; (d) vortex phase plate layout [48]. 50
Figure 2.17: Shack-Hartmann sensor images under: (a) weak turbulence; (b) medium turbulence [48]. 53
Figure 2.18: Shack-Hartmann sensor image under strong atmospheric turbulence [48]. 54
Figure 2.19: Plenoptic images under: (a) weak turbulence; (b) strong turbulence [48]. 55
Figure 2.20: Zoomed in Plenoptic image from Figure 2.19(b) highlighting the geometrically overlapped patches of light [48]. 57
Figure 3.1.1: Diagram of indoor experimental setup. 59
Figure 3.1.2: OKO Technologies deformable mirror hardware. 60

Figure 3.1.3: Actuator map of OKO 37-channel deformable mirror. 61
Figure 3.1.4: Plenoptic images of different wavefront deformations. 63
Figure 3.1.5: Plenoptic image and reconstruction of defocus deformation. 64
Figure 3.1.6: Plenoptic image and reconstruction of trefoil deformation. 65
Figure 3.1.7: Tree reconstruction algorithm for trefoil deformation. 68
Figure 3.1.8: Experimental layout for real-time AO correction. 70
Figure 3.1.9: Adaptive optics flowchart showing 1 cycle of the closed-loop correction. 71
Figure 3.1.10: Closed loop adaptive optics turned off. 72
Figure 3.1.11: Closed loop adaptive optics turned on. 73
Figure 3.1.12: Adaptive optics system operating under 175 F conditions. 75
Figure 3.1.13: Adaptive optics system operating under 250 F conditions. 76
Figure 3.1.14: Adaptive optics system operating under 325 F conditions. 77
Figure 3.2.1: LAS Transmitter undergoing testing. 80
Figure 3.2.2: LAS Transmitter and Receiver undergoing testing. 81
Figure 3.2.3: MOG Large Aperture Scintillometer testing in Kim Building parking lot. 83
Figure 3.2.4: MOG Large Aperture Scintillometer testing on AV Williams Rooftop. 83
Figure 3.2.5: Large Aperture Scintillometer data on AV Williams on rooftop. 84
Figure 3.2.6: MOG Large Aperture Scintillometer testing at the US Naval Academy. 85
Figure 3.2.7: Comparison of MOG LAS with a Kipp and Zonen LAS. 86
Figure 3.2.8: Prototype RTD probe system for $CT2$ measurements. 87
Figure 3.2.9: 2/3 Power Law of R for $CT2$. 88
Figure 3.2.10: Weatherized RTD $CT2$ device. 89
Figure 3.2.11a: Outdoor verification of RTD $CT2$ devices. 91
Figure 3.2.11b: BLS900 Transmitter and RTD Device #2. 91
Figure 3.2.12: $Cn2$ values from Scintec Scintillometers and RTD $CT2$ devices. 92
Figure 3.2.13: Testing the Plenoptic Sensor on the TISTEF range. 96
Figure 3.2.14: 15 continuous Plenoptic images. 96
Figure 3.2.15: Beam intensity profile from Plenoptic images in Figure 3.2.14. 97

Figure 3.2.16: Normalized beam intensity of each frame from Figure 3.2.15. 98
Figure 3.2.17: Angle of arrival data for Plenoptic images obtained in Figure 3.2.14. 99
Figure 3.2.18: Wavefront reconstruction from Plenoptic images. 100
Figure 3.2.19: Basic principle of a transmissometer..... 101
Figure 3.2.20: Transmissometer testing at the Shuttle Landing Facility. 102
Figure 3.2.21: MOG Transmissometer + AWI Visibility Sensor. 103
Figure 3.2.22: Atmospheric attenuation coefficient data. 104
Figure 3.2.21: Visibility readings from visibility sensor, sun photometer, and particle counters. 105
Figure 3.3.1: MOG LED Large Aperture Scintillometer. 106
Figure 3.3.2: Plenoptic Sensor testing on SLF. 107
Figure 3.3.3: RTD and LED scintillometer results. 108
Figure 3.3.4: Comparison of $Cn2$ data from 2/2/2017..... 109
Figure 3.3.5: Plenoptic Sensor $Cn2$ data from 2/2/2017. 110
Figure 3.3.6: Closer look at Plenoptic Sensor $Cn2$ data at 8:20 pm. 111

List of Tables

Table 2.1: Hardware utilized in Scenario 1 38

Table 2.2: Performance characteristics of Scenario 1..... 39

Table 2.3: Hardware utilized in Scenario 2 40

Table 2.4: Hardware utilized in Scenario 2 41

Table 3.1: Coordinates of the 37 actuators on the OKO deformable mirror. 62

Table 3.2: Comparison of applied deformable mirror voltages to reconstructed voltages for a trefoil deformation. 67

Table 3.3: Statistics of adaptive optics operation. 78

1) Atmospheric Turbulence

Atmospheric turbulence is a naturally occurring phenomenon that results from small spatial and temporal variations in atmospheric temperature. These small variations in temperature are often on the order of <1 Celsius and cause small variations in the density of the atmosphere. The inhomogeneity of the density of the atmosphere correspondingly results in small variations in the index of refraction. Although the fluctuations in index of refraction are on the order of 10^{-6}, the accumulation of these fluctuations over a path length can significantly affect the propagation of light [1].

The small variations in atmospheric temperature also give rise to small regions of turbulent airflow. The random changes in wind velocity cause the pockets of higher and lower density air to move around. Localized unstable air masses are referred to as turbulent eddies, or simply eddies, and can be characterized by their inner and outer scale [2]. The inner scale l_0 defines the smallest eddy size while the outer scale L_0 defines the largest eddy size. Eddies bounded by the inner scale and outer scale form the inertial subrange [2]. Eddies that are smaller than the inner scale form the viscous dissipation range, where the turbulent eddies disappear and their energy is dissipated as heat. Simply speaking, the eddy size reflects areas where the index of refraction can be considered uniform. These eddies can analogously be thought of as small lenses in the atmosphere [1].

Adaptive optics primarily aims to correct for three main effects of atmospheric turbulence [1][2]. One effect is the presence of intensity scintillation which is commonly observed in the twinkling of stars. The intensity scintillation is

due to self-interfering portions of a wavefront when their optical paths are altered by the small differences in index of refraction and then overlap. A second effect is the presence of beam wander. The average changes in index of refraction along the optical path causes an object to wander about an average position. The third effect is the presence of beam spreading or beam breakup. These are higher order phase aberrations that cause large phase distortions and can reduce the coherence of a beam. All three of these effects are a result of refractive index fluctuations [2]. Other effects such as aerosol scattering and absorption are generally left out of the adaptive optics discussion because they are not able to be corrected for using traditional adaptive optics techniques and their impact is generally limited to optical attenuation. [2]

1.1) Scintillation

Overview

Scintillation is one of the primary areas of concern when dealing with light propagation through atmospheric turbulence. Scintillation is commonly referred to as the irradiance fluctuations of an optical source. The effect of scintillation can be observed influencing both incoherent light sources, such as the twinkling of stars, as well as coherent light sources, such as the intensity fluctuation at the receiver end of a laser beam. The random redistribution of light within the profile of a beam poses a problem for optical communication systems by temporarily reducing the overall signal strength. The random areas of constructive and destructive interference in the beam cross section are a result of the phase changes in the wavefront caused by the fluctuating index of refraction in the atmosphere. Scintillation effects occur with a

temporal frequency starting around 10 hertz all the way up to a few hundred hertz [1][2]. Taylors Frozen Turbulence Hypothesis dictates that the turbulent eddies can be seen as a frozen field in which the local changes inside each eddy are negligible. The wind carries this frozen field past the sensor at timescales on the order of milliseconds which gives adaptive optics a short but not impossible timeframe to correct for the wavefront distortions [3].

Scintillation of an optical source can be measured by simply measuring the normalized intensity variance. The intensity collected by an aperture will increase in variance as the strength of atmospheric turbulence increases. The normalized intensity variance σ_I^2 , also known as the scintillation index, can be defined as:

$$\sigma_I^2 = \frac{\langle I^2 \rangle - \langle I \rangle^2}{\langle I \rangle^2} \tag{1}$$

where $\langle I^2 \rangle - \langle I \rangle^2$ refers to the variance of the intensity *I* and $\langle I \rangle^2$ is the mean squared of *I*. The scintillation index σ_I^2 can be related to the strength of turbulence conditions [2][4]. For a value of σ_I^2 which is less than about 0.3, also known as the weak fluctuations regime, the value of σ_I^2 is proportional to the Rytov variance σ_R^2. The Rytov variance σ_R^2 for a plane wave can be defined as:

$$\sigma_R^2 = 1.23 C_n^2 k^{\frac{7}{6}} L^{\frac{11}{6}} \tag{2}$$

where *k* is the optical wave number, *L* is the propagation distance between the transmitter and receiver, and C_n^2 is the index of refraction structure parameter.

C_n^2 is a parameter commonly used to characterize the strength of atmospheric turbulence. The index of refraction structure parameter C_n^2 comes from the

generalized structure parameters used to describe turbulent fields [2]. The generalized structure parameter is defined as:

$$D_x(R_1, R_2) = \left\langle |x(R_1) - x(R_2)|^2 \right\rangle \quad (3)$$

where *x* is the measured quantity and R_1 and R_2 are 2 different positions at which *x* is measured at. The index of refraction structure parameter C_n^2 arises when the measured quantity is the index of refraction *n*, such that $D_n(R) = C_n^2 R^{2/3}$ within the inertial subrange defined by $l_0 \ll R \ll L_0$, where l_0 is the inner scale and L_0 is the outer scale [2]. Typical values of C_n^2 range from 10^{-17} $m^{-2/3}$ in very weak turbulence up to about 10^{-12} $m^{-2/3}$ in strong turbulence [2].

As the scintillation index σ_I^2 enters the strong fluctuations regime and surpasses 0.3, σ_I^2 eventually reaches a maximum value and enters a saturation regime. As shown in Figure 1.1, the scintillation index σ_I^2 is no longer proportional to the Rytov variance σ_R^2 in the saturation regime and other methods must be used to calculate C_n^2. The Rytov variance σ_R^2 can continue to be extended into the strong fluctuations regime by increasing the propagation distance *L* or by increasing C_n^2 [2][4].

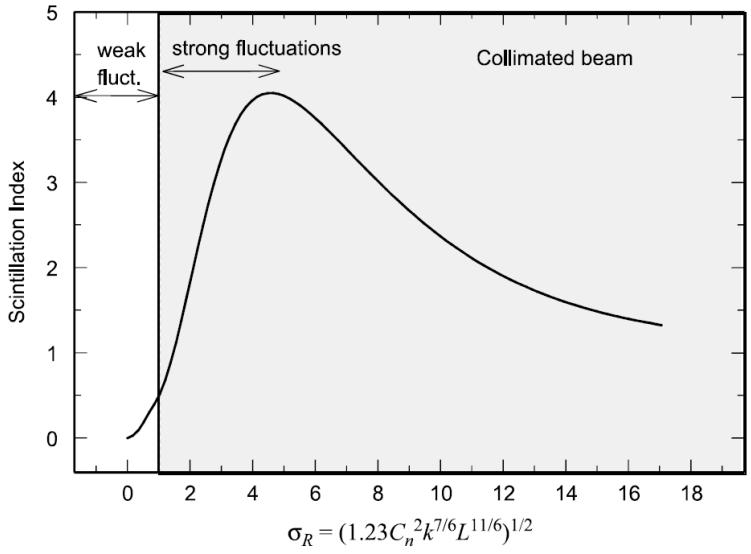

Figure 1.1: Scintillation index versus Rytov variance (experimental data) [2].

For scintillation measurements involving a large aperture receiver (in contrary to point source intensity fluctuations mentioned above), a C_n^2 value can be evaluated using the following equation:

$$C_n^2 = 1.12\sigma_{\ln(I)}^2 D^{7/3} L^{-3} \tag{4}$$

where D is the transmitter and receiver aperture size and L is the propagation length. Equation 2 and Equation 4 represent path averaged values of C_n^2 over the propagation length L. A point measurement of C_n^2 can be computed from C_T^2 measurements. C_T^2 can be calculated by the following equation [2]:

$$D_T(R) = \left\langle |T_1 - T_2|^2 \right\rangle = C_T^2 R^{2/3}, \qquad l_0 \ll R \ll L_0 \tag{5}$$

where l_0 is the inner scale, L_0 is the outer scale, R is the distance between temperature measurements T_1 and T_2, and C_T^2 is the temperature structure parameter. The index of refraction for the atmosphere at optical and IR wavelengths can be related to temperature and pressure fluctuations by the following equation [2]:

$$n(R) \cong 1 + (79 \times 10^{-6}) \frac{P(R)}{T(R)} \quad (6)$$

where P is the pressure in millibars and T is the temperature in kelvin. Finally, with Equation 5 and Equation 6, point measurements of C_n^2 can be directly computed from experimentally determined C_T^2 values by the relation [2]:

$$C_n^2 = \left[(79 \times 10^{-6}) \frac{P}{T^2}\right]^2 C_T^2 \quad (7)$$

where P is the pressure in millibars and T is the temperature in kelvin.

Experimental characterization

A scintillometer is the most common device used to evaluate C_n^2 [5][6]. The basic operation of a scintillometer involves a transmitter and receiver setup. The transmitter sends a known optical signal through a channel of length *L*. The aperture on the receiver collects the signal intensity and is able to compute the normalized intensity variance, and then correspondingly compute a path averaged C_n^2 value. In order to mitigate intensity variance saturation effects in the strong fluctuation regimes, large aperture scintillometers (LAS) utilize the aperture averaging effect. A larger aperture allows for an overall reduction in scintillation effects due to the aperture being larger than the spatial scale of the atmospheric scintillation [1][2]. The following condition can be used to determine if the transmitting and receiving apertures are large enough to avoid saturation for a given path length and turbulence strength [7]:

$$\frac{D_T + D_R}{2\sqrt{\lambda L}} > (\sigma_T^2)^{3/5} \quad (8)$$

where D_T is the diameter of the transmitting aperture, D_R is the diameter of the receiving aperture, L is the propagation length, and λ is the wavelength of the transmitters optical source. It is standard practice in LAS design for D_T and D_R to be the same. σ_T^2 is defined as [7]:

$$\sigma_T^2 = 0.124k^{7/6}L^{11/6}C_n^2 \quad (9)$$

where $k = \frac{2\pi}{\lambda}$, L is the propagation length, and C_n^2 is the index of refraction structure parameter. Unfortunately there often becomes a limit, whether due to cost or size restraints, as to how large the transmitting and receiving apertures can be in a scintillometer.

C_T^2 can also be used to indirectly calculate a corresponding point measurement of C_n^2. Multiple resistance temperature detectors (RTDs) can be used to take several precise temperature point measurements at known distances apart. It is important to ensure that the RTD measurements are precise and quick enough to calculate small C_n^2 values from very small temperature fluctuations. In addition, care must be taken to space the RTDs far enough apart as to satisfy the condition $l_0 \ll R \ll L_0$. By applying Equation 5 and Equation 6, these temperature measurements allow for a way to determine a point measurement of C_n^2.

1.2) Beam Wander

Beam wander causes a propagating beam to move about an average position. The averaged changes in the index of refraction along the propagation path cause this movement about an average position. Beam jitter refers to beam wander that occurs quickly, while beam drift refers to beam wander that occurs more slowly [1]. Beam

wander can be thought of as a global tilt in the wavefront because the centroid of the beam is constantly changing in position. This generally leads to misalignment effects as the beam is unable to stay pointed on the receiver. A simple solution to beam wander is increasing the size of the receiving aperture so that the probability of the beam remaining on the receiving aperture is also increased. Unfortunately, there are limitations as to how large a receiving aperture can be made, whether due to cost or size constraints. Another solution is the inclusion of a fast steering mirror into the adaptive optics system. Beam wander has a time constant proportionate to $\frac{beam\ diameter}{wind\ speed}$ [2]. A fast steering transmitter (often implemented with a fast steering mirror) is easily capable of working in the kilohertz range and provides adequate tip and tilt control of the beam [8]. A feedback loop can be initiated with the receiver to maximize the intensity received on the receiving aperture.

Beam wander can be analyzed through the concept of a long term beam radius W_{LT} and a short term beam radius W_{ST}. Figure 2 below is an illustration of W_{LT} and W_{ST} [2].

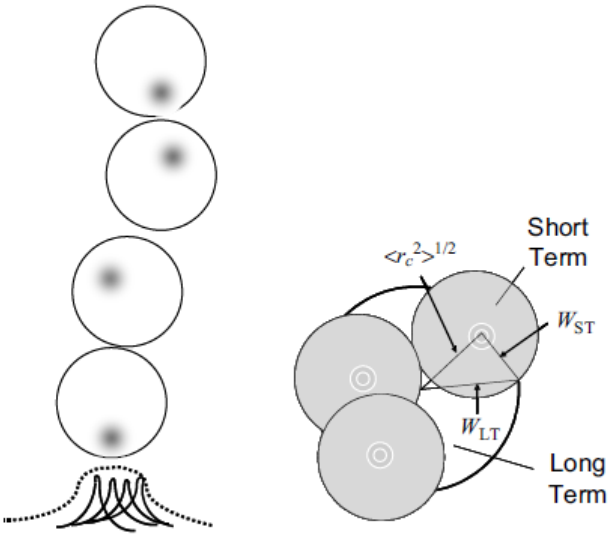

Figure 1.2: Long term vs short term beam radius [2].

W_{ST} represents the short term beam radius arising from small scale beam spreading, while W_{LT} is the summation of W_{ST}, diffraction, and $\langle r_c^2 \rangle^{1/2}$. For a collimated Gaussian beam and using the approximation of an infinite outer scale ($\kappa_0 = 0$), the variance of the center of the beam at the receiver plane $\langle r_c^2 \rangle$ can be described as [2]:

$$\langle r_c^2 \rangle = 2.42 C_n^2 L^3 w_0^{-1/3} \tag{10}$$

where C_n^2 is the index of refraction structure parameter, L represents the propagation distance, and w_0 is the beam radius. $\langle r_c^2 \rangle$ provides an estimate for the magnitude of beam wander depending on the turbulence strength and propagation distance.

1.3) Beam spreading/break up

The presence of atmospheric turbulence causes the beam to have wavefront variations due to the time and spatially varying fluctuations in the index of refraction. Similar to the index of refraction structure parameter C_n^2, a phase structure parameter D_ϕ can be determined for the phase difference δ_ϕ between two parallel paths in the atmosphere separated by a distance ρ [1]:

$$D_\phi = 1.46 k^2 C_n^2 L \rho^{5/3}, \qquad l_0 < \rho < L_0 \tag{11}$$

where $k = \frac{2\pi}{\lambda}$, L is the propagation length, C_n^2 is the index of refraction structure parameter, l_0 is the inner scale, and L_0 is the outer scale. The phase difference δ_ϕ can be defined as [1]:

$$\delta_\phi = k\rho[\Delta n(\rho)] \tag{12}$$

where $k = \frac{2\pi}{\lambda}$, ρ is the separation distance between two parallel paths, and $\Delta n(\rho)$ is the difference in refractive index. As C_n^2 or the propagation distance L increases, a beam may undergo significant wavefront distortions that results in the loss of coherence which invalidates many plane-wave approximations made in beam propagation [1][2]. Generally speaking, the phase difference in which a beam remains coherent is defined by the condition:

$$\langle(\delta_\phi)^2\rangle < \pi^2 \tag{13}$$

An important parameter that involves the coherence of a beam is the Fried coherence length r_0 [1][2]:

$$r_0 = \left[0.423k^2 \int_0^L C_n^2(z)dz\right]^{-3/5} \tag{14}$$

where L is the propagation length, $k = \frac{2\pi}{\lambda}$ is the wavenumber, and $C_n^2(z)$ is the refractive index structure parameter that may be variable with the position z [1]. The Friend coherence length r_0 is a parameter often used to describe atmospheric conditions because it includes the strength of turbulence C_n^2, the propagation length L, and the wavelength λ [1][2]. In addition, r_0 is also referred to as the "seeing parameter" where a large r_0 value represents "good seeing" and a small r_0 value represents "bad seeing". It can be shown that the resolving power of an optical system is limited by the optics when the aperture diameter D is smaller than r_0, and limited by the atmosphere when the aperture diameter D is larger than r_0 [2]. In other words, r_0 describes a limit of the largest effective aperture diameter in an optical system before atmosphere turbulence severely impacts performance.

Beam breakup can be observed as several large patches of light within the beam itself. Although the overall coherence of the beam is lost, the smaller individual patches of light can be treated as individually propagating beams [1][2]. One way to experimentally measure the presence of beam breakup is by observing the Fourier spectrum of the beam. If there are multiple portions of the wavefront that are significantly different in phase, a thin lens performing a Fourier transform will show multiple focal spots at the back focal plane. Each focal spot represents a different portion of the beam with significantly different phase that will "breakup" if allowed to propagate further. This serves to estimate the presence of beam breakup but does not provide an answer to the characterization and correction for this complicated phenomenon.

2) Plenoptic Wavefront Sensor

The idea of the Plenoptic Wavefront Sensor, or Plenoptic Sensor, originates from the light field camera [9][10][11]. The light field camera, or plenoptic camera, was originally designed for imaging purposes. The main function of the light field camera is to preserve information about image depth with just a single camera exposure. A traditional camera with a main lens and image sensor loses the incident light rays angular information because the irradiance from all the incident light rays is averaged over the image sensor with each exposure. Additionally, this means that objects in the image that are incorrectly focused become blurred due to their incident light rays being distributed over an improperly large sensor area [9][12].

The light field camera approaches this problem by trading some of the spatial resolution in the image plane for angular resolution in the aperture plane [13]. This is achieved by the placement of a micro-lens array at some distance behind the main lens and in front of the image sensor. The placement of the micro-lens array and the main lens can be used in multiple configurations, but a popular configuration (the standard plenoptic camera) involves placing the micro-lens array at the back focal plane of the main lens [13][14]. As a result of the added micro-lens array, each camera exposure produces several different images (equal to the micro-lens count) that are captured from different angles.

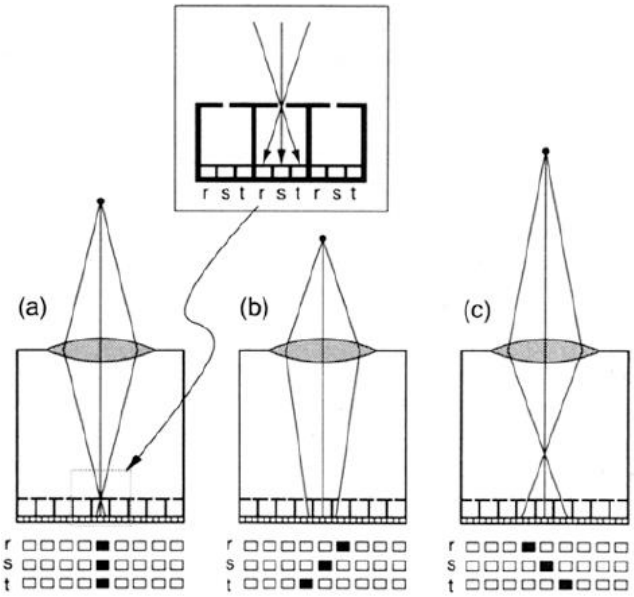

Figure 2.1: Extracting image depth from pinholes [9].

An example of how the standard plenoptic camera operates is shown in Figure 2.1. The standard plenoptic camera images an object in Figure 2.1a, Figure 2.1b, and Figure 2.1c which is in the plane of focus, nearer to the plane of focus, and further from the plane of focus, respectively. In this simplified example, a pinhole array (as opposed to a micro-lens array) is placed at the back focal plane of the imaging lens. This is contrary to a conventional camera where the image sensor is placed at the back focal plane of the image lens. In Figure 2.1a, the in-focus object is focused onto a single on-axis pinhole which illuminates all three pixels r, s, and t behind the on-axis pinhole. If an image sensor is used in place of the pinhole array (as in a conventional camera), the object would still produce a sharp focus on the image sensor. However, in Figure 2.1b and Figure 2.1c, it is evident that the out of focus object illuminates separate pinholes, and therefore different pixels, corresponding to whether the object is nearer or further from the plane of focus. The illuminated pixel

information can be used to determine the depth of the image in the scene because the angular information from the out of focus rays is preserved and separated into different pinholes [9]. If an image sensor is used in place of the pinhole array (as in a conventional camera), the out of focus objects create a blurred image due to averaging of all the out of focus rays, which illustrates the problem of a loss of angular ray information. The standard plenoptic camera design has also been used in astronomy for wavefront sensing [15][16]. In a similar manner to the above scenario, each micro-lens array image represents an image of the sun or star (or other celestial body) from a different angle. This allows for an estimation of the wavefront by measuring the differences between each individual micro-lens image and translating the angular information into wavefront phase information. These past developments in plenoptic sensing are the inspiration behind the development of the Plenoptic Sensor utilized in our experiments.

2.1) Basic structure and design

The Plenoptic Sensor uses a modified configuration of the main lens and micro-lens array in order to perform wavefront sensing in strong turbulence conditions. With complex wavefront sensing in mind, the Plenoptic Sensor should be resistant to strong turbulence situations that often lead to scintillation, beam wander and beam breakup. The light field approach sacrifices spatial resolution of the wavefront in order to better preserve the complex phase information that is vital to performing accurate wavefront sensing.

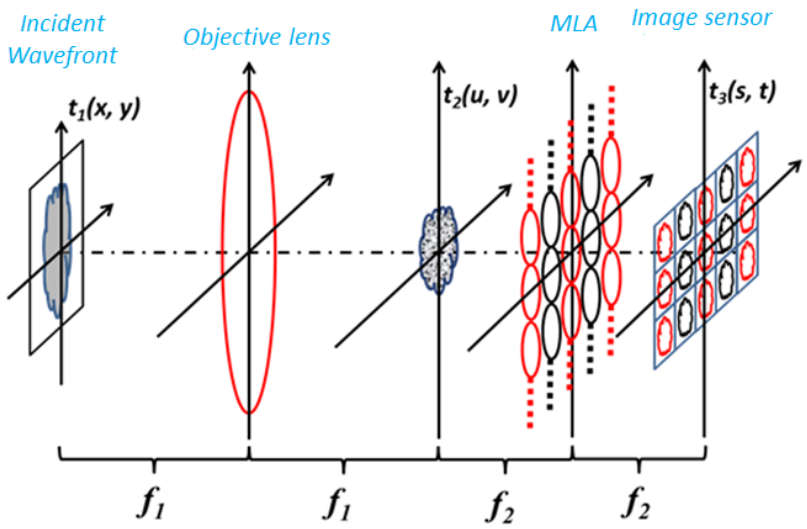

Figure 2.2: Diagram of the Plenoptic Sensor.

The basic configuration of the Plenoptic Sensor is shown in Figure 2.2. Consistent with the previous discussion about light field cameras, the Plenoptic Sensor consists of an objective lens, micro-lens array (MLA), and image sensor. The back focal plane of the objective lens and front focal plane of the MLA is such that they coincide on the same plane. The image sensor is located at the back focal plane of the MLA. This optical configuration can be viewed as an array of mini-Keplerian telescopes that share a common objective lens [17][18].

The plane of the wavefront reconstruction lies at the front focal plane of the objective lens. From Fourier optics, the objective lens performs a 2D Fourier transform of the incident wavefront $t_1(x,y)$ at the front focal plane to the transformed wavefront $t_2(u,v)$ at the back focal plane [19]. This transformation can be described by the following equation:

$$t_2(u,v) = \frac{1}{j\lambda f_1} \iint_{-\infty}^{\infty} \mathrm{t}_1(x,y)\exp\left\{\frac{-j2\pi}{\lambda f_1}(ux+vy)\right\}dxdy \qquad (15)$$

The MLA then spatially subsamples $t_2(u,v)$ and performs the inverse Fourier transform to the back focal plane [18].

$$t_3^{M,N}(s,t) = \frac{1}{j\lambda f_2} \iint \mathrm{t}_2(u'+Md, v'+Md)\mathrm{rect}\left(\frac{u'+s'}{d}\right)\mathrm{rect}\left(\frac{v'+t'}{d}\right)\exp\left\{\frac{-j2\pi}{\lambda f_2}(u's' + v't')\right\} du'dv' \qquad (16)$$

$$(s',t') = (s-Md, t-Nd)$$

$$(u',v') = (u-Md, v-Nd)$$

The coordinates (M,N) represent the indices for each MLA lenslet and d represents the pitch of each MLA. A rectangular pupil function is introduced to limit the Fourier transform to the specific MLA lenslet. In addition, (u',v') and (s',t') represent the local coordinates within an MLA lenslet in relation to the global coordinates (u,v) and (s,t). The overall field on the image sensor $t_3(s,t)$ is the summation $t_3^{M,N}(s,t)$ across all the MLA lenslets.

$$t_3(s,t) = \sum_{M,N} t_3^{M,N}(s',t') \qquad (17)$$

Substituting in $t_3^{M,N}(s,t)$ from Equation (16) into the summation above produces the final result:

$$t_3(s,t) = \frac{1}{j\lambda f_2} \iint \mathrm{t}_2(u,v)\sum_{M,N}\mathrm{rect}\left(\frac{u+s-2Md}{d}\right)\mathrm{rect}\left(\frac{v+t-2Md}{d}\right)\exp\left\{\frac{-j2\pi}{\lambda f_2}((u-Md)(s-Md)+(v-Nd)(t-Nd))\right\}dudv \qquad (18)$$

Equation (18) shows the final field $t_3(s,t)$ on the image sensor plane after the secondary Fourier transform performed by the MLA. In order to ensure that a

collimated beam filling the entire objective lens can be imaged by a single MLA lenslet, we impose the following numerical aperture requirements [17][18]:

$$\frac{d_{obj}}{f_{obj}} \leq \frac{d_{MLA}}{f_{MLA}} \tag{19}$$

where d_{obj} and f_{obj} represent the objective lens diameter and objective lens focal length, respectively, and d_{MLA} and f_{MLA} represent the MLA lenslet diameter and MLA lenslet focal length, respectively. In general, the numerical apertures of the objective lens and the MLA lenslets are matched in order to maximize the use of image sensor pixels behind each lenslet without accidentally overlapping any images.

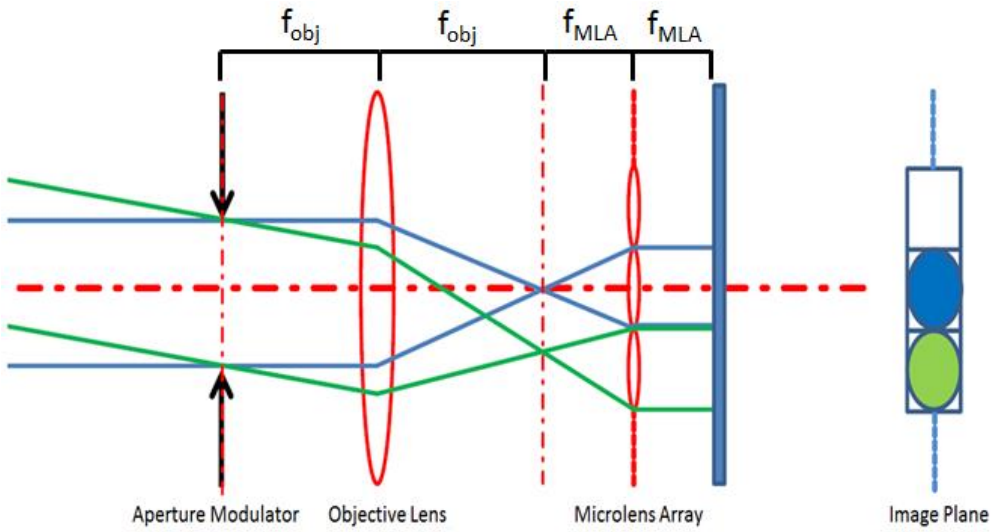

Figure 2.3: Ray tracing diagram of Plenoptic Sensor.

Figure 2.3 illustrates from a geometrical optics perspective how the Plenoptic Sensor interprets phase gradient differences in the wavefront. The blue rays and the green rays represent 2 collimated wavefronts that are distinguished by a global wavefront tilt. The blue rays are traveling parallel to the propagation axis while the

green rays are tilted with respect to the propagation axis. It becomes obvious that incoming rays that are parallel to the propagation axis will always be imaged by the center MLA sub-aperture. Any rays that have a tilt with respect to the propagation axis, such as the green rays, will be imaged by off-axis MLA sub-apertures. To generalize, the MLA spatially subsamples the Fourier spectra of the incoming wavefront. The result is a plenoptic image at the back focal plane of the MLA where each pixel on the image sensor directly corresponds to a specific location and angular spectrum of the incoming wavefront. From Figure 2.3, it is also apparent that this configuration is similar to a Shack-Hartmann wavefront sensor but with the addition of an objective lens. A further comparison between the Plenoptic Sensor and Shack-Hartmann sensor is performed in Section 2.3.

2.2) Wavefront Reconstruction

Wavefront reconstruction using a Plenoptic Sensor is performed by analyzing the Plenoptic image for the phase and amplitude information. As mentioned in the previous section, the MLA sub-apertures are indicative of a certain angular spectrum (and correspondingly the phase gradient information) of the wavefront while the intensity in these sub-apertures represents the amplitude information. We can generalize the wavefront reconstruction algorithms into 2 categories. The first category involves a wavefront reconstruction algorithm focused on reconstructing the wavefront with the lowest error possible with the assumption that reconstruction time is not an issue. This accuracy-based wavefront reconstruction algorithm is ideal for dealing with static or slowly time varying aberrations in an optical system, such as when dealing with aberrations in an indoor experimental setup. The second category

involves a wavefront reconstruction algorithm focused on reconstructing the wavefront as quick as possible while allowing for slight wavefront reconstruction errors along the way. This speed-based algorithm is ideal for situations involving rapidly time varying and large amplitude wavefront distortions such as in strong atmospheric turbulence. Two separate algorithms are discussed in this section to address these different needs.

2.2.1) Checkerboard Reconstruction Algorithm

The checkerboard reconstruction algorithm is aimed at reconstructing the wavefront with as little error as possible. The meaning behind the "checkerboard" name is to represent the further subdivision of each sub-aperture into smaller quantized "checkerboard" units. Each sub-aperture already represents a subdivision of the total image sensor into areas representing a specific angular spectrum of the wavefront [20]. The further subdivision of each sub-aperture into these "checkboard" units represents different spatial locations of the incoming wavefront. Figure 2.4 clarifies this point.

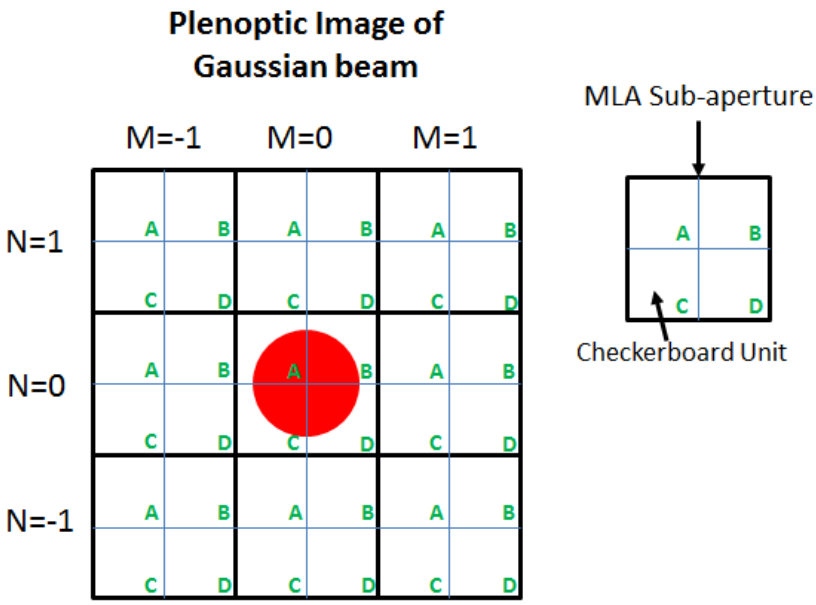

Figure 2.4: Plenoptic image of undistorted beam with checkerboard units overlaid.

Figure 2.4 shows a plenoptic image with a black grid outlining different MLA sub-apertures. In addition, each sub-aperture is further divided by a blue grid into four different checkerboard units. Each checkerboard unit is labeled with “A”, “B”, “C”, or “D”. It is easy to see that every MLA sub-aperture contains these four checkerboard units. The reasoning is because each checkerboard unit “A” represents the same spatial location of the incoming wavefront despite each sub-aperture representing a different angular spectrum. The same situation applies for “B”, “C”, “D”, or however else the sub-aperture may be subdivided into. For the simplicity of this example, we divide each sub-aperture into only 4 checkerboard units “A” through “D”. Figure 2.4 also shows an undistorted Gaussian beam in the center MLA sub-aperture, as shown by the red circular beam in MLA sub-aperture (M=0, N=0). This is because the center MLA sub-aperture (M=0, N=0) is aligned with the optical axis

and will only image the planar/undistorted portion of an incoming wavefront. Therefore, an undistorted beam will be entirely imaged by sub-aperture (M=0, N=0). This will change as the wavefront becomes distorted.

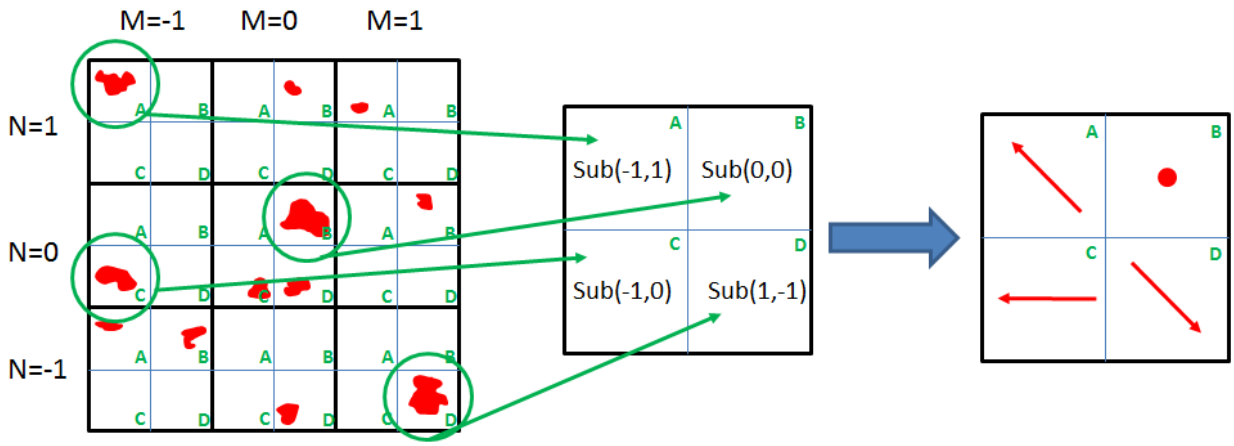

Figure 2.5: Wavefront gradient information from checkerboard units.

The left image in Figure 2.5 now shows a Plenoptic Image of a distorted beam. As a result of the wavefront distortion, the beam is no longer solely present in the center MLA sub-aperture (M=0, N=0), which we will denote as Sub(0,0). Instead, the intensity is now distributed into the different sub-apertures that represent the angular spectrum of each intensity patch. In order to perform the checkerboard reconstruction, we first examine checkerboard unit "A". Checkerboard unit "A" has a non-zero intensity sum value only in sub-apertures Sub(-1,1), Sub(-1,-1), and Sub(1,1). However, it is clear that Sub(-1,1) has the largest intensity sum value out of those 3 non-zero intensity sum value sub-apertures. Therefore, Sub(-1,1) is selected as the sub-aperture (as well as its corresponding angular spectrum) representing the spatial location of the wavefront denoted as Checkerboard Unit "A". This sub-aperture selection is recorded in the middle image in Figure 2.5 for Checkerboard

Unit “A”. Next, we move onto Checkerboard unit “B”, and notice that the largest intensity sum value resides in Sub(0,0). This sub-aperture index is then recorded once again in the middle image in Figure 2.5. This process continues for the remaining checkerboard units. Finally, because each sub-aperture corresponds to a specific angular spectrum of the wavefront, the recorded sub-aperture index in each checkerboard unit directly corresponds to the local wavefront gradient *through* $(M\Delta\varphi, N\Delta\varphi)$, where M and N are the sub-aperture indices and $\Delta\varphi$ represents the phase difference between two adjacent sub-apertures. The exact value of $\Delta\varphi$ depends on the hardware parameters and an example is calculated in Section 2.3 for specific hardware configurations. In the right image of Figure 2.5, we assign a local gradient pointing up and to the left for Checkerboard unit “A” because Sub(-1,1) is located up and to the left of the on-axis centralized Sub(0,0). The exact local gradient is denoted by $((-1)\Delta\varphi, (+1)\Delta\varphi)$. Next, we assign a local gradient of zero in Checkerboard unit “B” because Sub(0,0) is the on-axis sub-aperture representing zero wavefront tilt. The exact local gradient is denoted by $((0)\Delta\varphi, (0)\Delta\varphi)$. This continues for the remaining checkerboard units and a map of local gradients is finally compiled closely resembling a Hartmann-gram produced by a Shack-Hartmann sensor [21][22]. It is important to note that the specified size of the checkerboard units can be as small as an image pixel, representing the finest spatial resolution possible, or enlarged to include a group of pixels in order to speed up calculations at the expense of wavefront reconstruction accuracy.

After the local gradient measurements have been made, various wavefront reconstruction techniques can be used to reconstruct the full wavefront [1][21]. For

example, a Least Mean Square Error reconstructor is a popular method of using local wavefront gradient measurements to reconstruct the full wavefront [21][23]. There are also applicable image reconstruction techniques that use gradient field information to reconstruct the surface of an object [24]. The reconstruction of a 3D surface from gradient fields is a well-researched area that is also applied to the Shack-Hartmann wavefront sensor, and similar methods of wavefront reconstruction can be shared with the Plenoptic Sensor [21][24].

2.2.2) Graph Reconstruction Algorithm

The Graph Reconstruction Algorithm is aimed at reconstructing the wavefront as quickly as possible while acknowledging that there may be slight wavefront reconstruction errors. The speed of wavefront reconstruction is extremely important when compensating for atmospheric turbulence which changes on the timescale of milliseconds [1][3]. In order to remove unwanted wavefront distortions from an optical system, the wavefront must be reconstructed and the phase conjugate applied to a deformable mirror before the distortions caused by atmospheric turbulence change. Examples of performing wavefront correction with a deformable mirror are presented in the experimental results in Section 3.1. The Graph Reconstruction Algorithm uses knowledge of the deformable mirror actuator layout and inter-actuator pitch in order to quickly perform wavefront reconstruction.

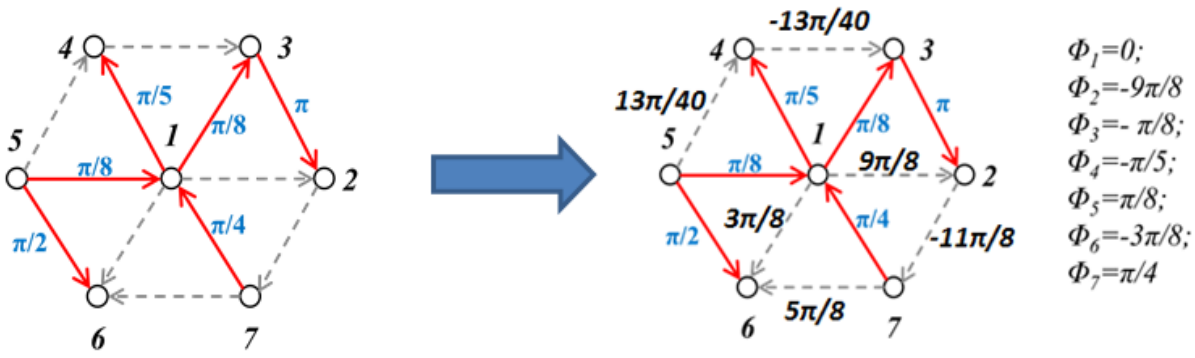

Figure 2.6: Minimum degree spanning tree of deformable mirror actuators.

The left image in Figure 2.6 shows a tree graph of 7 nodes. These 7 nodes represent 7 deformable mirror actuators, although the deformable mirror may have many more actuators in reality. The nodes are arranged in a hexagonal pattern identical to our OKO Deformable Mirror used in the experimental results presented in later sections [17][20][25]. To solve a graph with *n* nodes, *n-1* edges must be known in order to complete the minimum degree spanning tree. The red arrows in the Figure 2.6 represent known 6 known edges with corresponding weight values. The weight values represent the phase differences between the nodes. With this information, a system of equations can be solved to compute the weight values (i.e. phase differences) along the remaining grey arrows. The right image in Figure 2.6 shows the result of solving a simple matrix equation for the unknown weight values. The remaining grey arrows now have their phase differences labeled. This gives a coarse wavefront reconstruction that accounts for the geometry of the deformable mirror actuators. This algorithm can be completed much more quickly than recreating the full surface from a dataset of gradient fields, which is the method traditionally found

in Shack-Hartmann sensors and our previously mentioned Checkerboard reconstruction algorithm [21][23][24].

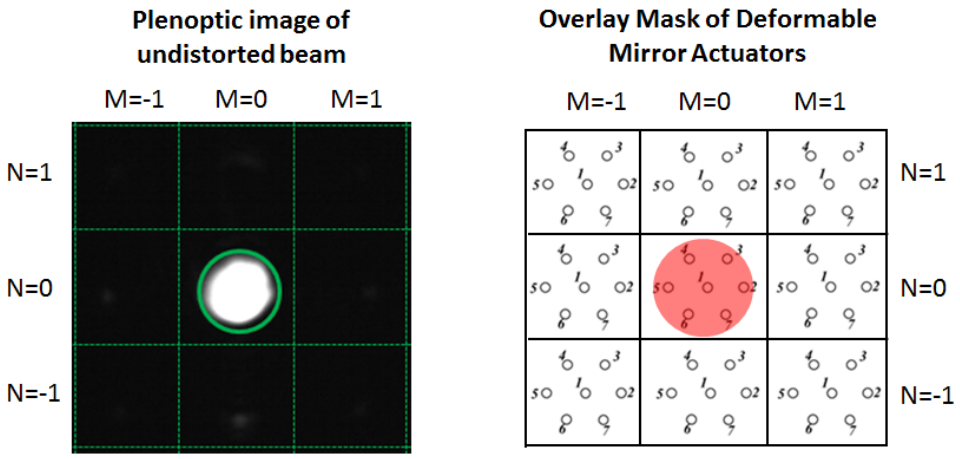

Figure 2.7: Actuator tree overlaid onto plenoptic image of undistorted beam.

Figure 2.7 shows only 9 MLA sub-apertures to simplify this example. Similar to Figure 2.4, the grid shows the borders of the MLA sub-apertures, and the undistorted beam is imaged solely by the center MLA sub-aperture. The tree from Figure 2.6 is applied onto each sub-aperture in a similar manner to the checkerboard units in the checkerboard reconstruction algorithm. The same sub-aperture naming convention Sub(M, N) is used as in the checkerboard reconstruction algorithm in Section 2.2.1.

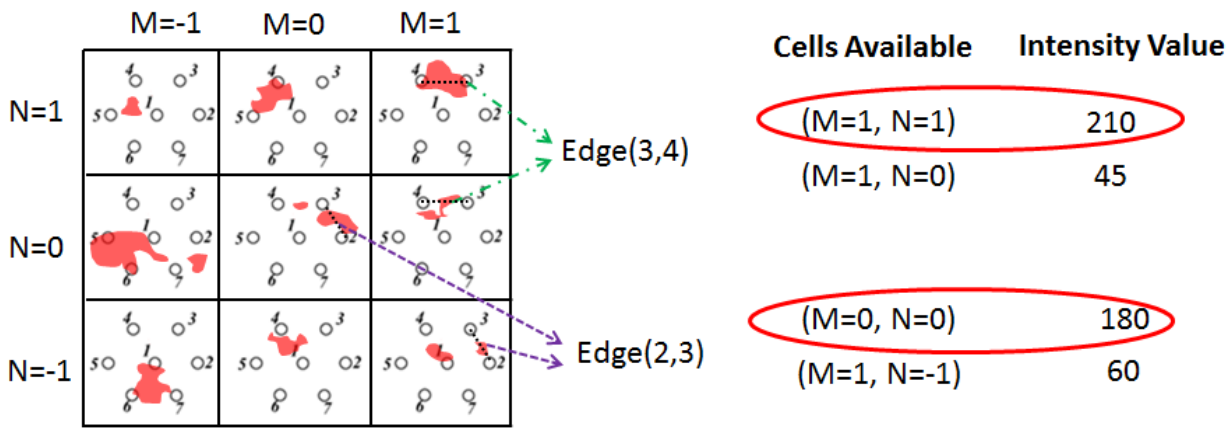

Figure 2.8: Plenoptic image of a distorted beam with actuator tree overlaid.

Each edge in the tree must be assigned a corresponding sub-aperture to represent its phase difference. For example, in Figure 2.8, we first examine Edge(3,4). Edge(3,4) only has a non-zero intensity sum value in MLA sub-apertures Sub(1,1) and Sub(1,0) . However, along Edge(3,4), Sub(1,1) has a larger intensity sum value of "210" compared to Sub(1,0) which has an intensity sum value of "45". For this case, Edge(3,4) and Sub(1,1) are assigned as a pair. When examining Edge(2,3) in Figure 2.7, it is clear that Sub(0,0) provides the largest intensity sum value of "180". Therefore, Edge(2,3) and Sub(0,0) are assigned as a pair. This continues until there is an Edge(M,N) and Sub(M,N) pair for every Edge(M,N) in the tree graph.

For the 7 actuator example, there are a total of 12 edges between the 7 neighboring actuators nodes. For the tree with *n* nodes, only *n-1* edges are required to be selected to form a minimum degree spanning tree. Therefore, the most "informative" edges are selected according to the following criteria:

1. Begin with a set of 7 unused actuator nodes U = {1,2,3,4,5,6,7}, a set of 12 edges EdgeList = { Edge(a,b), … , Edge(w,x) }, and an empty set Final = {}.
2. Sort EdgeList in descending order by each Edge(M,N)'s intensity sum value.
3. Select the highest ranked edge Edge(a,b).
4. If "a" or "b" are present in set U, then Edge(a,b) is selected for the minimum degree spanning tree. Remove Edge(a,b) from the set EdgeList and add Edge(a,b) to the set Final{}. Remove "a" and b" from set U.
5. Else, since "a" and "b" are both not present in U, then they have already been utilized in the minimum degree spanning tree. Remove Edge(a,b) from the list of sorted edges.
6. Return to step 2) and repeat until set U{} is empty.

After the above process is complete, set Final{} contains a list of *n-1* edges that form a minimum degree spanning tree with the most "informative" edges determined by their associated intensity sum value.

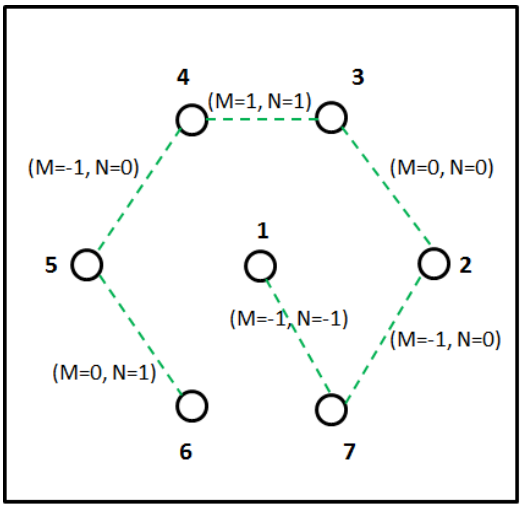

	M=-1	M=0	M=1
N=1	$(-\phi_x, +\phi_y)$	$(0, \phi_y)$	$(+\phi_x, +\phi_y)$
N=0	$(-\phi_x, 0)$	0,0	$(+\phi_x, 0)$
N=-1	$(\phi_x, -\phi_y)$	$(0, -\phi_y)$	$(+\phi_x, -\phi_y)$

Figure 2.9: Selected edges between nodes and associated phase map.

The left side of Figure 2.9 shows the completed minimum degree spanning tree with the selected Edge(a,b) and Sub(M,N) pair. From here, it is simple to determine the phase difference between each actuator by using the assigned Sub(M,N). The right side of Figure 2.9 is a precompiled table of the phase difference values assigned to each sub-aperture Sub(M,N). The phase differences (ϕ_x, ϕ_y) are computed by:

$$(\phi_x, \phi_y) = \frac{d_{MLA}}{f_{obj}}(\mathrm{M}, \mathrm{N}) \tag{20}$$

where d_{MLA} is the pitch of the MLA, f_{obj} is the focal length of the objective lens, and (M, N) is the sub-aperture indices. With the minimum degree spanning tree complete and with knowledge of the associated phase difference values along each edge, there are enough known values to solve for all the phase differences between the n nodes. A system of equations can quickly be solved to map the phase differences between every deformable mirror actuator.

This is a wavefront reconstruction algorithm that recognizes the limitation of having a finite number of actuators and sacrifices some wavefront reconstruction accuracy. However, the major advantage is that this algorithm does not perform a full 2D surface reconstruction and instead performs a simple algebraic calculation that lowers the wavefront reconstruction time. In addition, a side benefit of this "path averaged" reconstruction is that the discarded low intensity edges do not affect the reconstruction result. Areas of low intensity may occur in the locations of branch points and branch cuts. By discarding these low intensity edges, the graph wavefront reconstruction "detours" around these complicated areas of large phase discontinuities which may otherwise result in large reconstruction errors if the

reconstruction algorithm is not capable of handling the complexity of the phase changes [23].

2.3) Comparison with Shack-Hartmann Sensor

The Shack-Hartmann wavefront sensor has been an invaluable tool for decades in wavefront sensing and adaptive optics. Astronomers frequently use the Shack-Hartmann sensor to correct for atmospheric turbulence present while observing celestial bodies from the Earth's surface. The Shack-Hartmann sensor has been an area of great research and development in the field of astronomy for many decades and its success has steadily pushed the advancement of ground based telescopes [26][27][28]. The Shack-Hartmann wavefront sensor is also commonly used in optometry to determine the wavefront error caused by a misshaped retina [29][30][31]. In addition, the simplicity of the Shack-Hartmann sensor permits for a low cost wavefront sensor that can be lab-built or readily available for purchase from vendors such as ThorLabs.

The Shack-Hartmann sensor consists of an MLA with an image sensor located at the back focal plane. The Shack-Hartmann sensor measures the intensity weighted gradient of a wavefront over the spatial location of an individual MLA sub-aperture. This intensity weighted gradient is often referred to as the centroid tilt or C-tilt. When turbulence conditions are weak, the centroid tilt will match the intensity weighted average gradient over the sub-aperture, often referred to as the gradient tilt or G-tilt. Unfortunately, when turbulence conditions are strong, C-tilt/G-tilt anisoplanatism becomes present and accurate wavefront information cannot be extracted [32]. Self-

interfering portions of the wavefront and intensity scintillation prove to be a large challenge for the Shack-Hartmann sensor as well as for other wavefront sensors.

A comparison between the Shack-Hartmann sensor and the Plenoptic Sensor is a comparison that will inevitably arise. The Plenoptic Sensor is aimed at being able to make atmospheric wavefront measurements in which the Shack-Hartmann sensor has already demonstrated its effectiveness. The similarity in hardware design also poses the question about what advantages and disadvantages the Plenoptic Sensor has in comparison to the Shack-Hartmann sensor. It is important for the Plenoptic Sensor to address the issues the Shack-Hartmann sensor faces when operating in strong turbulence conditions. In addition, any tradeoffs in wavefront sensing performance should be analyzed to distinguish the two wavefront sensors.

2.3.1) Hardware comparison

2.3.1.1) Shack-Hartmann Sensor

The Shack-Hartmann sensor consists of an MLA of focal length f_{MLA} and an image sensor. The image sensor is placed a distance f_{MLA} behind the MLA. The wavefront being sensed is incident on the MLA which results in a focal spot being formed on the image sensor for each individual MLA sub-aperture. The centroid location of each focal spot is representative of the intensity weighted local tilt (i.e. phase gradient) of the wavefront at the corresponding sub-aperture location [1][22]. The full wavefront can be reconstructed by piecing together all the local wavefront tilt measurements. Many different techniques, such as the least mean square error (LMSE) reconstructor, have been developed to reconstruct the full wavefront from

local wavefront measurements [1][21][23]. More robust wavefront reconstructors can successfully recreate the wavefront despite the presence of branch points and branch cuts induced by strong atmospheric turbulence [23][33][34][35].

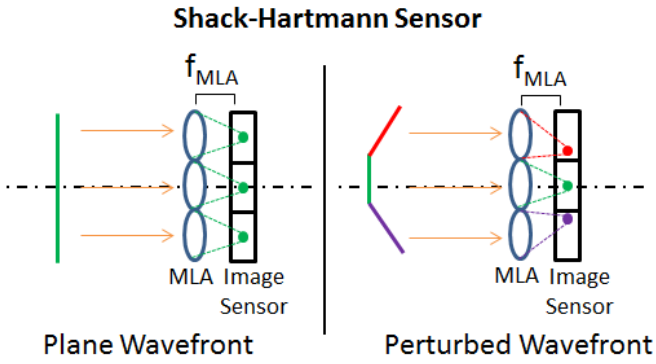

Fig. 2.10 Shack-Hartmann sensor operation.

The left side of Figure 2.10 shows a plane wavefront entering the Shack-Hartmann sensor. The focal spot on the image sensor behind each MLA sub-aperture coincides with the optical axis of the corresponding MLA sub-aperture. There is no centroid tilt away from the optical axis of each sub-aperture and therefore the portion of the wavefront entering each sub-aperture has no local tilt and is undistorted. On the right side of Figure 2.10 a perturbed wavefront enters the Shack-Hartmann sensor. The center portion of the wavefront (colored in green) remains undistorted while the top and bottom portions (colored in red and purple, respectively) are tilted in opposite directions. On the image sensor, the center sub-aperture still produces a focal spot coinciding with the optical axis of the sub-aperture. However, the top and bottom centroids corresponding to the top and bottom of the wavefront are shifted from the optical axis of each sub-aperture. By measuring the shift of the centroid and knowing

the MLA and image sensor specifications, the local wavefront tilt at each sub-aperture can be calculated. The local wavefront tilts *(Δx, Δy)* are calculated as:

$$(\Delta x, \Delta y) = \left(\frac{x_2}{f_{MLA}}, \frac{y_2}{f_{MLA}}\right) \quad (21)$$

In Equation (21), (x_2, y_2) are the coordinates referring to the geometric location within an MLA sub-aperture, where $(x_2=0, y_2=0)$ indicates the location of the optical axis within the MLA sub-aperture. A data set of local tilts *(Δx, Δy)* at each sub-aperture location can be compiled to produce a Hartmannogram. A complete Hartmannogram can then be used to perform a complete wavefront reconstruction using various wavefront reconstruction techniques that utilize local gradient information [1][21][22].

2.3.1.2) Plenoptic Sensor

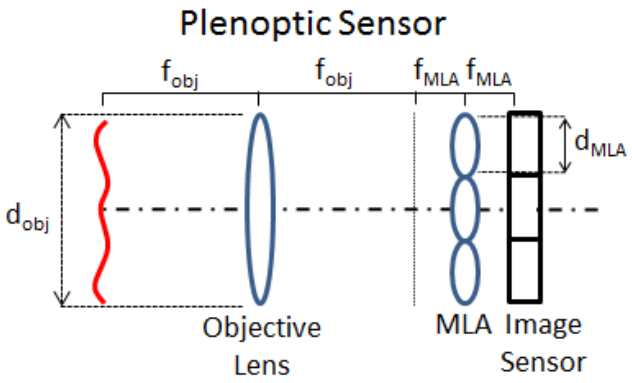

Figure 2.11: Plenoptic Sensor diagram.

The back portion of the Plenoptic Sensor consists of an identical MLA and image sensor configuration as is present in the Shack-Hartmann sensor. The image sensor is located a distance f_{MLA} behind the MLA. As shown in Figure 2.11, the notable difference is the addition of an objective lens with focal length f_{obj} that is

placed a distance $f_{obj}+f_{MLA}$ in front of the MLA. This shifts the plane of the reconstructed wavefront to a distance f_{obj} in front of the objective lens [17][18][19]. This is in contrast to the Shack-Hartmann sensor where the plane of the reconstructed wavefront is located at the plane of the MLA. The relationship between a geometric location within a sub-aperture (x_2, y_2) to the corresponding location at the front focal plane of the objective lens (x_1, y_1) is characterized as:

$$(x_2, y_2) = \left(\frac{-f_{MLA}}{f_{obj}}\right)(x_1, y_1) \tag{22}$$

In Equation (22), (x_1, y_1) are the coordinates referring to the geometric location with respect to the primary optical axis centered on the objective lens. Likewise to the notation used in Equation (21), (x_2, y_2) are coordinates referring to the geometric location within an individual sub-aperture. The quantized angular spectrum imaged by an individual MLA sub-aperture is characterized as:

$$(\alpha, \beta) = \frac{d_{MLA}}{f_{obj}}(m, n) \tag{23}$$

In Equation (23), (α, β) is the angular spectrum imaged by the center of the MLA sub-aperture indexed by (m, n), where $(m=0, n=0)$ refers to the MLA sub-aperture centered upon the primary optical axis of the Plenoptic Sensor. The angular spectrum, or wavefront tilt, can be directly translated to the phase gradient at the front focal plane of the objective lens by the relation $(2\pi\alpha/\lambda, 2\pi\beta/\lambda)$, where λ represents the wavelength. Finer adjustments in the angular spectrum can be made for the off-axis (in relation to the center of the individual MLA sub-aperture) illuminated pixels by the following:

$$(\delta\alpha, \delta\beta) = -\left(\frac{x_2}{f_1}, \frac{y_2}{f_1}\right) \tag{24}$$

Therefore, the angular spectrum represented by an MLA sub-aperture can be adjusted by $(\alpha + \delta\alpha, \beta + \delta\beta)$ for off-axis illuminated pixels. For this comparison between the Plenoptic Sensor and the Shack-Hartmann sensor, we ignore the fine adjustment term in Equation (24) and use the results presented in Equation (23). However, for precise wavefront reconstruction purposes, Equation (23) and the adjustment term from Equation (24) are used to determine the exact angular spectrum of the wavefront. For this example, we use Equation (22) and Equation (23) to provide the relation between an illuminated pixel on the image sensor (x_2, y_2) and an illuminated portion of the wavefront (x_1, y_1) at the front focal plane of the objective lens with phase gradient (α, β) [17][36]. With this information, an equivalent Hartmannogram (identical to the dataset provided by a Shack-Hartmann sensor) can be constructed with the local phase gradient data across the measured wavefront. With the local phase gradient data, the complete wavefront reconstruction can be performed using techniques identical to those used in a Shack-Hartmann sensor, such as a least-mean square error reconstructor, or other reconstruction methods tailored towards the Plenoptic Sensor such as those mentioned in Section 2.2 [17][20][25][36].

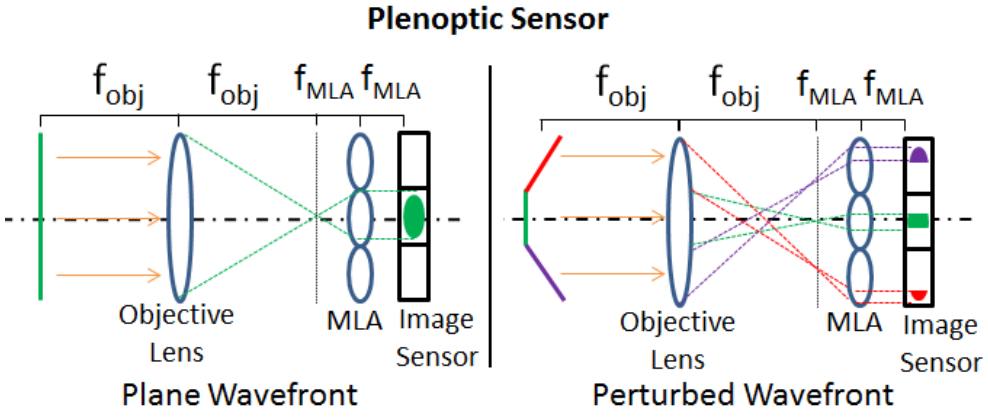

Figure 2.12 Plenoptic Sensor operation [48].

Figure 2.12 presents two wavefronts identical to those used in Figure 2.10 in the Shack-Hartmann sensor example. On the left side of Figure 2.12, a plane wavefront arrives at the objective lens and is focused to a spot at the back focal plane. The focal spot is then imaged solely by the center sub-aperture *(m=0, n=0)* and the Plenoptic image is entirely contained to the image sensor location directly corresponding to sub-aperture *(m=0, n=0)*.

The right side of Figure 2.12 has a perturbed wavefront incident on the objective lens. The center portion of the wavefront remains undistorted but the upper and lower portions are tilted downwards and upwards, respectively. As a result, only the central undistorted portion of the wavefront (denoted in green) is focused on the optical axis at the back focal plane of the objective lens. Therefore, only the central portion of the wavefront is imaged by the center sub-aperture *(m=0, n=0)*. In contrast, the top and bottom portions of the wavefront (denoted by the red and purple lines, respectively) are separated into different sub-apertures corresponding to their angular spectrum. By using the illuminated areas on the image sensor in conjunction with Equation (22) and Equation (23), the local wavefront phase and intensity information can be determined at front focal plane of the objective lens and the full wavefront can be reconstructed.

2.3.2) Gradient Information Comparison: Tilt sensitivity, tilt dynamic range, gradient sample size

The wavefront sensor in use must be properly designed to match the operating conditions. In this section we determine the wavefront tilt sensitivity, the dynamic

range, and the gradient sample size of the Shack-Hartmann sensor and the Plenoptic Sensor. In addition, two different scenarios are provided to compare the basic performance characteristics of each sensor. First we show how the basic performance characteristics can be determined for the Shack-Hartmann sensor:

$$(\Delta x_{min}, \Delta y_{min})_{SH} = \frac{Pixel\_Size}{f_{MLA}} \tag{25}$$

$$(\Delta x_{max}, \Delta y_{max})_{SH} = (\Delta x_{min}, \Delta y_{min})_{SH} \times \frac{d_{MLA}}{2 \times Pixel\_Size} \tag{26}$$

$$\left(N_{gradient}\right)_{SH} = \left(\frac{Sensor\_Width}{d_{MLA}}\right)^2 \tag{27}$$

Equations (25)-(27) are the calculations for three Shack-Hartmann sensor performance characteristics. Equation (25) represents the Shack-Hartmann sensor's minimum measurable wavefront tilt, or sensitivity, where *Pixel_Size* represents the width of the square pixel on the image sensor. Equation (26) represents the Shack-Hartmann sensor's maximum measurable wavefront tilt, or dynamic range. This is calculated by multiplying the Shack-Hartmann sensor's sensitivity (from Equation (25)) by the radius of each sub-aperture in terms of the image sensor pixel count. Equation (27) represents the Shack-Hartmann sensor's wavefront gradient sample count. This is determined by calculating the total number of square sub-apertures of pitch d_{MLA} that can fit on a square image sensor defined by a width of Sensor_Width. Next we show how these performance characteristics can be determined for the Plenoptic Sensor:

$$(\Delta x_{min}, \Delta y_{min})_{Plen} = \frac{d_{MLA}}{f_{obj}} \tag{28}$$

$$(\Delta x_{max}, \Delta y_{max})_{Plen} = \frac{Sensor\_width}{2 \times f_{obj}} \tag{29}$$

$$\left(N_{gradient}\right)_{Plen} = \left(\frac{d_{MLA}}{Pixel\_Size}\right)^2 \quad (30)$$

Equations (28) represents the Plenoptic Sensor's sensitivity. The sensitivity is calculated by applying Equation (23) for the case of (m=1, n=0) or (m=0, n=1). This designates the wavefront tilt between two patches of light arriving in directly adjacent sub-apertures and is the minimum wavefront tilt measurable by the Plenoptic Sensor (ignoring the fine adjustment factor calculated by Equation (24)). Equation (29) represents the Plenoptic Sensor's maximum measurable tilt, or dynamic range. This is calculated by first assuming the beam is initially aligned with the center of the MLA. Then, *Sensor_Width / (2 *d_{MLA})* represents the radius of the image sensor in terms of sub-aperture count. Finally, multiplying the sensitivity (Equation (28)) by the maximum number of sub-apertures in any direction (i.e. a radius of *Sensor_Width / (2 *d_{MLA})*) gives the dynamic range shown in Equation (29). Equation (30) represents the Plenoptic Sensor's minimum gradient sample count and is calculated by determining the maximum number of pixels that fit under the area denoted by a single sub-aperture. The reason a minimum number is quoted is because the gradient sample count is dynamic depending on the level of wavefront distortion [36]. Therefore, in this example we state the minimum gradient sample count that occurs when the wavefront has no distortions and is completely imaged by a single sub-aperture.

To compare the basic performance characteristics of the Shack-Hartmann sensor and the Plenoptic Sensor we analyze two different hardware scenarios. Scenario #1 involves Shack-Hartmann Sensor "A" and Plenoptic Sensor #1. In Scenario #1, both wavefront sensors utilize the same MLA and image sensor in order to keep the hardware configuration as similar as possible. An objective lens with the

appropriate numerical aperture defined by Equation (19) is used for Plenoptic Sensor #1. Then the basic performance characteristics of Shack-Hartmann Sensor "A" and Plenoptic Sensor #1 are compared. In Scenario #2, Shack-Hartmann Sensor "A" remains unchanged. However, the MLA and objective lens in Plenoptic Sensor #2 are customized in order to more closely match the basic performance characteristics of Shack-Hartmann Sensor "A". Once again, the basic performance characteristics of the two sensors are compared.

2.3.2.1) Scenario #1

In Scenario #1 we compare the basic performance characteristics of Shack-Hartmann Sensor "A" to Plenoptic Sensor #1. This goal of this scenario is to keep the hardware configuration between the two sensors as similar as possible and then compare the resulting performance characteristics. Therefore, Plenoptic Sensor #1 uses the exact same MLA as Shack-Hartmann Sensor "A" but includes an appropriately matched objective lens defined by Equation (19). The hardware specifications used in Scenario #1 are defined in Table 2.1.

Table 2.1: Hardware utilized in Scenario 1

	Shack-Hartmann "A"	Plenoptic Sensor #1
Image sensor pixel size	5.5 μm	5.5 μm
Image sensor resolution	1820x1820 pixels	1820x1820 pixels
MLA pitch	300 μm	300 μm
MLA focal length	18.8 mm	18.8 mm
Beam diameter	10 mm	10 mm
Objective lens diameter	N/A	10 mm
Objective lens focal length	N/A	627 mm

Table 2.1: Hardware utilized in Scenario 1

Table 2.1 shows that an identical MLA is used for both wavefront sensors. In addition, the appropriately sized objective lens in this scenario for Plenoptic Sensor

#1 would be a 10 mm diameter lens with a 627 mm focal length. The image sensor pixel size of 5.5μm is based off the commercially available Allied Vision Technologies Prosilica GX1050 cameras. The MLA pitch and focal length are based off the commercially available Edmund Optics MLA #64-478. The resulting performance characteristics are defined in Table 2.2.

Table 2.2: Performance characteristics of Scenario 1

	Shack-Hartmann "A"	Plenoptic Sensor #1
Sensitivity	0.293 mrad	0.479 mrad
Maximum Tilt	8.00 mrad	7.97 mrad
Gradient Samples	1111	2975 (minimum)

Table 2.2: Performance characteristics of Scenario 1

The performance characteristics in Table 2.2 were calculated using Equations (25)-(30) as well as the hardware defined in Table 2.1. Table 2.2 gives insight as to how the objective lens in Plenoptic Sensor #1 changes the available gradient information provided by a common MLA between Shack-Hartmann Sensor "A" and Plenoptic Sensor #1. The wavefront tilt sensitivity is 40% greater with Shack-Hartmann Sensor "A" while the maximum wavefront tilt measurable, or dynamic range, is within 1% of each other. However, Shack-Hartmann Sensor "A" provides a minimum of 60% fewer gradient samples compared to Plenoptic Sensor #1. This is assuming a collimated beam, which correspondingly provides the minimum gradient samples in a Plenoptic Sensor. A minimum number is quoted because a Shack-Hartmann sensor has a fixed number of gradient samples equal to the sub-aperture count while the Plenoptic Sensor potentially increases in gradient samples as the complexity of the wavefront increases [36]. Scenario #1 is interesting because it describes the situation in which an existing Shack-Hartmann sensor can be re-tasked

quickly to perform as a Plenoptic Sensor. The simple addition of an objective lens to an existing Shack-Hartmann sensor as well an appropriate change of wavefront reconstruction algorithms is all that is needed to perform wavefront sensing with the newly created Plenoptic Sensor. Table #2 shows that even with a common MLA, it is possible to have two very different wavefront sensors that are more appropriately suited to different wavefront sensing conditions.

2.3.2.2) Scenario #2

In Scenario #2 we compare the basic performance characteristics of the previously used Shack-Hartmann Sensor "A" to the newly specified Plenoptic Sensor #2. The goal of this scenario is to match the basic performance characteristics of Shack-Hartmann Sensor "A" by modifying the hardware in Plenoptic Sensor #2. Scenario # 1 demonstrates that it would be unfair to compare Shack-Hartmann Sensor "A" to Plenoptic Sensor #1 due to the largely differing gradient measurements capable of the different sensors. Scenario #2 demonstrates that it is possible to have 2 very similar wavefront sensing capabilities by carefully designing Plenoptic Sensor #2 to match Shack-Hartmann Sensor "A". Table 2.3 describes the new hardware specifications for each wavefront sensor.

Table 2.3: Hardware utilized in Scenario 2

	Shack-Hartmann "A"	Plenoptic Sensor #2
Image sensor pixel size	5.5 µm	5.5 µm
Image sensor resolution	1820x1820 pixels	1820x1820 pixels
MLA pitch	300 µm	185 µm
MLA focal length	18.8 mm	11.5 mm
Beam diameter	10 mm	10 mm
Objective lens diameter	N/A	10 mm
Objective lens focal length	N/A	622 mm

Table 2.3: Hardware utilized in Scenario 2

Table 2.3 shows that the image sensor specifications as well as Shack-Hartmann Sensor "A" remain unchanged from Scenario 1. However, the MLA and objective lens in Plenoptic Sensor #2 have both been modified from Plenoptic Sensor #1. The resulting performance characteristics of Plenoptic Sensor #2 are calculated using Equations (28)-(30) and displayed below in Table 2.4.

Table 2.4: Performance characteristics of Scenario 2

	Shack-Hartmann "A"	Plenoptic Sensor #2
Sensitivity	0.293 mrad	0.297 mrad
Maximum Tilt	8.00 mrad	8.01 mrad
Gradient Samples	1111	1131 (minimum)

Table 2.4: Hardware utilized in Scenario 2

In Table 2.4, the wavefront tilt sensitivity, the maximum measurable tilt, and the total gradient samples between Shack-Hartmann Sensor "A" and Plenoptic Sensor #2 are very close to each other. If both wavefront sensors are sensing an identical wavefront, both will exhibit a distribution of light onto a similar number of pixels on the image sensor (resulting in a similar signal to noise ratio) but obviously in a very different image. This is true for wavefronts without significantly complicated distortions because the number of gradient samples provided by a Plenoptic Sensor tends to increase with wavefront complexity which would redistribute the incoming wavefront onto more image sensor pixels [36]. Scenario #2 demonstrates that it is possible to design a Plenoptic Sensor with very similar performance characteristics to a Shack-Hartmann sensor by modifying the MLA and objective lens in use. The MLA and objective lens defined in Table 2.3 for Plenoptic Sensor #2 are still reasonable and can be obtained commercially. However, strictly looking at these similar performance characteristics doesn't illustrate the more intricate differences between a

Shack-Hartmann sensor and Plenoptic Sensor. Section 2.3.3 takes a look at specific wavefront scenarios in order to illustrate how these wavefront sensors differ even if their performance characteristics are very similar.

2.3.3) Sample Wavefront Scenarios

Section 2.3.2 showed in Scenario #2 that it is simple to create a Plenoptic Sensor that can provide a very similar data set of gradient information to a Shack-Hartmann sensor. The comparison of the gradient information data sets is useful but doesn't address issues that frequently occur when performing wavefront sensing in strong atmospheric turbulence, as discussed in Section 1. The negative effects of strong atmospheric turbulence on the Shack-Hartmann sensor have been well studied throughout the years. In addition, advances have been made to help counteract and improve wavefront sensing despite the strong turbulence effects described in Section 1. For example, optical vortices and branch points are a naturally occurring phenomenon that can be generalized as a location with field amplitude of zero that is enclosed by a non-zero curl of the gradient [33][37]. It has been shown that the density of optical vortices as well as other large phase discontinuities increases as the propagation distance and atmospheric turbulence strength increases [37]. Plenty of research has demonstrated that it is still possible to use a Shack-Hartmann sensor to correctly identify the location of these phase discontinuities as well as reconstruct the highly distorted wavefront [32][35][38][39][40][41]. This is performed by first realizing that the wavefront should no longer be assumed to have a net zero value along a closed loop path of the 2D phase function. The "hidden phase" component contains a value that is typically ignored when performing a traditional least mean

square error reconstruction of the wavefront from the phase gradient information. To accurately perform wavefront reconstruction, the branch cuts can be located by examining the curl of the local phase gradient data. After noting the locations of the branch cuts and other large phase discontinuities, a least mean square error reconstructor can be effectively applied into segmented regions where the phase remains continuous.

However, these advanced methods to reconstruct highly distorted wavefronts do not change the fundamental mechanisms of how a Shack-Hartmann sensor operates. Each sub-aperture in the Shack-Hartmann sensor produces an intensity weighted average of the phase function across the sub-aperture. This is adequate for performing wavefront sensing in weak atmospheric turbulence because the centroid tilt (C-tilt) matches the intensity weighted average gradient (G-tilt), as discussed in Section 2.3. However, as the atmospheric turbulence strength increases, the issue of C-tilt and G-tilt anisoplanatism arises [32]. The Fried coherence length begins to approach the length of the sub-aperture and the density of large phase discontinuities also increases [32][37]. Figure 2.13 presents a wavefront with significant distortions on the order of the sub-aperture length and the respective sensing behavior of a Shack-Hartmann wavefront sensor and Plenoptic Sensor.

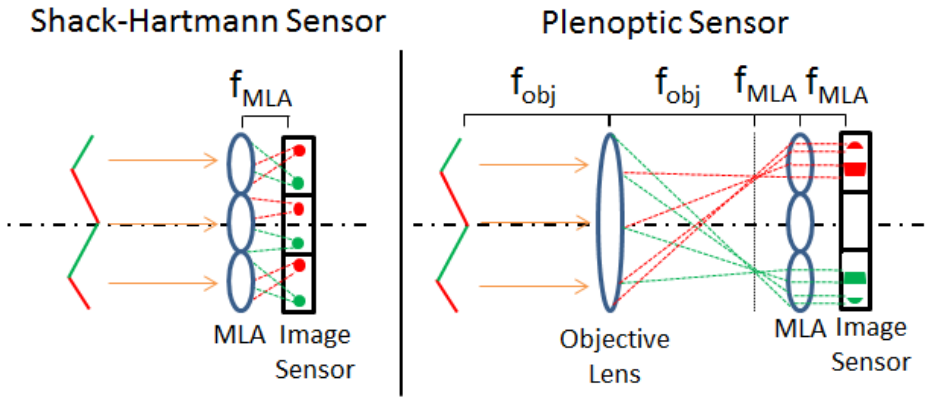

Figure 2.13: Significant wavefront distortion scenario [48].

Figure 2.13 is a simplified diagram illustrating an identical distorted wavefront entering a Shack-Hartmann sensor and a Plenoptic Sensor. The wavefront has large phase changes within the scale of the sub-aperture length. This is a commonly occurring scenario as the strength of atmospheric turbulence and the propagation distance increases which causes a reduction in the Fried coherence length [37]. The high spatial frequency of the abrupt wavefront changes causes many problems for the Shack-Hartmann sensor. As shown on the left side of Figure 2.13, the individual sub-apertures in the Shack-Hartmann sensor perform an intensity weighted average gradient leading to multiple interfering centroids on the image sensor. Unfortunately, the hardware design of the Shack-Hartmann sensor does not give a way to make use of this information. If a traditional "center of mass" centroiding algorithm is applied to calculate the center of the intensity, the weighted average of the multiple interfering centroids will be calculated which does not correctly represent the gradient of the wavefront. More advanced algorithms have been developed to correctly identify the centroid on a Shack-Hartmann sensor in tough wavefront sensing situations. For example, matched filtering, sub-aperture cross correlation, and iteratively weighted centroiding algorithms help to identify the centroid in noisy conditions caused by situations such as turbulence induced intensity scintillation [42][43]. In addition, clever algorithms can extend the dynamic range of the Shack-Hartmann sensor by allowing the centroids to shift outside the normally allocated image sensor area denoted by the corresponding sub-aperture [44]. However, these algorithms do not help when there are multiple centroids or if there is

a complete null in intensity, both of which can be caused by large gradient changes within the length of a sub-aperture.

The hardware design of the Plenoptic Sensor allows for the complete reconstruction of the wavefront presented in Figure 2.13. The different angular components are automatically separated by the Fourier transform of the objective lens. As a result, there are no interference issues with the wavefront as it is imaged by the sub-apertures. The Plenoptic image on the right side of Figure 2.13 shows that the full wavefront is imaged correctly onto the image sensor. From here, a variety of Plenoptic wavefront reconstruction algorithms can be used to reconstruct the wavefront at the front focal plane of the objective lens despite there being significant wavefront distortions present within the length of the sub-aperture.

Another scenario that differentiates the operating mechanism of the Shack-Hartmann sensor and the Plenoptic Sensor is the presence of a second incoming wavefront. A second identical wavefront can be produced by splitting an incoming beam and directing both beams into the wavefront sensor with a small tilt separating each one. This 2-beam scenario is a simplified scenario in which 2 geometrically overlapped patches of light are incident on the wavefront sensor. One detrimental effect of atmospheric turbulence (mentioned in Section 1) is beam breakup where the overall coherence of the beam is lost and the beam is "broken up" into separate patches [1][39][45]. The separate patches can be treated as individually propagating beams that have the potential to geometrically overlap and interfere with each other [36]. In a sense, this 2-beam scenario attempts to mimic a scenario in which there are 2 separate patches of light geometrically overlapped on top of each other prior to

entering the wavefront sensor. Figure 2.14 shows how each wavefront sensor handles this scenario.

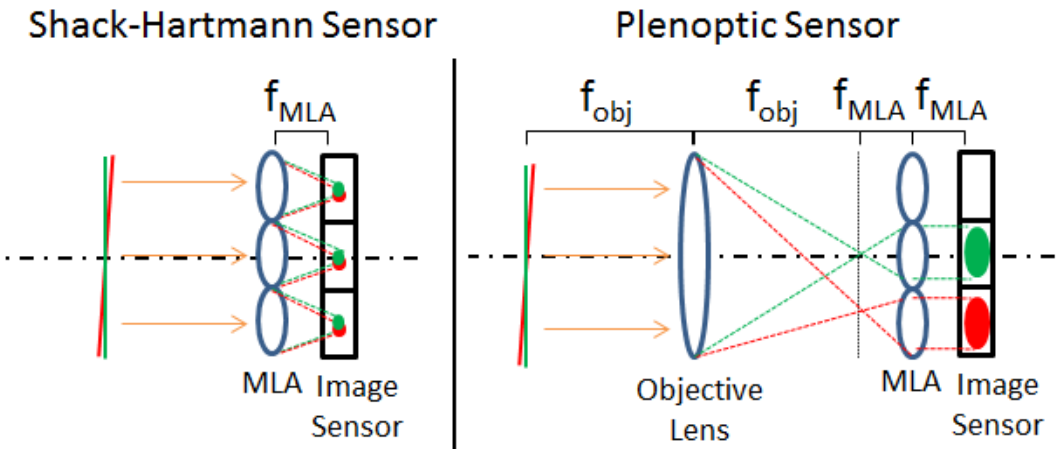

Figure 2.14: Double beam scenario [48].

The two beams in Figure 2.14 (indicated in green and red) are identical with the exception of a small global tilt. The Shack-Hartmann sensor on the left side of Figure 2.14 can only measure the average of the two incoming wavefronts. Each sub-aperture calculates the intensity weighted average gradient of the two incoming wavefronts which leads to either two separate centroids on the image sensor or interfering focal spots. This does not accurately represent the 2-beam scenario and is a simplified example of how the Shack-Hartmann sensor fails to measure geometrically overlapped patches of light that are induced by strong atmospheric turbulence.

The Plenoptic Sensor on the right side of Figure 2.14 is able to adapt to this 2-beam scenario. Although the Shack-Hartmann sensor has a fixed number of sub-apertures directly corresponding to a fixed gradient sample count, the Plenoptic Sensor effectively doubles its phase gradient sample count in the presence of a second

beam. The red and green wavefronts are separated into different sub-apertures corresponding to their angular spectrum. If the tilt separating the two wavefronts is greater than or equal to the Plenoptic Sensors sensitivity, then the full wavefront information can be retrieved for both incoming wavefronts. This simple example demonstrates that geometrically overlapped patches of light do not inherently pose a significant problem for the Plenoptic Sensor.

2.3.4) Indoor Experimental Images

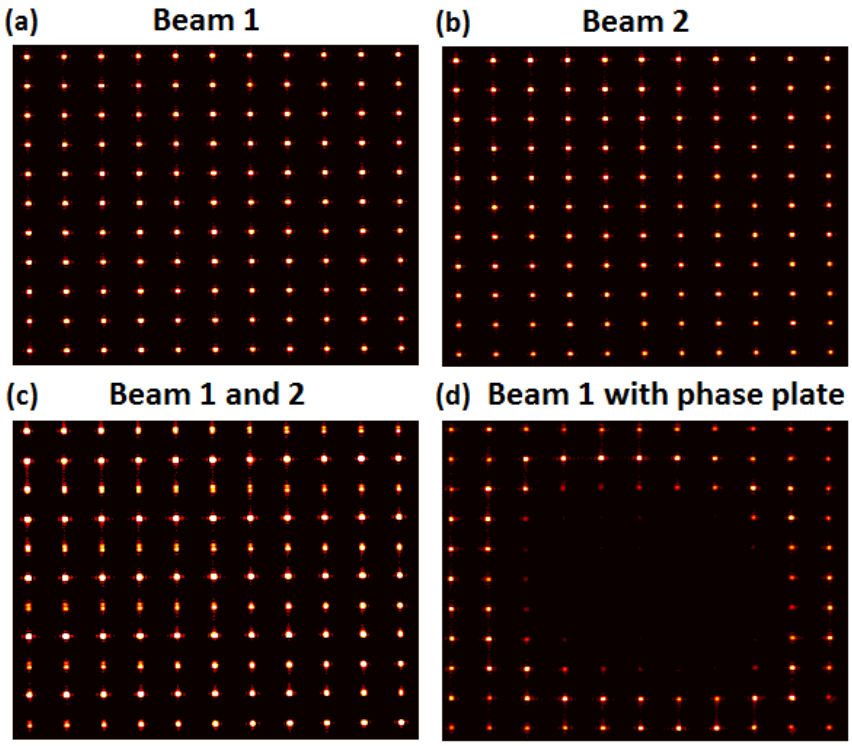

Figure 2.15: Shack-Hartmann sensor images (a) Beam 1; (b) Beam 2; (c) Beam 1 and 2; (d) Beam 1 with vortex phase plate [48].

Figure 2.15 are experimental images obtained with an AVT Prosilica GX1050 camera with a resolution of 1024x1024 and a 5.5 μm pixel size. The MLA is 10x10 mm in total size and has a 300 μm pitch with a focal length of 18.8 mm. The MLA is

positioned 1 focal length away from the image sensor and therefore represents a Shack-Hartmann sensor configuration. The laser is a 633 nm HeNe laser that is expanded to roughly the size of the MLA and then split into 2 separate beams. The 2 beams are then geometrically overlapped and introduced into the Shack-Hartmann sensor with a small global tilt (~1 mrad) differentiating them. Figure 2.15 only shows a smaller portion (600x600 pixels) of the image sensor for ease of viewing.

Figure 2.15(a) and Figure 2.15(b) are images of Beam 1 and Beam 2 individually cast onto the Shack-Hartmann sensor. Beam 1 and Beam 2 are collimated beams from an identical laser source with the only differing quality being a small global tilt separating them (~1 mrad). As expected, Figure 2.15(a) and 2.15(b) show the familiar symmetrical grid of a Hartmannogram with a very uniform pattern. The 2D correlation between the 2 images is ~97% after shifting Figure 2.15(b) down by 4 pixels to accommodate for the ~1 mrad tilt. This indicates that the wavefront of Beam 1 and Beam 2 within the selected region of interest is essentially identical with the exception of the global ~1 mrad tilt. An ordinary "center of mass" centroiding algorithm would have no problem identifying the centroids in Figure 2.15(a) and Figure 2.15(b) due to the well-defined focal spots. In addition, a least mean square error reconstructor or other wavefront reconstruction method can use the local gradient tilts provided by the centroids to reconstruct the full wavefront.

Figure 2.15(c) represents the 2-beam scenario in which Beam 1 and Beam 2 are simultaneously cast onto the Shack-Hartmann sensor. The presence of 2 beams results in centroids that are interfering both constructively and destructively which leads to areas of over exposure and under exposure. In addition, some sub-apertures show the

presence of 2 separate centroids from the 2 incoming beams. As expected, it is impossible to separate Beam 1 and Beam 2 in Figure 2.15(c) because the Shack-Hartmann sensor can only calculate the intensity weighted average gradient of the 2 incoming beams. The fixed gradient sample size does not allow for the complexity of this scenario to be accurately represented and therefore wavefront reconstruction would not lead to a correct result.

Figure 2.15(d) represents Beam 1 with the insertion of an RPC Photonics VP-m633 vortex phase plate. The chosen vortex phase distortion features a vortex of topological charge +4 with four equally spaced 2π branch cuts, as highlighted in red in Figure 2.16(d). The center of the vortex is clearly identified by the large area of intensity null in the center of Figure 2.15(d). It has been shown that successful vortex phase reconstruction is possible by locating areas of branch points or branch cuts and then performing a traditional wavefront reconstruction inside areas where the wavefront phase function remains continuous [34][35][38][39][40][41]. However, it is understood that the presence of branch points, branch cuts, and other complex phase functions may lead to a reduction in phase gradient information. These complex phase functions often lead to low or no intensity in the corresponding sub-apertures, which is clearly shown by the large intensity null in Figure 2.15(d). The null of intensity where a centroid should normally be present directly corresponds to a reduction in the phase gradient information provided by the Shack-Hartmann sensor. Although the surrounding gradient information may still be adequate to reconstruct the full wavefront, the reduction of gradient samples in the presence of complicated wavefronts is not a desired quality of any wavefront sensor.

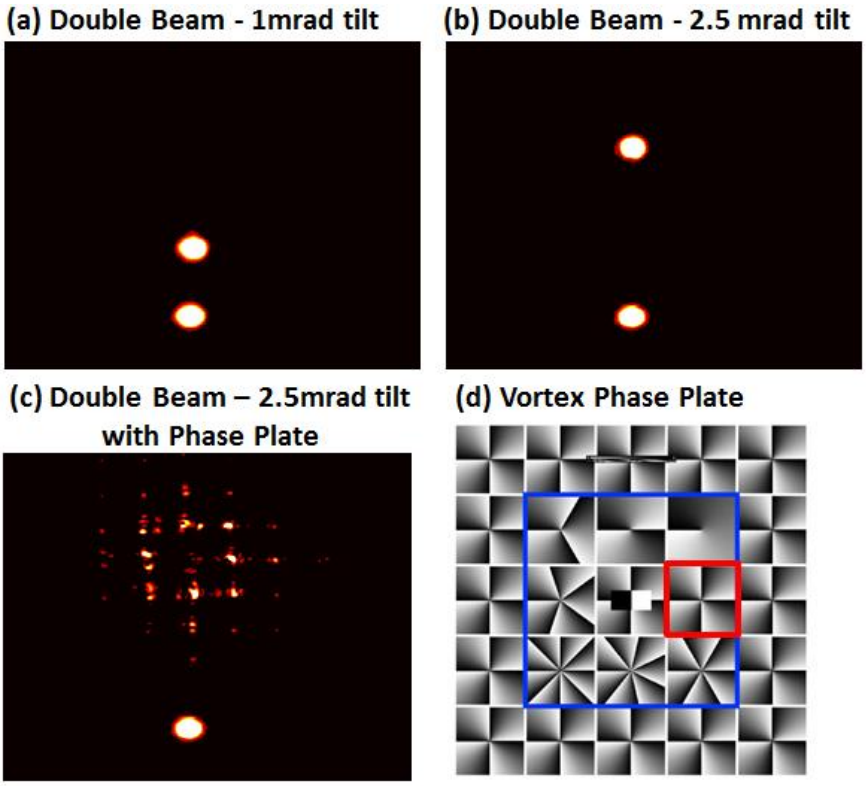

Figure 2.16: (a) Plenoptic image of double beam with small tilt; (b) Plenoptic image of double beam with large tilt; (c) Plenoptic image of double beam with large tilt and phase plate; (d) vortex phase plate layout [48].

Figure 2.16 contains 3 experimental images from a Plenoptic Sensor with a 300μm pitch MLA with focal length of 18.8 mm (identical to the Shack-Hartmann sensor used in Figure 2.15) as well as a matching objective lens satisfying the numerical aperture requirements from Equation (19). The AVT Prosilica GX1050 camera with a resolution of 1024x1024 and a 5.5 μm pixel size is retained from the setup used in Figure 2.15. In addition, the 2-beam scenario and vortex phase plate utilized in Figure 2.15 is also reused in Figure 2.16. The similarity in hardware configuration of this Plenoptic Sensor in relation to the Shack-Hartmann sensor matches Scenario 1 from Section 2.3.2.

Figure 2.16(a) and Figure 2.16(b) are the Plenoptic images of Beam 1 and Beam 2 in the 2-beam scenario with a tilt separation of ~1 mrad and ~2.5 mrad, respectively. Due to the wavefront tilt differences, Beam 1 and Beam 2 are separated into different sub-apertures and imaged onto a different portion of the image sensor despite being geometrically overlapped before entering the Plenoptic Sensor. This results in the doubling of phase gradient information provided by the Plenoptic Sensor because there is now double the amount of illuminated pixels in comparison to a single collimated beam. Contrastingly, the geometrically overlapped beams in Figure 2.15(c) results in misleading information for a Shack-Hartmann sensor. Figure 2.16(c) shows the same vortex phase plate (highlighted in Figure 2.16(d)) placed in front of one of the beams. It is clear from Figure 2.16(c) that the upper beam has undergone a phase distortion due to the vortex phase plate while the lower beam remains undistorted and collimated. In addition, it is possible to analyze just the upper beam's phase distortion while ignoring the presence of the lower beam. If we remove the lower beam from the Plenoptic images, we can determine that the upper beam has changed from ~1570 illuminated image sensor pixels in the collimated example of Figure 2.16(b) to ~3780 illuminated image sensor pixels in the vortex phase plate example of Figure 2.16(c). This indicates that the increased complexity of the wavefront caused by the vortex phase plate has resulted in an increase of 140% more phase gradient samples. The tilt separation of the upper and lower beams in Figure 2.16(c) allows for the Plenoptic Sensor to reconstruct the distorted upper beam by a process of identifying the branch cuts and reconstructing the continuous portions of the wavefront through a least mean square error reconstructor [17][36].

Reconstructing each beam separately is possible until the tilt separation becomes too small and the phase distortions result in light from each beam overlapping onto shared sub-apertures, therefore making it impossible to determine which patches of light arise from which beam. This is why Figure 2.16(c) borrows the ~2.5 mrad separation from Figure 2.16(b) as the starting wavefront scenario as opposed to the ~1mrad separation example in Figure 2.16(a).

2.3.5) Outdoor Experimental Images

Experimental images have been taken in an outdoor environment to differentiate the data provided by a Shack-Hartmann sensor and a Plenoptic Sensor. The experimental images provided in this section were obtained from the Townes Institute Science and Technology Experimentation Facility (TISTEF) range at the Kennedy Space Center. The purpose of these field images is to compare the Shack-Hartmann sensor and the Plenoptic Sensor in real world atmospheric turbulence. In addition, these field images are intended to show the relevancy of the scenarios mentioned in Section 2.3.3 and 2.3.4. The laser source is a 640 nm Coherent fiber laser that is collimated and located 850 m away from the wavefront sensors. An identical setup to Section 2.3.4 is used for the Shack-Hartmann sensor and Plenoptic Sensor with an AVT Prosilica GX1050 camera as well as a 300 μm pitch MLA with a focal length of 18.8 mm. However, in order to collect as much of the wavefront as possible, a 6 inch Celestron Cassegrain telescope with an adjustable focus is used as a collection aperture for the Shack-Hartmann sensor and the main objective lens of the Plenoptic Sensor. In addition, a BLS900 Scintec scintillometer is used to characterize

the strength of turbulence by providing C_n^2 measurements along the same propagation channel.

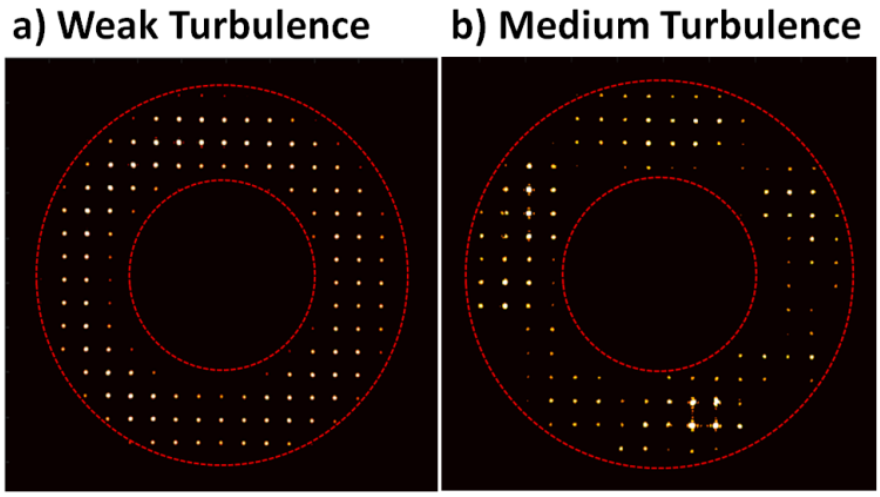

Figure 2.17: Shack-Hartmann sensor images under: (a) weak turbulence; (b) medium turbulence [48].

Figure 2.17 shows two images from the Shack-Hartmann sensor taken under two different turbulence strengths [48]. In both images, the red circular outlines show the wavefront being apertured by the familiar shape of a Cassegrain telescope. Figure 2.17(a) is a Shack-Hartmann sensor image taken under weak atmospheric turbulence conditions ($C_n^2 \sim 10^{-15}$). The centroids in this image show sharp focal spots being produced by each sub-aperture which presents no trouble for acquiring the location of the centroid as well as the calculating the local phase gradients. Figure 2.17(b) is a Shack-Hartmann sensor image taken under medium atmospheric turbulence conditions ($C_n^2 \sim 10^{-14}$). In this image, many but not all of the centroids are still sharp focal spots and can be easily identified. As expected, the increase in the atmospheric turbulence strength has led to intensity scintillation across the wavefront, as evident by the local regions of high intensity (oversaturated focal spots) and low intensity

(dark and hard to identify focal spots). Various algorithms can be applied in order to help identify the centroids in the regions of low signal to noise ratio caused by scintillation [42][43]. Another point to note is that there aren't many regions of complete intensity null or double focal spots caused by multi-beam interference. As a result, medium turbulence (found in ground to ground as well as astronomical optical situations) does not nullify the effectiveness of a Shack-Hartmann sensor in performing wavefront reconstruction, although smarter reconstruction algorithms may be necessary to help deal with intensity scintillation.

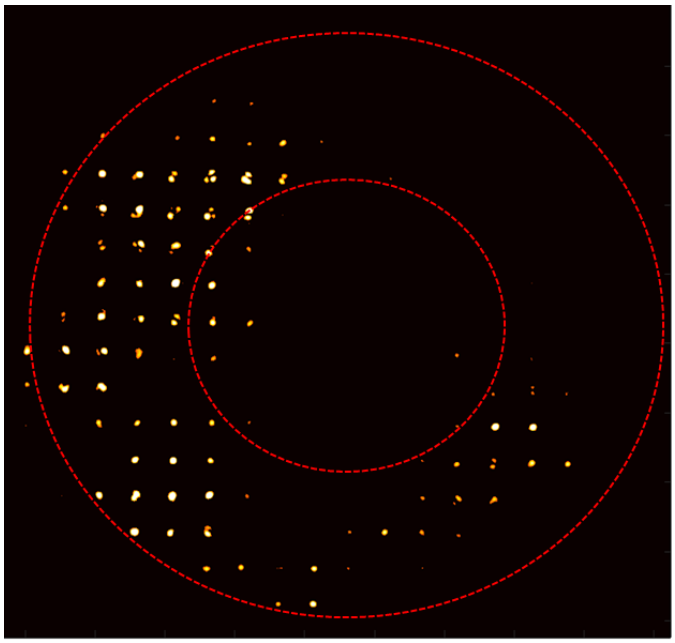

Figure 2.18: Shack-Hartmann sensor image under strong atmospheric turbulence [48].

Figure 2.18 is a familiar image of a Shack-Hartmann sensor operating under strong atmospheric turbulence conditions ($C_n^2 \sim 10^{-13}$) [48]. The effects of strong atmospheric turbulence on a Shack-Hartmann sensor are well researched and several expected consequences can be found in Figure 2.18. First, the intensity scintillation

has become so prominent that there are huge areas of the wavefront with zero intensity. The regions of zero intensity can be caused by interference effects such as those described in Figure 2.18, turbulence generated optical vortices and branch points similar to the example in Figure 2.15(d), or from simply a lack of field intensity in this area. The Shack-Hartmann sensor has no way to differentiate what is happening in this scenario and therefore the regions of intensity null directly correlate to a loss of phase gradient information. Second, there are several areas on the image sensor with 2 or 3 closely located intensity patches focused by a single sub-aperture. These multiple focal spot areas represent a scenario similar to Figure 2.13 where there are large changes in the wavefront gradient within the length of a sub-aperture. In addition, the multiple focal spot areas could also indicate multiple overlapping patches of light similar to the scenario in Figure 2.14. Clever centroiding algorithms do not help resolve the presence of these multiple focal spots so the wavefront gradient remains undetermined in the affected sub-apertures.

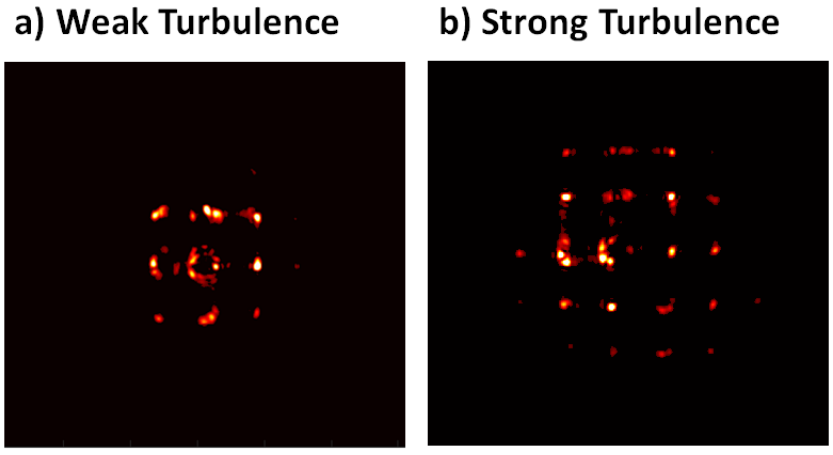

Figure 2.19: Plenoptic images under: (a) weak turbulence; (b) strong turbulence [48].

Figure 2.19 shows Plenoptic images under weak ($C_n^2 \sim 10^{-15}$) and strong ($C_n^2 \sim 10^{-13}$) atmospheric turbulence conditions [48]. Figure 2.19 is a Plenoptic image cropped down to a smaller 7x7 sub-aperture count area in order show only the relevant illuminated areas. In comparison, Figure 2.17 and Figure 2.18 in the Shack-Hartmann sensor configuration feature a roughly 17x17 illuminated sub-aperture area. In Figure 2.19(a), the Plenoptic image is mainly contained to the inner 3x3 sub-apertures. This correctly represents the weak turbulence scenario because the incoming wavefront only encounters small phase changes that can be characterized by the inner most sub-apertures. The wavefront in Figure 2.19(a) can be reconstructed through several different single wavefront reconstruction algorithms for the Plenoptic Sensor [17][20][25]. Contrastingly, Figure 2.19(b) shows a Plenoptic image under strong turbulence illuminating many more sub-aperture elements, although the illuminated sub-aperture count is still far from the full 17x17 sub-apertures utilized in Figure 2.17 and Figure 2.18. This correctly represents the strong turbulence scenario because the incoming wavefront now encounters large phase changes (i.e. local tilts) which would redirect light into sub-apertures further away from the optical axis. Figure 2.19(b) is examined in more detail below in Figure 2.20.

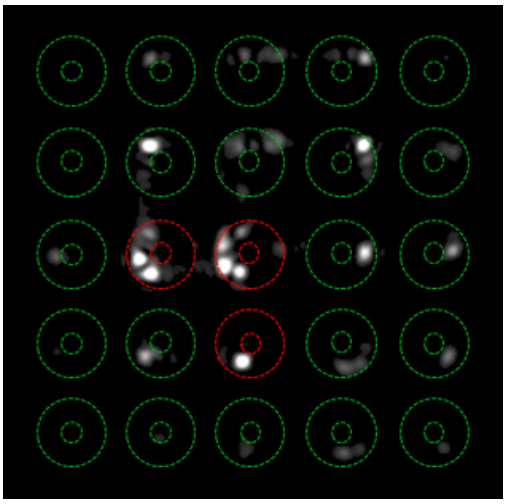

Figure 2.20: Zoomed in Plenoptic image from Figure 2.19(b) highlighting the geometrically overlapped patches of light [48].

Figure 2.20 is a further zoomed in version of the strong atmospheric turbulence example in Figure 2.19(b) [48]. A Cassegrain telescope mask is overlaid on top of the location of each sub-aperture in order to clarify the boundaries of the sub-apertures. The 3 red Cassegrain masks (as opposed to the other green Cassegrain masks) mark particular sub-apertures that are of interest. In each of these 3 red sub-apertures, there is a bright patch of light appearing in the same geometric location (bottom left corner). This indicates a geometrical overlap (at the plane of wavefront reconstruction) of 3 different patches of light with different angular spectrum. This is a real world example of overlapping light patches from the same incoming wavefront and is analogous to the 2-beam scenario presented in Figure 2.14. In a Shack-Hartmann sensor, this would lead to either multiple centroids within a sub-aperture or interference effects. However, the Plenoptic Sensor is able to separate the overlapped patches of light based on their angular spectrum and preserve the full wavefront information for further analysis. A single wavefront reconstruction can be performed

by intensity ranking or intensity averaging the overlapped patches of light, as utilized in the Graph Reconstruction in Section 2.2.2. This would be the more common scenario for an adaptive optics system requiring rapid wavefront reconstruction and correction. On the other hand, a more thorough multiple wavefront reconstruction algorithm can also be performed to more accurately characterize wavefronts of this complexity [17][36].

3) Experimental Results

3.1) Indoor lab experiments

An indoor test bench was established to demonstrate the Plenoptic Sensor in a controlled environment.

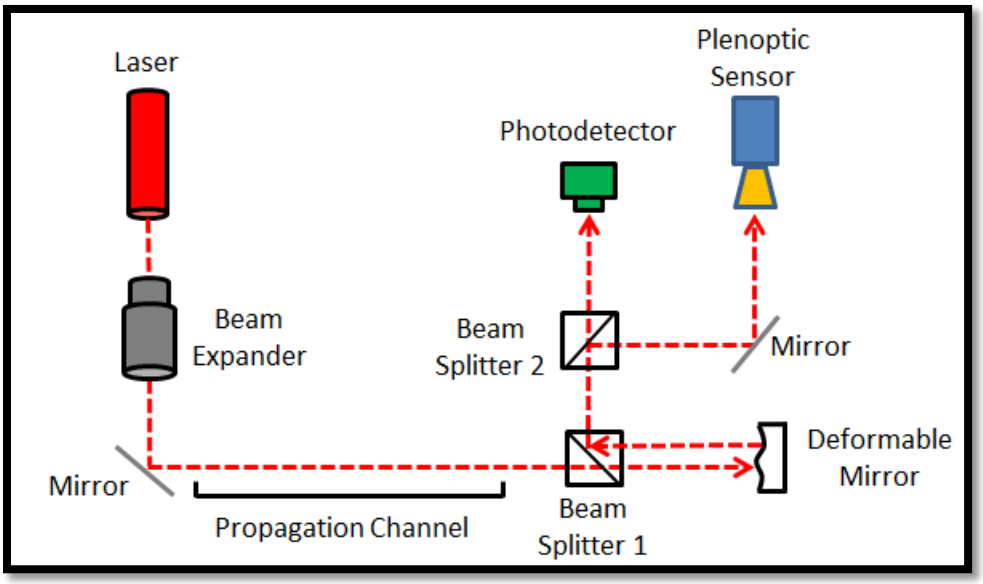

Figure 3.1.1: Diagram of indoor experimental setup.

The above configuration in Figure 3.1.1 illustrates the basic layout of our indoor experiments. The laser used in our experiments is a 633 nm HeNe laser that enters a beam expander prior to entering the propagation channel. Although the propagation channel is empty in Figure 3.1.1, the denoted area marks where static or dynamic turbulence is added to cause distortions to the wavefront. The beam passes through Beam Splitter 1, is incident on the deformable mirror, and is reflected back to Beam Splitter 1. The beam is then diverted towards Beam Splitter 2 where half the

beam passes through towards a photodetector and the other half is directed to the Plenoptic Sensor.

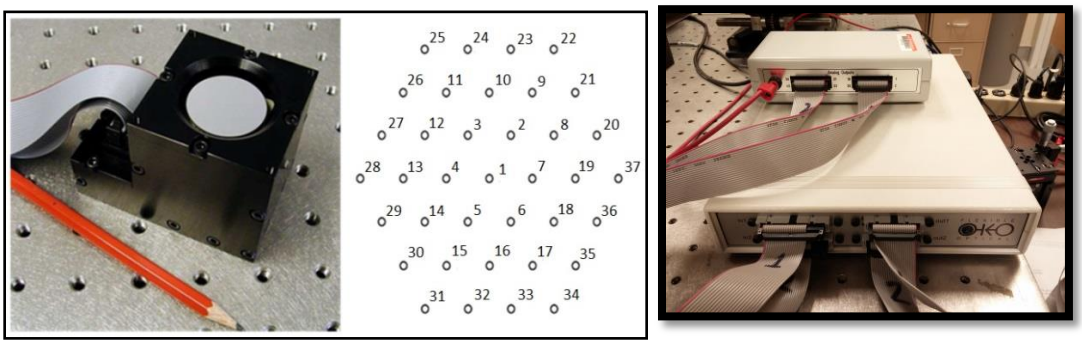

Figure 3.1.2: OKO Technologies deformable mirror hardware.

Figure 3.1.2 is the deformable mirror hardware that is used in our experiments. We use a 30 mm 37-channel piezoelectric deformable mirror built by OKO Technologies. The left side of Figure 3.1.2 is a picture of the deformable mirror (with a pencil for scale) and the hexagonal layout of the 37 actuators. The actuators are positioned with an inter-actuator pitch of 4.3 mm and have a maximum stroke of 8 μm. However, the maximum inter-actuator stroke (maximum stroke between 2 adjacent actuators) is limited to 1.5 μm. In addition, hysteresis effects are present in any piezoelectric device and must be taken into consideration when controlling the surface of the mirror [46]. The right side of Figure 3.1.2 is the hardware used to control the deformable mirror. The OKO Digital to Analog converter (DAC) has 40 channels with 12 bit voltage resolution (0 to 4095) and receives its commands from a computer. Underneath the OKO DAC is the OKO DC High Voltage amplifier which accepts up to 40 channels from the OKO DAC and produces a voltage anywhere from

0 to 300 V. The OKO amplifier then outputs the individual channel voltages to the deformable mirror in order to control each individual mirror actuator.

3.1.1) Adaptive optics correction of static distortions

In order to validate the wavefront reconstruction methods of the Plenoptic Sensor, experimental results were first obtained by performing wavefront reconstruction for static cases. One reason for performing the adaptive optics (AO) correction for static distortions is to verify that the Plenoptic Sensor can perform an accurate wavefront reconstruction. This is done by producing a known wavefront distortion (with the use of the deformable mirror) and independently comparing this known distortion to the reconstructed wavefront performed with the Plenoptic Sensor. In addition, the AO correction for static distortions is used to verify that our indoor experimental hardware is properly calibrated for performing wavefront correction. This includes verifying that the alignment of the beam and the orientation of the deformable mirror are appropriately configured. Once AO correction can be accurately performed for static distortions, more advanced real-time AO corrections can be attempted to counteract dynamic turbulence.

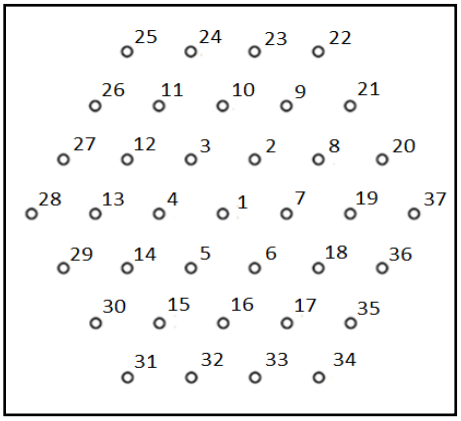

Figure 3.1.3: Actuator map of OKO 37-channel deformable mirror.

Actuator #	Radius	Theta	**Actuator #**	Radius	Theta
1	0	0	**20**	0.8819	0.3335
2	0.3333	π/3	**21**	0.8819	0.7137
3	0.3333	2π/3	**22**	1	π/3
4	0.3333	π	**23**	0.8819	π/2 – 0.1901
5	0.3333	4π/3	**24**	0.8819	π/2 + 0.1901
6	0.3333	5π/3	**25**	1	2π/3
7	0.3333	0	**26**	0.8819	π – 0.7137
8	0.5774	π/6	**27**	0.8819	π – 0.3335
9	0.6666	π/3	**28**	1	π
10	0.5774	π/2	**29**	0.8819	π + 0.3335
11	0.6666	2π/3	**30**	0.8819	π + 0.7137
12	0.5774	5π/6	**31**	1	4π/3
13	0.6666	π	**32**	0.8819	3π/2 – 0.1901
14	0.5774	7π/6	**33**	0.8819	3π/2 + 0.1901
15	0.6666	4π/3	**34**	1	5π/3
16	0.5774	3π/2	**35**	0.8819	2π – 0.7137
17	0.6666	5π/3	**36**	0.8819	2π – 0.3335
18	0.8819	11π/3	**37**	1	0
19	0.6666	0			

Table 3.1: Coordinates of the 37 actuators on the OKO deformable mirror.

The location of each deformable mirror actuator is mapped to establish full control of the shape of the deformable mirror. Figure 3.1.3 shows the hexagonal layout of the deformable mirror actuators behind the 30 mm diameter mirror surface. In Table 3.1, a more precise mapping of each actuator is recorded using its radius and angle theta with respect to the center Actuator #1. This coordinate system makes it simple to recreate Zernike polynomials, which are a sequence of orthogonal polynomials over a unit circle, with their two variables being the radius and theta. In addition, wavefront aberrations often take the form of these Zernike polynomials, such as coma and astigmatism. Once the location of these actuators is documented, it is simple to create these Zernike polynomials on the surface of the deformable mirror.

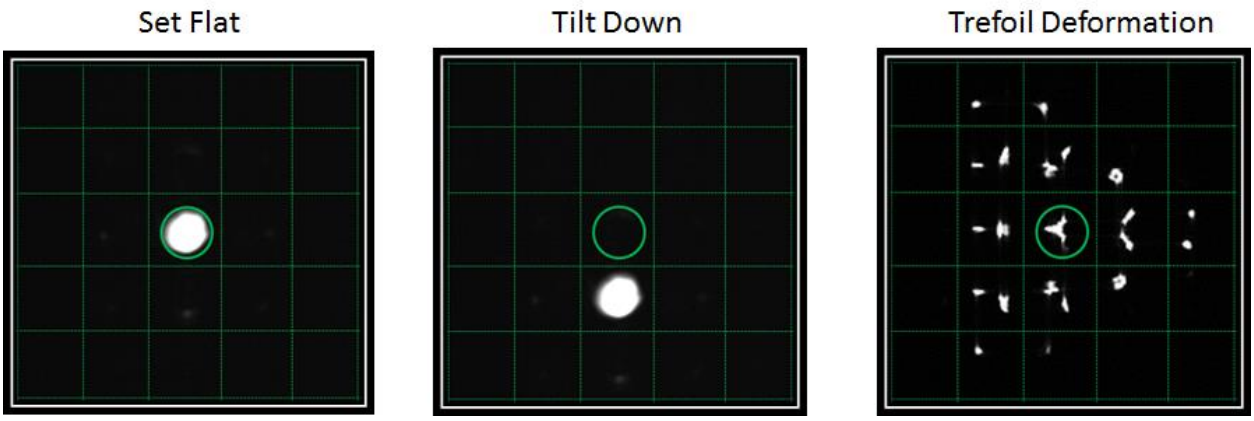

Figure 3.1.4: Plenoptic images of different wavefront deformations.

Figure 3.1.4 shows Plenoptic Images of 3 different wavefronts being imaged by the Plenoptic Sensor. Each Plenoptic Image has a green grid mask overlaid to highlight where the boundaries of the MLA sub-apertures are located. The images were taken using an AVT Bonito CL400 Camera Link camera as the image sensor and a 633 nm HeNe laser expanded to 20 mm is used as the laser source. The Plenoptic Sensor in this example uses a MLA with a size of 10x10 mm, pitch of 500 μm, and a focal length of 46.7 mm. An appropriately sized objective lens is used that obeys the criteria specified in Equation (19). The hardware layout closely follows the diagram in Figure 3.1.1. The deformable mirror is located at the front focal plane of the objective lens which matches the plane of wavefront reconstruction from the Plenoptic Images.

The undistorted beam produces the image on the left in Figure 3.1.4. This is done by setting the deformable mirror to a flat state (all actuator voltages set to zero) which mimics a flat mirror. To no surprise, the undistorted beam is incident on the center MLA sub-aperture and remains circular in shape. The middle image in Figure

3.1.4 shows the result of tilting the beam downwards. As a result, the beam is shifted downwards to an adjacent MLA sub-aperture but remains circular. The right image in Figure 3.1.4 is the result of applying the Zernike Trefoil deformation $Z(3,3) = \rho^3 cos(3\theta)$ to the deformable mirror. These Plenoptic Images are raw images from the Plenoptic Sensor and can be analyzed with the algorithms discussed in Section 2.2 to recreate the actual wavefront.

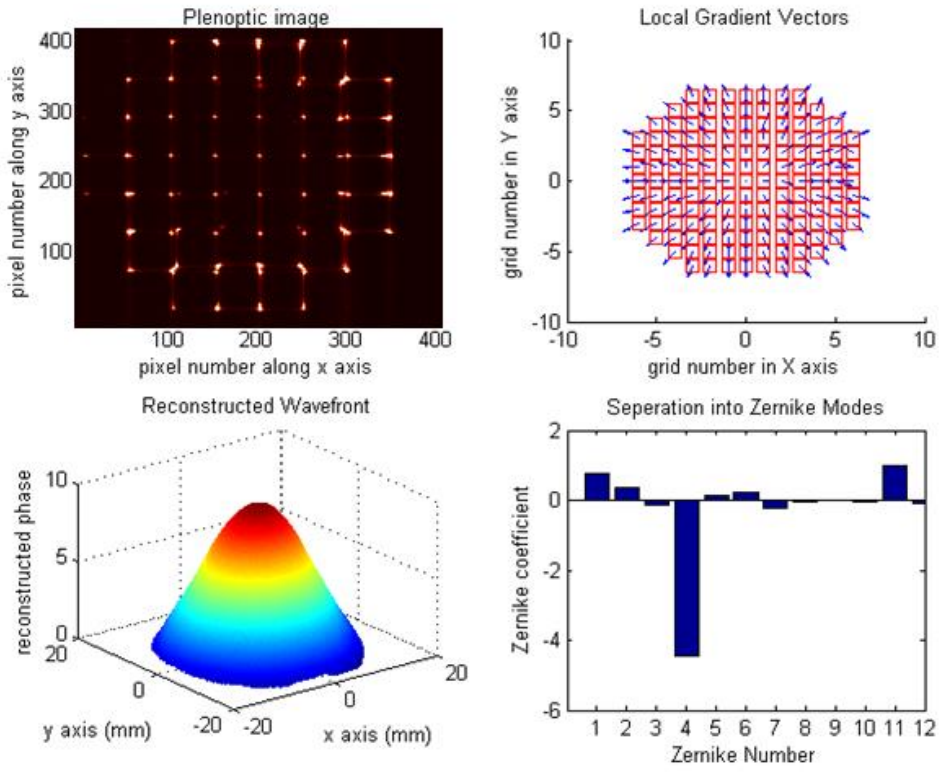

Figure 3.1.5: Plenoptic image and reconstruction of defocus deformation.

The top left image in Figure 3.1.5 is a Plenoptic Image after a Zernike Defocus deformation $Z(0, 2) = 2\rho^2 - 1$ is applied to the deformable mirror. The intensity from the beam is now distributed evenly radially outwards from the center MLA sub-aperture. The top right image in Figure 3.1.5 shows many small red boxes

which are representative of checkerboard units from the checkerboard reconstruction algorithm discussed in Section 2.2. In addition, inside each red checkerboard unit there is a gradient vector. Unsurprisingly, for the defocus deformation, all the calculated gradient vectors from processing the Plenoptic Image are pointing radially outwards away from the center. The bottom left image is the reconstructed wavefront using the checkerboard reconstruction algorithm and it correctly represents the shape of a defocus deformation. The bottom right image is a result of decomposing the reconstructed wavefront into its Zernike components, and it correctly predominantly matches a defocus deformation (Zernike number 4).

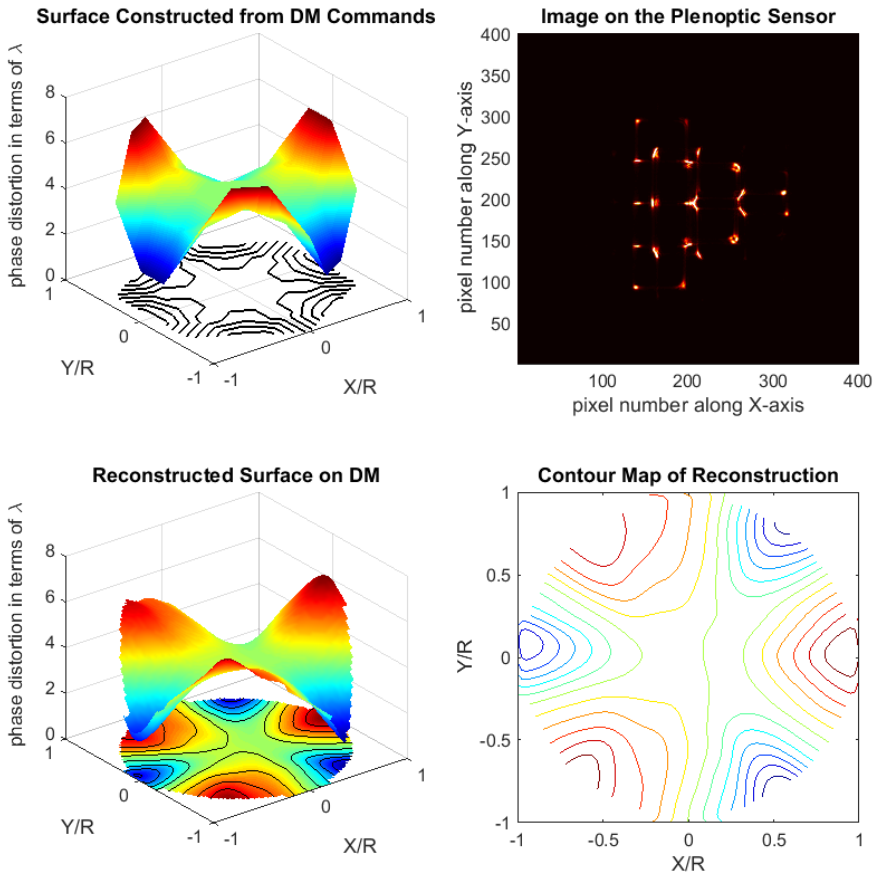

Figure 3.1.6: Plenoptic image and reconstruction of trefoil deformation.

The top left graph in Figure 3.1.6 represents a Trefoil Zernike deformation $Z(3,3) = \rho^3 cos(3\theta)$ that has been extrapolated over the 37-actuators of the OKO deformable mirror. This mapped surface represents the exact commands sent to the deformable mirror and closely matches the actual surface of the deformable mirror. The image in the top right of Figure 3.1.6 is the Plenoptic Image on the image sensor created by applying the Trefoil deformation to the OKO deformable mirror. The bottom left graph and bottom right graph in Figure 3.1.6 shows the wavefront reconstruction of the Plenoptic Image performed by the checkerboard reconstruction algorithm. By comparing the top left and bottom left graphs in Figure 3.1.6, it is easy to see that the wavefront reconstruction closely resembles the actual commanded shape given to the deformable mirror. Table 3.2 below shows the voltage values (with 0 being the lowest voltage and 4095 being the highest voltage) that are applied to the deformable mirror and also those voltages values that are reconstructed from the Plenoptic Image. The larger mismatches between the applied voltage and reconstructed voltage occur in the outer ring of actuators. For example, Actuator #33 had an applied voltage of 0 while the reconstructed voltage was 1396. However, the correlation between the applied voltage and reconstructed voltage remained 93.2% which translates to a respectable 0.62 λ RMS error. The error can be attributed to factors such as deformable mirror hysteresis, misalignment in the optical system leading to larger errors on the edge of the wavefront, or a limited number of discrete actuators [17][46].

Actuator #	Applied Voltage	Reconstructed Voltage	**Actuator #**	Applied Voltage	Reconstructed Voltage
1	2048	2052	**20**	0	638
2	2048	1871	**21**	0	0
3	2048	1854	**22**	2047	2063
4	2048	2281	**23**	4095	3579
5	2048	2103	**24**	4095	3844
6	2048	2174	**25**	2048	2258
7	2048	2314	**26**	0	256
8	1384	1258	**27**	0	1070
9	2048	1926	**28**	2047	2878
10	2711	2845	**29**	4095	3518
11	2048	2066	**30**	4095	3957
12	1384	1557	**31**	2048	2287
13	2048	2664	**32**	0	364
14	2711	2955	**33**	0	1396
15	2048	2275	**34**	2047	3269
16	1384	1416	**35**	4095	4095
17	2047	2794	**36**	4095	3343
18	2711	2992	**37**	2048	2042
19	2048	2434			

Table 3.2: Comparison of applied deformable mirror voltages to reconstructed voltages for a trefoil deformation.

The graph reconstruction algorithm (mentioned in Section 2.2.2) was also tested and calibrated for static wavefront reconstruction scenarios. This is especially important because the graph reconstruction algorithm inherently throws away some wavefront information in order to perform as quick of a wavefront reconstruction as possible. Figure 3.1.7 shows the result of the graph reconstruction algorithm when a Trefoil Zernike deformation $Z(3,3) = \rho^3 cos(3\theta)$ is applied to the OKO deformable mirror.

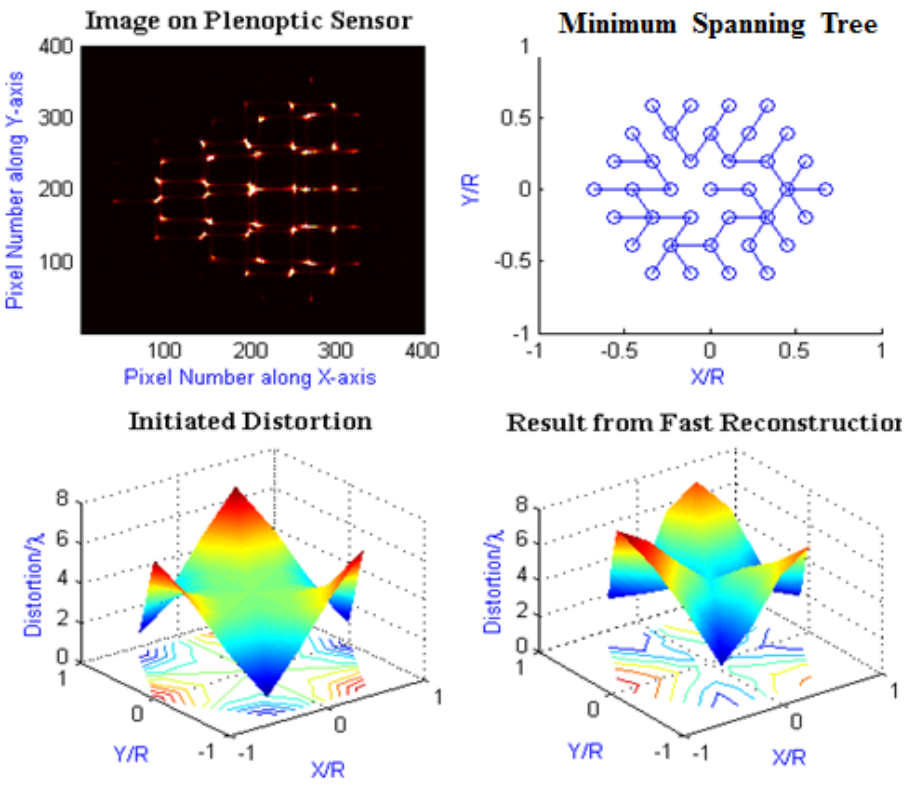

Figure 3.1.7: Tree reconstruction algorithm for trefoil deformation.

The top left image in Figure 3.1.7 is a Plenoptic image of the Trefoil deformation. The bottom left image in Figure 3.1.7 is a plot of the Trefoil deformation voltages sent to the deformable mirror. The top right image in Figure 3.1.7 is a tree graph showing the 37 nodes representing the 37 actuators on the OKO deformable mirror. The 36 selected edges from the graph reconstruction algorithm are also shown connecting the 37 actuators in a minimum degree spanning tree. The result of reconstructing the full wavefront using the 36 selected edges is shown in the bottom right image in Figure 3.1.7. The three-point symmetry of the Trefoil deformation is clearly visible in the reconstructed wavefront and matches the reference wavefront in the bottom left image.

3.1.2) Adaptive optics correction of live turbulence

Once the Plenoptic Sensor and its wavefront reconstruction algorithms had been validated for static wavefront distortions, the next step was to perform wavefront correction through live atmospheric turbulence. A challenge with adaptive optics in live atmospheric turbulence arises from the rapid speed of correction required to make the wavefront correction before the turbulence conditions change. As mentioned earlier, Taylor's Frozen Turbulence Hypothesis dictates that depending on the wind speed, turbulence is stationary on timescales that can be less under 1 ms [3]. This means that closed loop wavefront reconstruction must occur faster than 100 hertz. The closed loop correction speed increases further if the wavefront reconstruction algorithm does not perform a perfect wavefront reconstruction on the first attempt. As a general rule of thumb, the faster the closed loop wavefront reconstruction, the better the adaptive optics system will perform.

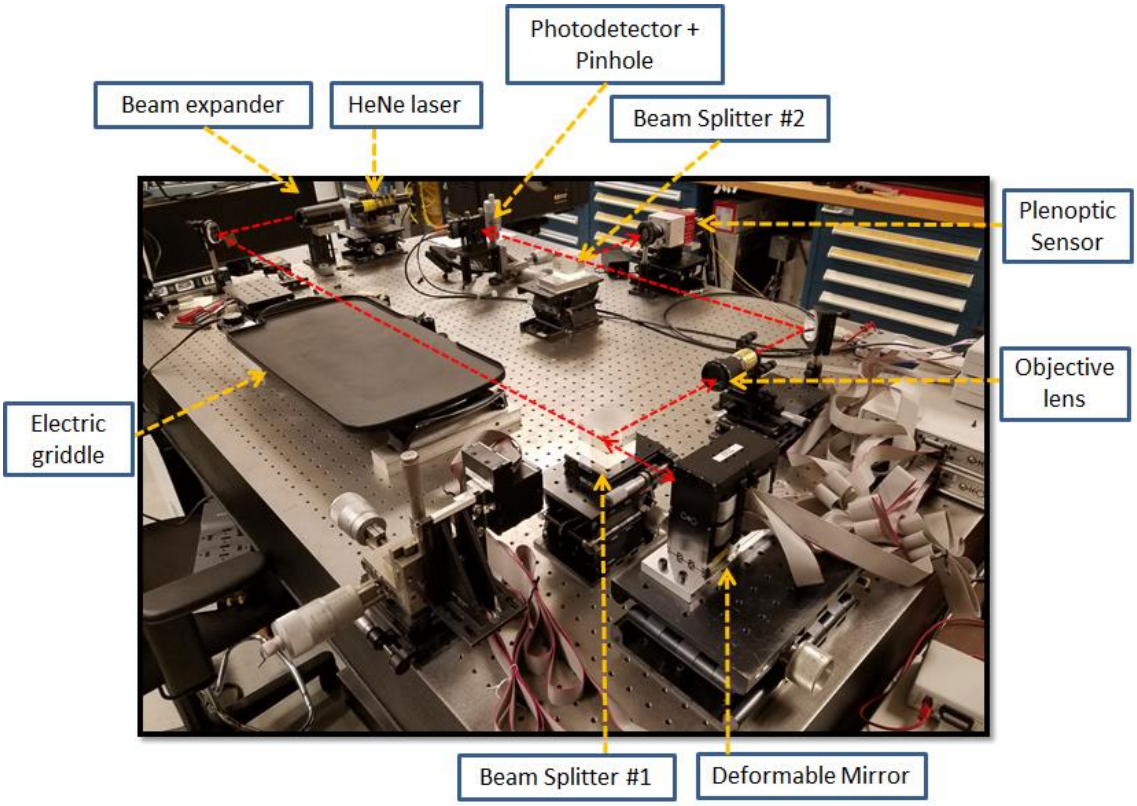

Figure 3.1.8: Experimental layout for real-time AO correction.

Figure 3.1.8 is a picture of our experimental layout used for real-time adaptive optics experiments. The beam originates from the 633 nm HeNe laser in the top left corner of Figure 3.1.8 and passes through the beam expander directly after it. The beam passes roughly 70 mm above a 60 mm long electric griddle which can adjust between 200-450 F and generates the atmospheric turbulence in the propagation channel. The beam then passes through Beam Splitter #1 and is incident on the deformable mirror. The beam reflects off the deformable mirror, re-enters Beam Splitter #1, and then enters the Plenoptic Sensor's objective lens. Beam splitter #2 is located behind the objective lens. Half of the beam is split towards the MLA and the image sensor of the Plenoptic Sensor. The MLA used is an Edmund Optics #64-483

which is 10x10 mm in size, 500 μm in pitch, and 46.7 mm in focal length. The image sensor is an AVT Bonito CL400 Camera Link Camera that is operated at 400 fps with a resolution of 1726x1726 and pixel size of 7x7 μm. The other half of the beam is directed towards a ThorLabs PDA100A photodetector which is used to take power-in-the-bucket (PIB) intensity measurements. Just in front of the photodetector, and at a location coinciding with the back focal plane of the objective lens of the Plenoptic Sensor, a 100 μm pinhole aperture is used as a spatial filter in order to ensure that the photodetector measurements represent a metric of beam quality.

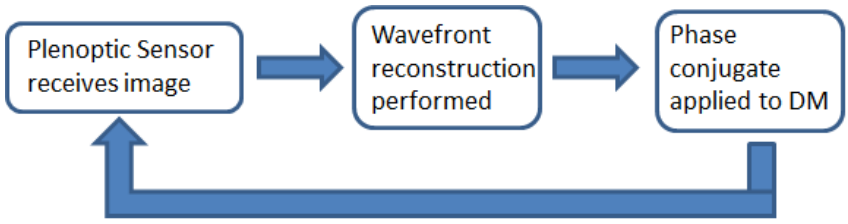

Figure 3.1.9: Adaptive optics flowchart showing 1 cycle of the closed-loop correction.

Figure 3.1.9 is a basic flowchart detailing the procedures of our adaptive optics system. First, the Plenoptic Sensor receives an image of current beam. This Plenoptic image is relayed to our Windows PC for wavefront reconstruction. In order to achieve speeds capable of correcting for real-time atmospheric turbulence, the graph reconstruction algorithm from Section 2.2.2 was chosen to reconstruct the wavefront. After the wavefront is reconstructed, the phase conjugate is applied to the deformable mirror in order to correct for the measured wavefront distortion. A C++ program was written to integrate the Plenoptic Sensor camera hardware and the

deformable mirror hardware. In general, the program acquires the image frame, performs the graph reconstruction algorithm on the image, and then sends a command to the deformable mirror through the USB DAC. Our Windows PC using an Intel i7-4930k CPU is able to perform a closed-loop AO correction (from image acquisition to the DM command) at roughly 250 frames per second.

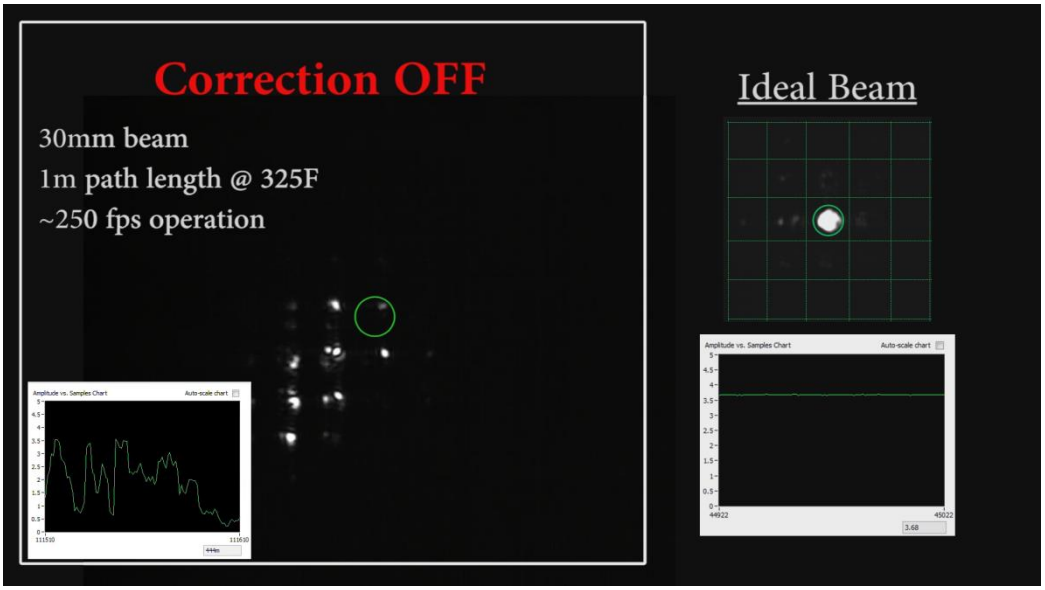

Figure 3.1.10: Closed loop adaptive optics turned off.

The right side of Figure 3.1.10 is a reference for a Plenoptic image of an undistorted beam and its corresponding photodetector readout. As expected, the beam is largely confined to a single MLA sub-aperture. In addition, the photodetector readout shows a constant high voltage reading of roughly 3.7 V. Due to the pinhole aperture acting as a spatial filter, a maximum voltage of roughly 3.7 V is only possible when the beam is mostly undistorted.

The left side of Figure 3.1.10 shows a Plenoptic image when turbulence is being generated and the adaptive optics system is turned off. The green circle represents the area in which the center MLA sub-aperture is located. When the electric griddle is set to 325 F and the generated atmospheric turbulence is strong, the distorted Plenoptic image on the left side of Figure 3.1.10 looks nothing like the reference Plenoptic image on the right. There is almost zero intensity inside the center MLA sub-aperture and instead the intensity is distributed into surrounding sub-apertures. Correspondingly, the photodetector readout on the left side of Figure 3.1.10 shows a very low voltage reading indicating that only a small portion of the beam is able to pass through the pinhole aperture to the photodetector.

Figure 3.1.11: Closed loop adaptive optics turned on.

The right side of Figure 3.1.11 remains as the reference images described previously for a Plenoptic image of an undistorted beam and its corresponding

photodetector readout. The left side of Figure 3.1.11 shows a Plenoptic image when the adaptive optics system is turned on. A strong level of atmospheric turbulence is kept constant between Figure 3.1.10 and Figure 3.1.11. However, it is easy to see that the intensity from the beam is now largely confined to the center MLA sub-aperture (as indicated by the green circle). This suggests that a majority of the beam has been phase corrected despite passing through strong levels of atmospheric turbulence. In addition, the photodetector readout in Figure 3.1.11 shows a higher voltage reading than when compared to the reading shown in Figure 3.1.10. This is visual confirmation that the closed-loop adaptive optics system is successfully able to help compensate for the wavefront distortions generated by atmospheric turbulence.

In order to analyze the effectiveness of the system more thoroughly, the closed-loop adaptive optics system was toggled on and off periodically for constant levels of turbulence and the PIB readings were logged. If the AO system is working correctly, there should be a noticeable increase in the PIB readings when the AO system is on compared to when the AO system is off. The results are presented below in Figures 3.1.12-3.1.14.

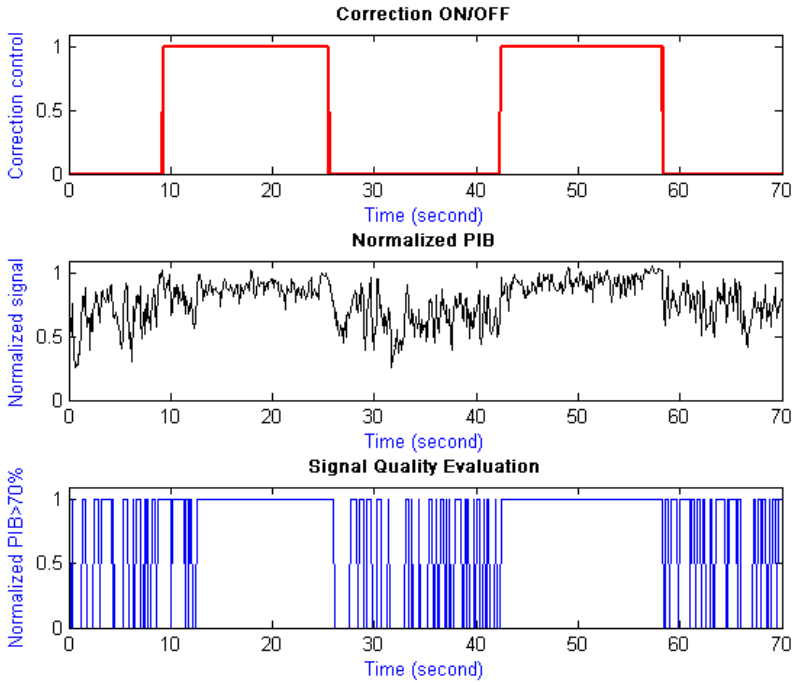

Figure 3.1.12: Adaptive optics system operating under 175 F conditions.

In Figure 3.1.12, the electric griddle is set to 175 F and the closed-loop AO system is turned on and off for two periods totaling roughly 70 seconds. In the top graph of Figure 3.1.12, the on and off AO correction signal is plotted, where a value of "1" indicates that the AO system is turned on, while a value of "0" indicates that the AO system is turned off. The middle graph is a normalized PIB reading which reflects the percentage of intensity that manages to pass through the pinhole relative to the maximum intensity possible in the absence of turbulence. The time scale (in seconds) is identical to the top graph. The bottom graph is a measure of "signal quality", where a value of "1" indicates that the normalized PIB reading is above a threshold value of 70%, while a value of "0" indicates that the normalized PIB reading is below 70%. The time scale (in seconds) is also identical to the top graph.

When looking at the three graphs in Figure 3.1.12, it is easy to see that the mean normalized PIB reading is much higher when the AO system is turned on. In addition, the bottom graph in Figure 3.1.12 shows that when the AO system is turned on, it is able to maintain a consistent normalized PIB reading of >70%. If an optical communication system uses an On-Off Keying modulation scheme with an intensity threshold of 70%, the bottom graph in Figure 3.1.12 suggests that the AO system is successfully able to maintain an accurately modulated signal through turbulence generated with the 175 F electric griddle. The PIB data is analyzed in more detail later in this section.

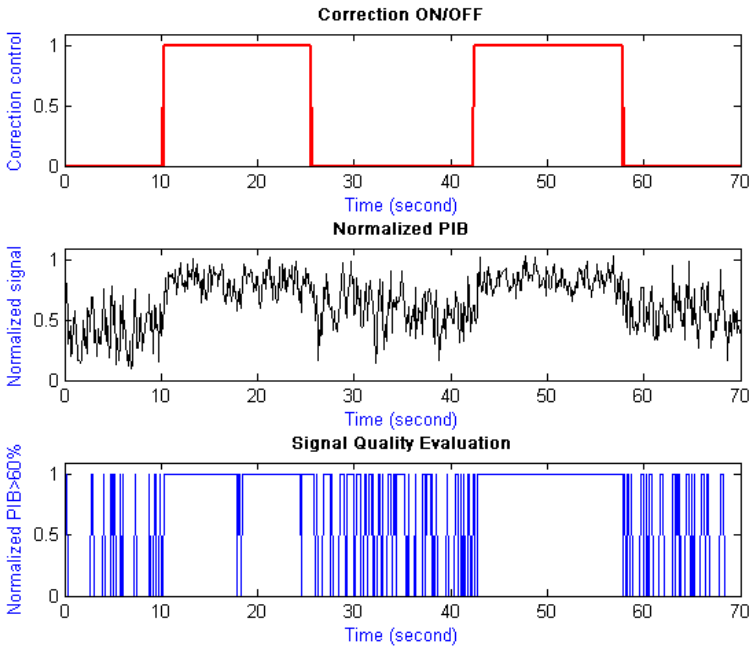

Figure 3.1.13: Adaptive optics system operating under 250 F conditions.

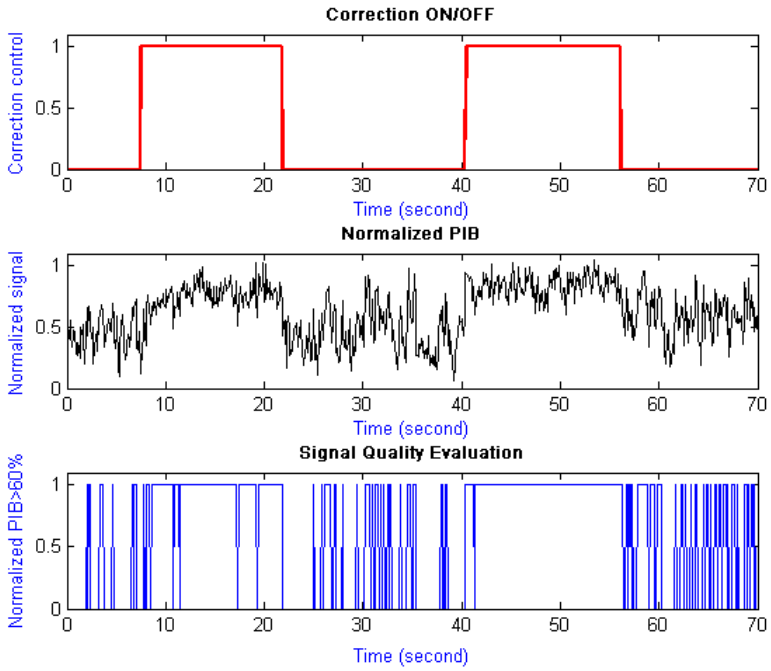

Figure 3.1.14: Adaptive optics system operating under 325 F conditions.

Figure 3.1.13 and Figure 3.1.14 are two additional scenarios with graphs identical to Figure 3.1.12. However, the temperature of the electric griddle has been increased to 250 F in Figure 3.1.13 and 325 F in Figure 3.1.14, which means the turbulence strength has been increased. In addition, the normalized PIB threshold value in the bottom graph of both Figures 3.1.13 and 3.1.14 has been reduced to 60%. By observing the normalized PIB graphs (the middle graphs) in Figures 3.1.13 and 3.1.14, it is easy to see that the normalized PIB values are of lower mean value and higher variance compared to the weaker 175 F turbulence cases of Figure 3.1.12. In addition, although the AO system is able to maintain a normalized PIB threshold of greater than 60% for a majority of the time the AO system is turned on, it is clear that the stronger turbulence presents a tougher scenario for wavefront correction.

Temperature	C_n^2 value	Adaptive Optics (On/Off)	Average value of Normalized PIB	Variance of Normalized PIB	% of time above threshold
175 F	7.38×10^{-7}	OFF	0.674	0.0184	69.8%
175 F	1.38×10^{-7}	ON	0.854	0.0057	98.9%
250 F	1.49×10^{-6}	OFF	0.514	0.0210	29.8%
250 F	3.74×10^{-7}	ON	0.754	0.0100	94.5%
325 F	1.68×10^{-6}	OFF	0.459	0.0207	17.0%
325 F	4.33×10^{-7}	ON	0.703	0.0116	84.3%

Table 3.3: Statistics of adaptive optics operation.

Table 3.3 takes a closer look at the experiments performed in Figure 3.1.12, Figure 3.1.13, and Figure 3.1.14 by calculating relevant statistics. For each temperature setting used on the electric griddle, photodetector PIB data was collected for about 1 minute with the AO system turned off and about 1 minute with the AO system turned on. In addition, the "threshold" mentioned in the last column of Table 3.3 remains identical to that mentioned in Figure 3.1.12 through Figure 3.1.14, where a 60% PIB threshold is used at 250 F and 325 F and a more stringent 70% PIB threshold is used at 175 F.

For the 325 F case, the average value of the normalized PIB is 0.703 with the AO system on and 0.459 with the AO system off. The variance of the normalized PIB is 0.0116 with the AO system on and 0.0207 with the AO system off. More impressively, the percentage of time the normalized PIB is able to stay above the 60% threshold is 84.3% with the AO system on compared to 17% with the AO system off. This shows that the AO system is effective in compensating for the wavefront distortion generated by the 325 F electric griddle. The 250 F case shows similar normalized variance results and the AO system is able to keep the normalized PIB above the 60% threshold 94.5% of the time versus 29.8% when the AO system is off.

In the 175 F case, with the more stringent normalized PIB threshold of 70%, the performance difference with the AO system on and off is less prominent (98.9% versus 69.8%) due to the lower levels of generated turbulence. However, it is impressive to see in the 175 F case with AO on that the variance of the normalized PIB is roughly half of the variance during the 250 F and 325 F cases (0.0057 vs ~0.01). This is an indicator that the AO-corrected signal has less fluctuations due to the AO system performing a better correction during the weaker turbulence generated at 175 F.

In order to relate this lab generated turbulence channel to a real outdoor environment, an equivalent C_n^2 value for a 2 km path length is computed by equating the Rytov variance σ_R^2 in our 2 m indoor propagation path to that of a 2 km path length. The C_n^2 values generated for the 175 F, 250 F, and 325 F scenarios in Table 3.3 are 7.38×10^{-7}, 1.49×10^{-6}, and 1.68×10^{-6}, respectively. The extrapolated C_n^2 values for an equivalent Rytov variance over a 2 km path versus our 2 m path would be 2.33×10^{-12}, 4.71×10^{-12}, and 5.33×10^{-12} for the 175 F, 250 F, and 325 F cases, respectively. The extrapolated 2 km C_n^2 values are all on the order of 10^{-12} which represents the strong turbulence conditions often seen in outdoor environments.

3.2) Outdoor experimental results

3.2.1) Initial device calibration

3.2.1a) Large Aperture Scintillometer

A Large Aperture Scintillometer (LAS) was created to measure a path averaged C_n^2 value. The LAS design was chosen instead of a laser scintillometer due to our interest in the strong turbulence regime. Laser scintillometers often encounter saturation effects at lower levels of atmospheric turbulence because of the coherence of the laser source. When the normalized intensity variance becomes saturated, so does the calculated C_n^2 value. In addition, LED scintillometers with a smaller aperture also encounter these saturation effects over long path lengths or under strong atmospheric turbulence. The aperture averaging effect of an LED LAS satisfies our requirement of effective operation in strong atmospheric turbulence.

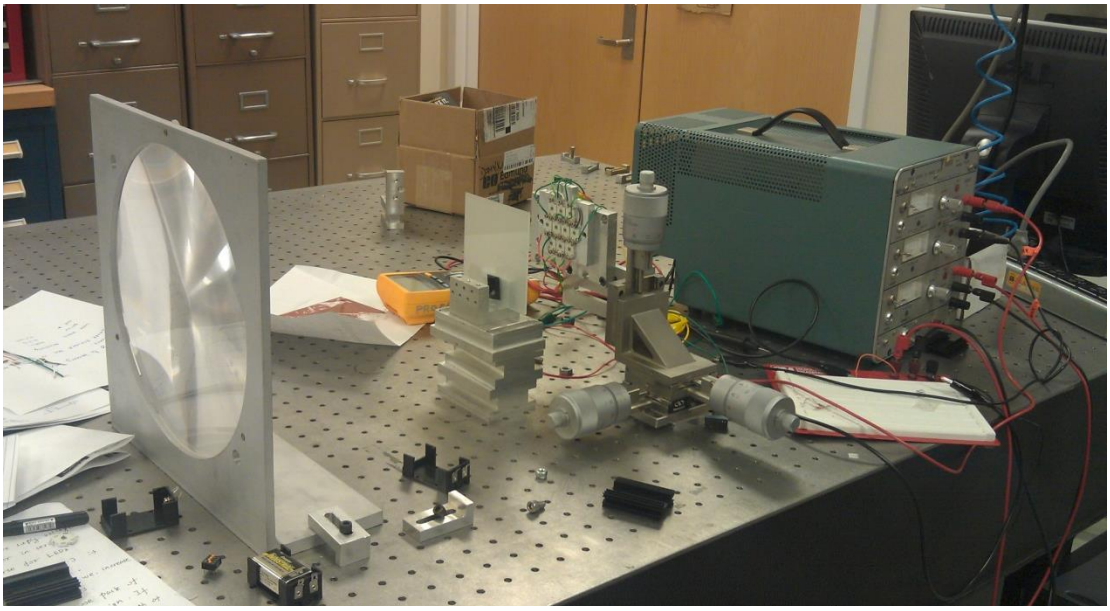

Figure 3.2.1: LAS Transmitter undergoing testing.

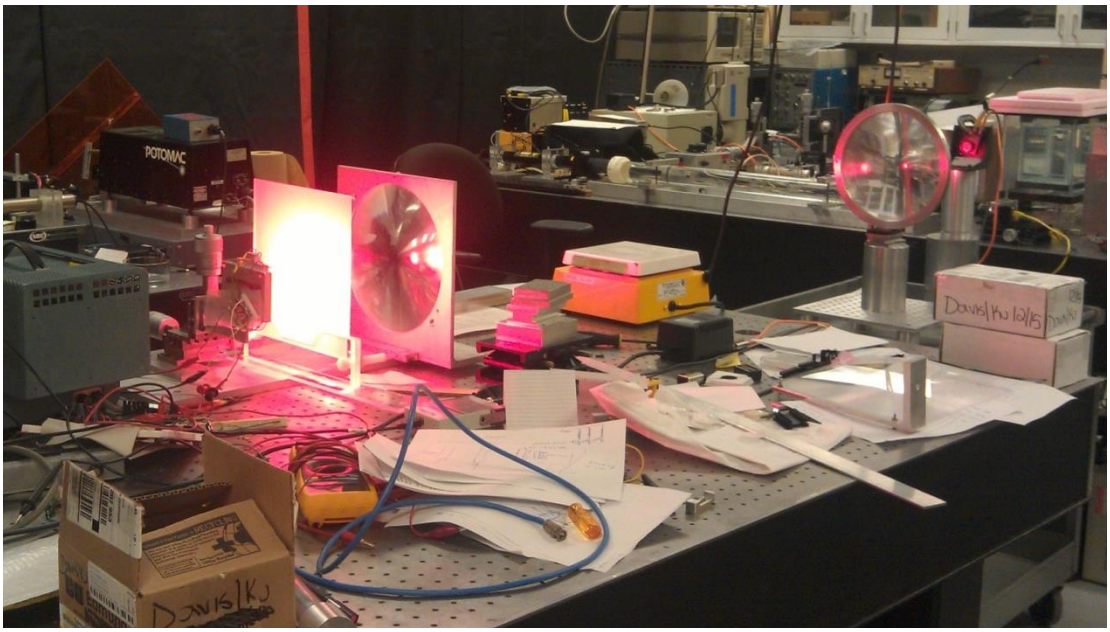

Figure 3.2.2: LAS Transmitter and Receiver undergoing testing.

The transmitter for the Maryland Optics Group (MOG) LAS was developed using a 10.4 inches Fresnel lens with a focal length of 9 inches. The transmitter has 10 Cree XPE LEDs that produce 46 lumens each and draw roughly 1 watt of power each. An Edmund Optics 100x100 mm 220 Grit Ground Glass Diffuser (NT45-656) was placed in front of the LEDs to ensure an even distribution of light. The LED array was placed at the back focal length of the Fresnel lens to ensure most of the light leaves the transmitter in a collimated beam. In addition, a 555 timer chip modulates the LED signal at roughly 25 Hz. This allows for compensation of any background light (from the sun or other sources) by comparing the signal of solely the background versus the background + LED signal.

The receiver for the MOG LAS also uses a 10.4 inches Fresnel lens with a focal length of 9 inches. A large area PDA100A photodetector is placed at the back

focal length of the Fresnel lens to collect as much of the arriving signal as possible. A National Instruments NI-9223 unit receives voltage data from the amplified photodetector and exports this data through Ethernet to a locally attached laptop. The raw waveform data (from the 25 Hz modulated signal) is saved and processed for the intensity variance and the corresponding C_n^2 value.

In order to ensure that the LAS does not saturate in strong turbulence, the following criteria is obeyed [7]:

$$\frac{D_T+D_R}{2\sqrt{\lambda L}} > (\sigma_T^2)^{3/5} \tag{31}$$

where D_T is the diameter of the transmitting aperture, D_R is the diameter of the receiving aperture, L is the propagation length, and λ is the wavelength used in the transmitter. σ_T^2 is defined as:

$$\sigma_T^2 = 0.124k^{7/6}L^{11/6}C_n^2 \tag{32}$$

where $k = \frac{2\pi}{L}$, L is the propagation length, and C_n^2 is the index of refraction structure parameter. Using an extremely strong turbulence value of $C_n^2 = 10^{-10}$, a path length of 200 meters, an operational wavelength of $\lambda = 630\ nm$, and $D_T = D_R =$ $10.4\ inches\ (0.264\ m)$, Equation (31) becomes $23.519 > 7.70$. This ensures that our LAS will not become saturated in even the strongest of turbulence conditions.

Figure 3.2.3: MOG Large Aperture Scintillometer testing in Kim Building parking lot.

Figure 3.2.4: MOG Large Aperture Scintillometer testing on AV Williams Rooftop.

Initial device testing started on the University of Maryland (UMD) campus. Figure 3.2.3 shows the MOG LAS in the parking lot (which no longer exists) behind

the Kim Engineering Building. Figure 3.2.4 shows the MOG LAS on the AV Williams rooftop. The purpose of these tests was to verify that the C_n^2 readings made sense in accordance with the general variations expected during the diurnal cycle.

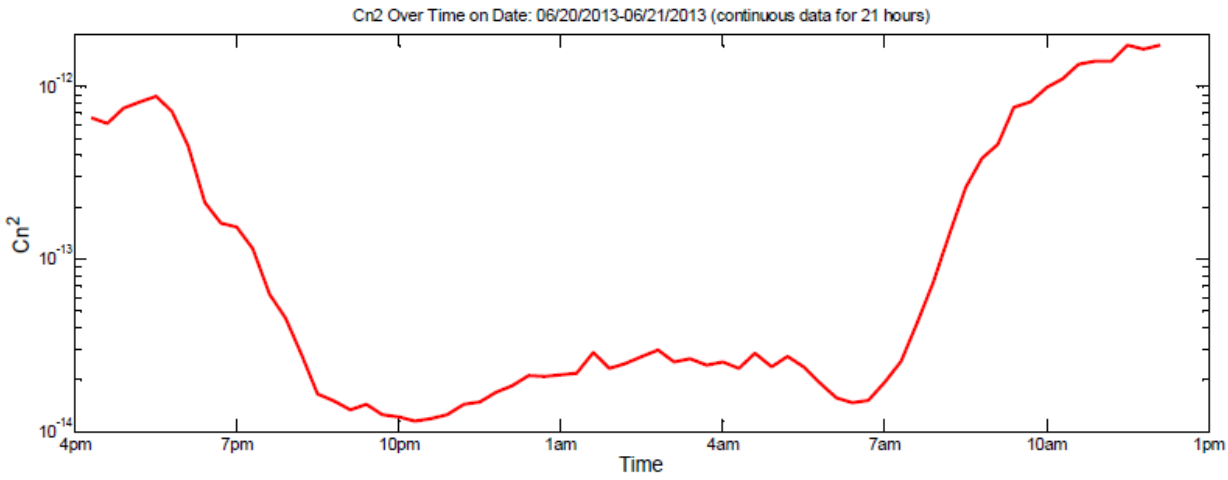

Figure 3.2.5: Large Aperture Scintillometer data on AV Williams on rooftop.

Figure 3.2.5 is a 21 hour long data logging session testing the MOG LAS on top of the AV Williams building on the UMD campus. The data collected in this experiment shows an accurate depiction of the C_n^2 diurnal cycle. Starting around 5pm, the sun begins to set and the ground temperature starts to cool. This causes a decrease in the temperature gradient between the ground and the atmosphere which results in decreasing C_n^2 values. Once the sun has set, the C_n^2 changes are small because the ground and atmosphere achieve a state close to thermal equilibrium. However, starting around 7 am, the rising sun begins to heat the ground again which leads to an increase in the ground to atmosphere thermal gradient and thus a rise in the C_n^2 value. This continues throughout the day until the evening approaches and the diurnal cycle

repeats. The initial data from the MOG LAS in Figure 3.2.5 correctly matches the expected C_n^2 diurnal cycle and was a good step towards verifying the MOG LAS.

Figure 3.2.6: MOG Large Aperture Scintillometer testing at the US Naval Academy.

The next step of testing for the MOG LAS was conducted at the US Naval Academy. In co-operation with Professor Svetlana Avramov-Zamurovic, the MOG LAS was tested alongside the US Naval Academy's Kipp and Zonen MkII commercial LAS which operates at 850 nm. The data is presented below:

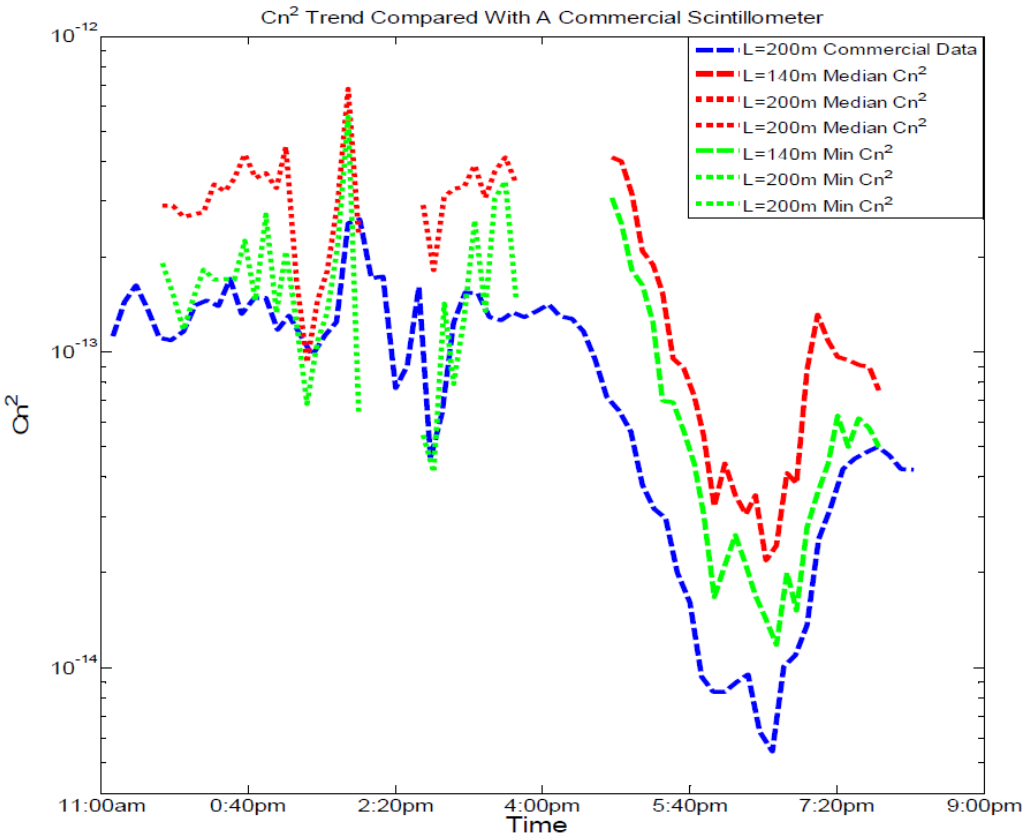

Figure 3.2.7: Comparison of MOG LAS with a Kipp and Zonen LAS.

Figure 3.2.7 shows a 9 hour side-by-side test of the MOG LAS and the Kipp and Zonen LAS. The MOG LAS was operated with a path length of 200 m until around 4:00 pm. Starting around 5:00 pm, a shorter path length of 140 m was used until the tests were concluded at 8:00 pm. The Kipp and Zonen LAS remained at a constant 200 m path length. The blue curve represents the C_n^2 value calculated by the Kipp and Zonen LAS while the green and red curves represent the median and minimum C_n^2 calculated by the MOG LAS. The two devices show strong agreement with each other which was a very promising sign for the MOG LAS. Also, the diurnal dip around 6-7 pm, caused by the equilibrium of the ground and air temperature, is clearly visible in both instruments. The slight difference in C_n^2 readings between the

two devices is normal as the two instruments are not seeing the exact same turbulence channel. The C_n^2 differences are well under an order of magnitude difference, and most importantly, the agreement in the general C_n^2 trend is clearly visible.

3.2.1b) RTD Probe System

An RTD C_T^2 device was also developed to calculate C_n^2 through C_T^2 measurements. The prototype device is pictured below:

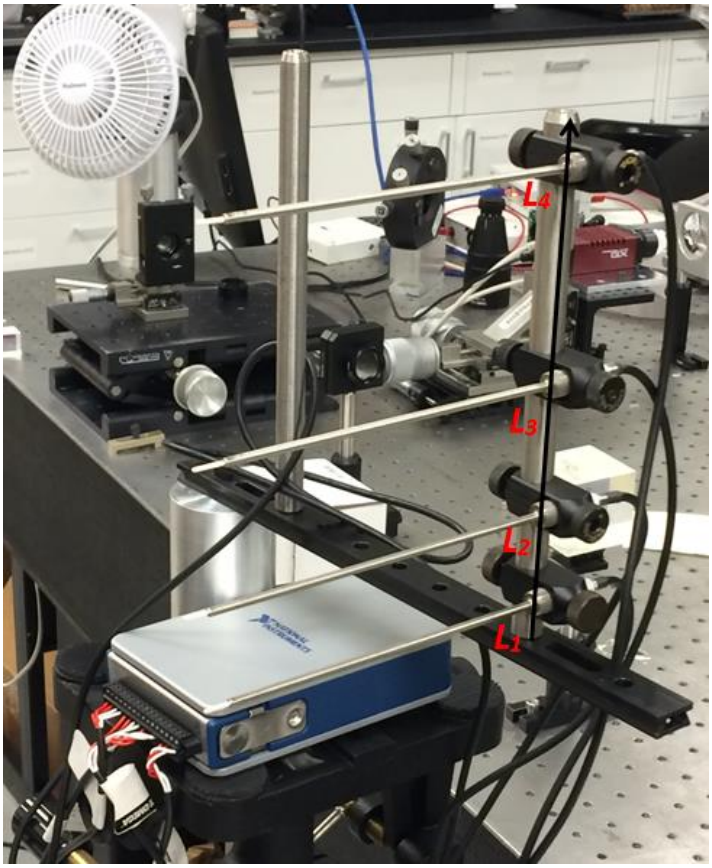

Figure 3.2.8: Prototype RTD probe system for C_T^2 measurements.

Initial testing of the RTD C_T^2 device used an NIDAQ unit with Omega P-L-1/10-1/8-6-1/8-T-3 RTD probes which have a precision up to 0.03 °C. Verification of

the RTD C_T^2 device involves calibration for the variations in probe sensitivity and observing the 2/3 power law that is described by Equation (33). Also, the RTD probes are spaced out anywhere from R≈1-50 cm to satisfy the spacing criteria from Equation (33).

$$D_T(R) = C_T^2 R^{2/3}, \qquad l_0 \ll R \ll L_0 \tag{33}$$

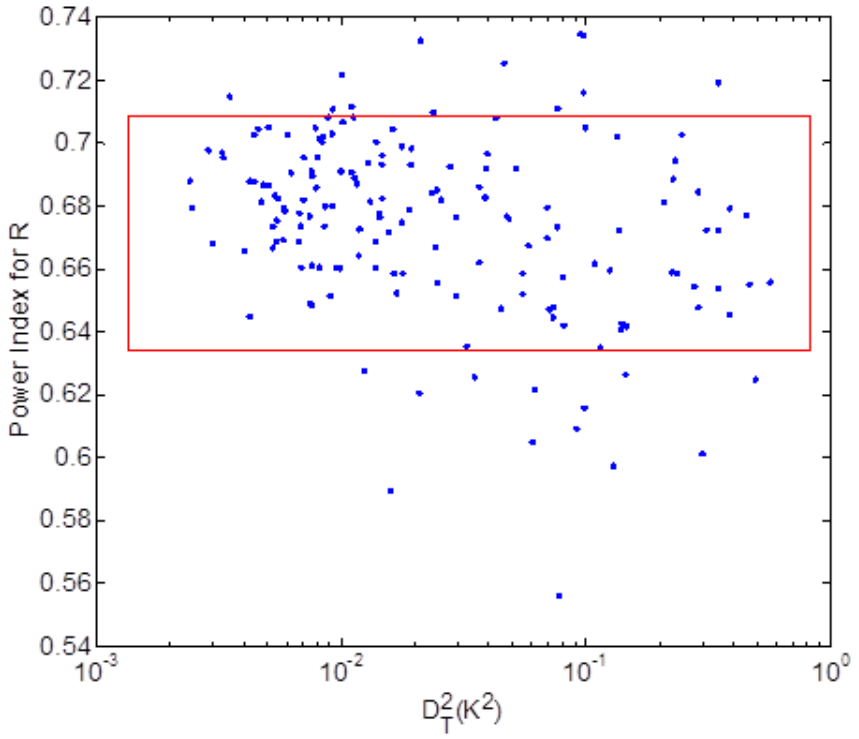

Figure 3.2.9: 2/3 Power Law of R for C_T^2.

Figure 3.2.9 is initial lab testing of our RTD C_T^2 device. An artificial turbulence generator, often a hot plate or electric griddle, is set up below the RTD C_T^2 device. The turbulence is varied over a wide range of C_n^2 values in order to examine if the $R^{2/3}$ law is satisfied between the 4 RTD probes. After plotting the power spectrum of the collected data points, it is clear that the data collected is in agreement with the $R^{2/3}$ law because a majority of the measurements are in the boxed area (red

box in Figure 3.2.9) around 0.666 on the Y-axis which represents the power index of *R*. During the same lab testing, the variance and mean temperature measurement of each probe is recorded over a long period of time in order to calibrate out any manufacturing differences between the RTD probes.

An outdoor weatherized version of the RTD C_T^2 device was constructed that could be used to compare the derived C_n^2 values to the C_n^2 values calculated by a scintillometer in varied weather conditions. The device would be operated over a long time period in order to observe the diurnal fluctuations of C_n^2 and to observe if there is general agreement with an adjacent scintillometer.

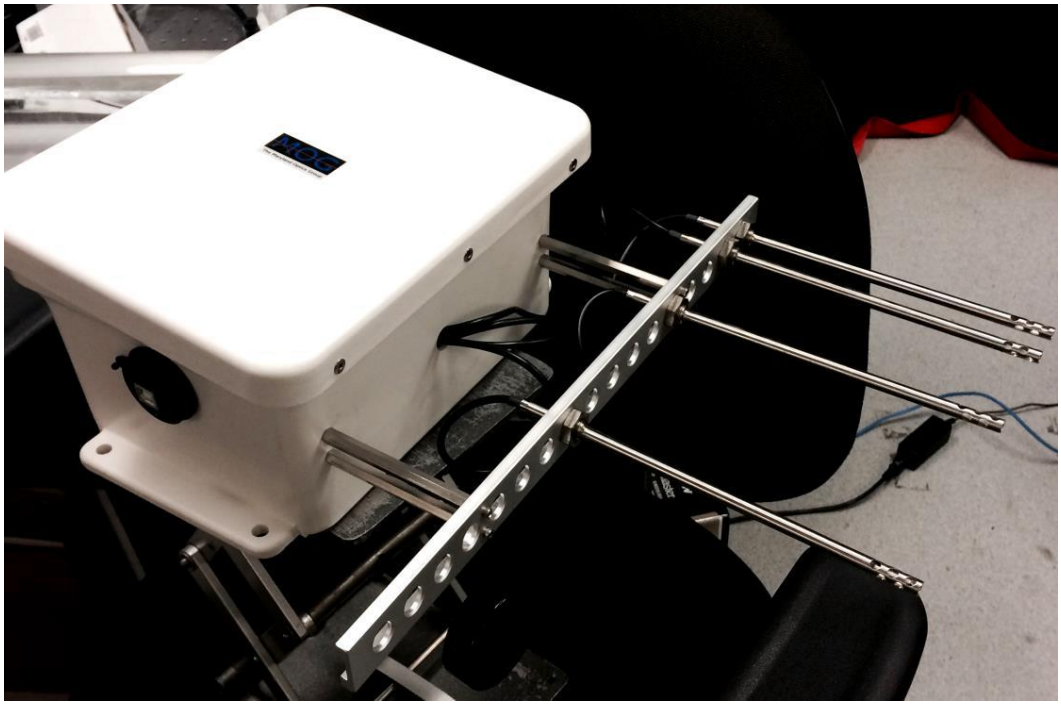

Figure 3.2.10: Weatherized RTD C_T^2 device.

The weatherized outdoor RTD C_T^2 device is shown in Figure 3.2.10. Inside the weatherproof housing there is an Omega 4 channel temperature data logger (OM-CP-QUADRTD) which is connected to the external Omega P-L-1/10-1/8-6-1/8-T-3 RTD probes. The distances between the RTD probes are fixed while satisfying the criteria $l_0 \ll R \ll L_0$. The data logger is able to store 12 hours of data when sampling once every two seconds. The sampling rate can be decreased further when access to the physical device is limited.

The weatherized outdoor RTD C_T^2 and the Prototype RTD C_T^2 device were field tested at the University of Central Florida (UCF) Townes Institute Science and Technology Experimentation Facility (TISTEF). TISTEF has a 1 km outdoor test range and is equipped with Scintec SLS20 and Scintec BLS900 scintillometers. The TISTEF range has ideal conditions for a well instrumented comparison in a real world environment between the two Scintec commercial scintillometers and our RTD C_T^2 systems. The BLS900 is operated over the full 1 km test range while the SLS20 is operated over a shorter 200 m path. RTD Device #1 (the Prototype RTD C_T^2 device) is placed close to the SLS20 while RTD Device #2 (the weatherproof RTD C_T^2 device) is placed next to the BLS900 transmitter at the far end of the test range. The experimental layout is shown below in Figure 3.2.11a.

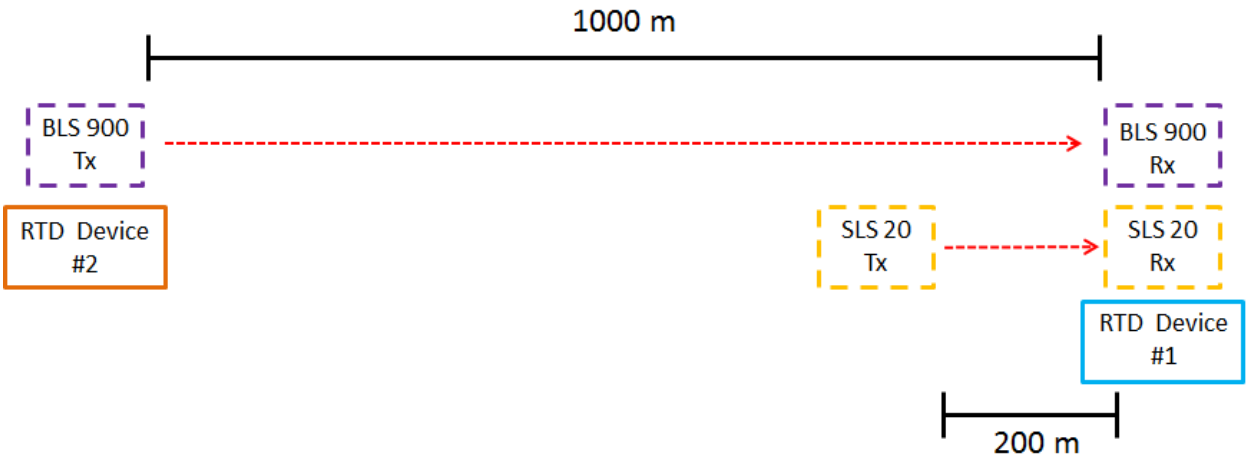

Figure 3.2.11a: Outdoor verification of RTD C_T^2 devices.

Figure 3.2.11b: BLS900 Transmitter and RTD Device #2.

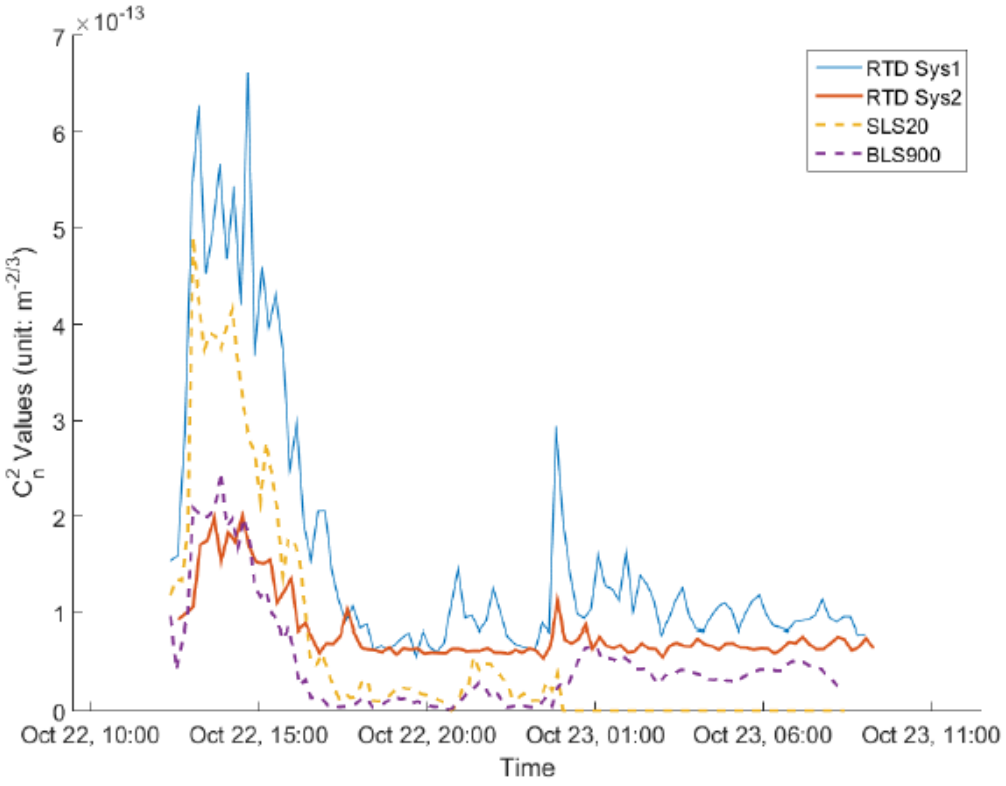

Figure 3.2.12: C_n^2 values from Scintec Scintillometers and RTD C_T^2 devices.

Figure 3.2.12 shows data collected from roughly 12 pm on October 22 to around 8 am on October 23. Several interesting points can be observed from the plotted data. One, it is clear that all 4 devices are in general agreement with respect to the expected diurnal C_n^2 trends. All 4 devices show maximum values in the afternoon when the atmospheric turbulence is expected to be the strongest. All 4 devices also show periods of low turbulence after sunset and throughout the night. It should be noted that the SLS20 turned off around midnight which explains the flat zero readings after 00:00 am October 23. Another interesting point is that the devices show that the level of atmospheric turbulence is not uniform throughout the 1 km channel. RTD Device #2 and the BLS900 transmitter were located close together (as shown in

Figure 3.2.9), and their C_n^2 values in the afternoon (strong turbulence conditions) are in good agreement with each other. In comparison, RTD Device #1 and the SLS20 were located closer together (as shown in Figure 3.2.11a) and show similar C_n^2 values during the afternoon, but the C_n^2 values are noticeably larger than those calculated by RTD Device #2 and the BLS900. This implies that on October 22, the atmospheric turbulence was weaker at the far side of the range (near the BLS900 transmitter and RTD Device #2) in comparison to the near side of the range (near the SLS20 and RTD Device #1). Another final note is that the RTD Devices are not as accurate as the scintillometers in low turbulence conditions where the C_n^2 values are around 10^{-14}. This is because the resolution of the Omega P-L-1/10-1/8-6-1/8-T-3 RTD probe is not good enough to detect very small temperature fluctuations. Given a temperature resolution of T_{res} = 0.01 Celsius, a maximum probe spacing of R=20 cm, an approximate temperature of T≈300 K, and an approximate pressure of P≈*1000 mbar*, an estimate for the minimum measurable C_n^2 value can be determined using Equations 35 and 36:

$$D_T(R) = C_T^2 R^{2/3} \tag{34}$$

$$\min(C_T^2) = \frac{T_{res}}{R^{\frac{2}{3}}} \tag{35}$$

$$\min(C_n^2) = \min(C_T^2)\left[(79 \times 10^{-6})\frac{P}{T^2}\right]^2 \approx 2 \times 10^{-14} \tag{36}$$

The estimated $\min(C_n^2)$ value explains why the C_n^2 values in Figure 3.2.12 seem to never go below 10^{-14}. A higher resolution RTD probe would be required to measure C_n^2 values accurately in low turbulence conditions. On the other hand, the

RTD C_T^2 devices are a great tool for measuring C_n^2 values in very strong atmospheric turbulence where traditional scintillometers may saturate due to strong optical scintillation effects. The temperature fluctuations should not be affected by any upper bound saturation and should continue to function in very strong atmospheric turbulence.

3.2.1c) Plenoptic Sensor

The Plenoptic Sensor was field tested at the TISTEF range at the Kennedy Space Center. In order to collect as much of the wavefront as possible, the objective lens of the deployed Plenoptic Sensor consisted of a 6 inch Celestron Cassegrain telescope with adjustable focus. The image sensor used was an AVT Prosilica GX1050 camera. The MLA used had a size of 10x10 mm, pitch of 300 μm, and a focal length of 18.8 mm. This is an identical setup to the Plenoptic Sensor used in Section 2.3.5. A collimated 532 nm laser was placed roughly 1 km away from the Plenoptic Sensor. In addition, a Scintec BLS900 scintillometer placed alongside the same 1 km channel was used to log C_n^2 values during data collection with the Plenoptic Sensor.

Figure 3.2.13: Testing the Plenoptic Sensor on the TISTEF range.

Figure 3.2.13 is the experimental setup of the Plenoptic Sensor at the TISTEF range. The Plenoptic Sensor is connected to a laptop and powered by a portable Honda EU2000i gas generator. The laptop is running a custom C++ program to continuously record images at 30 fps. A 15 frame continuous sample of the data collected by the Plenoptic Sensor is shown below:

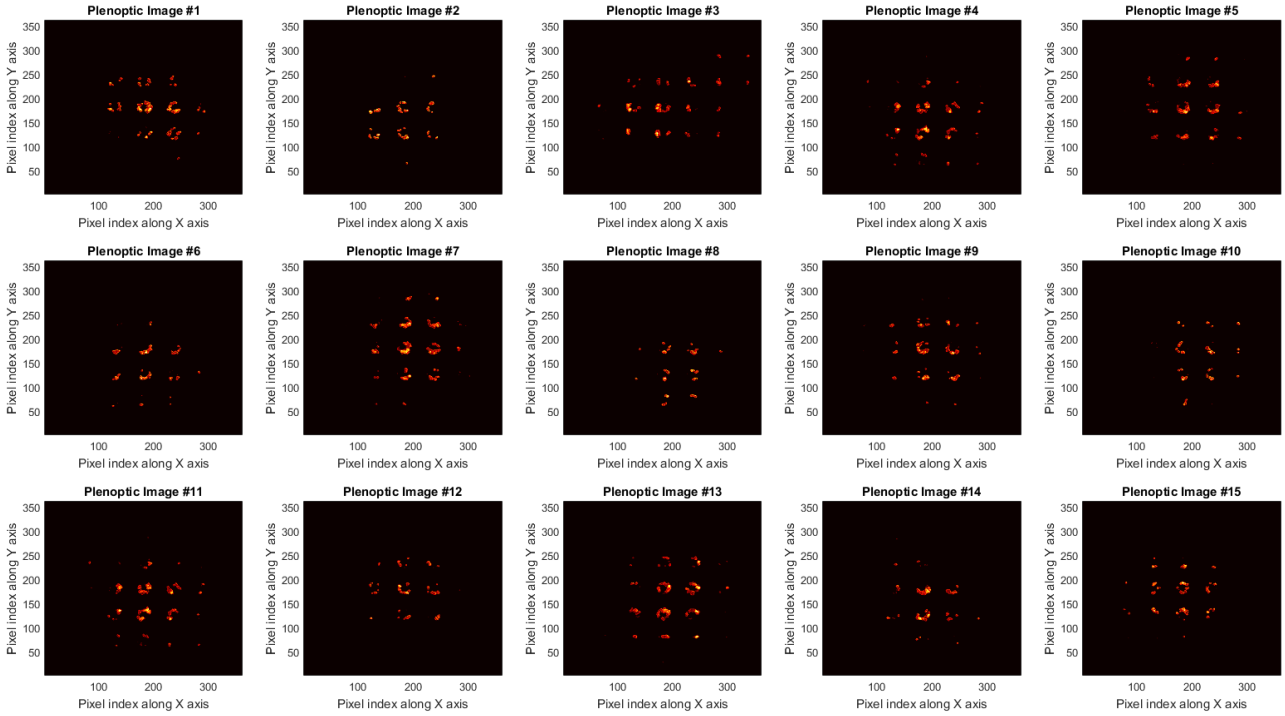

Figure 3.2.14: 15 continuous Plenoptic images.

One simple analysis can be performed with these 15 Plenoptic images by reconstructing the incoming beams' intensity profile. The results are displayed below:

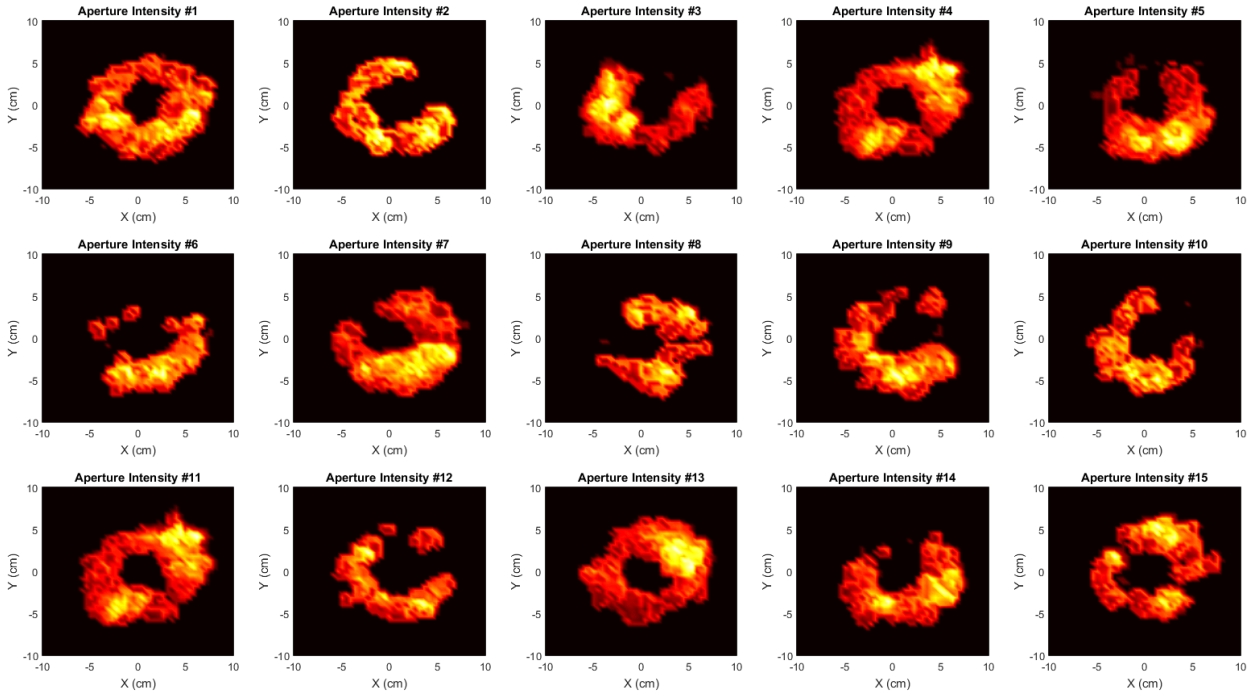

Figure 3.2.15: Beam intensity profile from Plenoptic images in Figure 3.2.14.

In Figure 3.2.15, it is interesting to note that there are several different beam shapes that do not have an intensity pattern resembling the ideal shape of a Cassegrain telescope. Instead, the intensity pattern more closely resembles a Cassegrain telescope shape with multiple large dark areas within the shape. This is an indication of significant beam breakup effects caused by the atmospheric turbulence. The total beam intensity from each image in Figure 3.2.15 can be determined. The result is shown below:

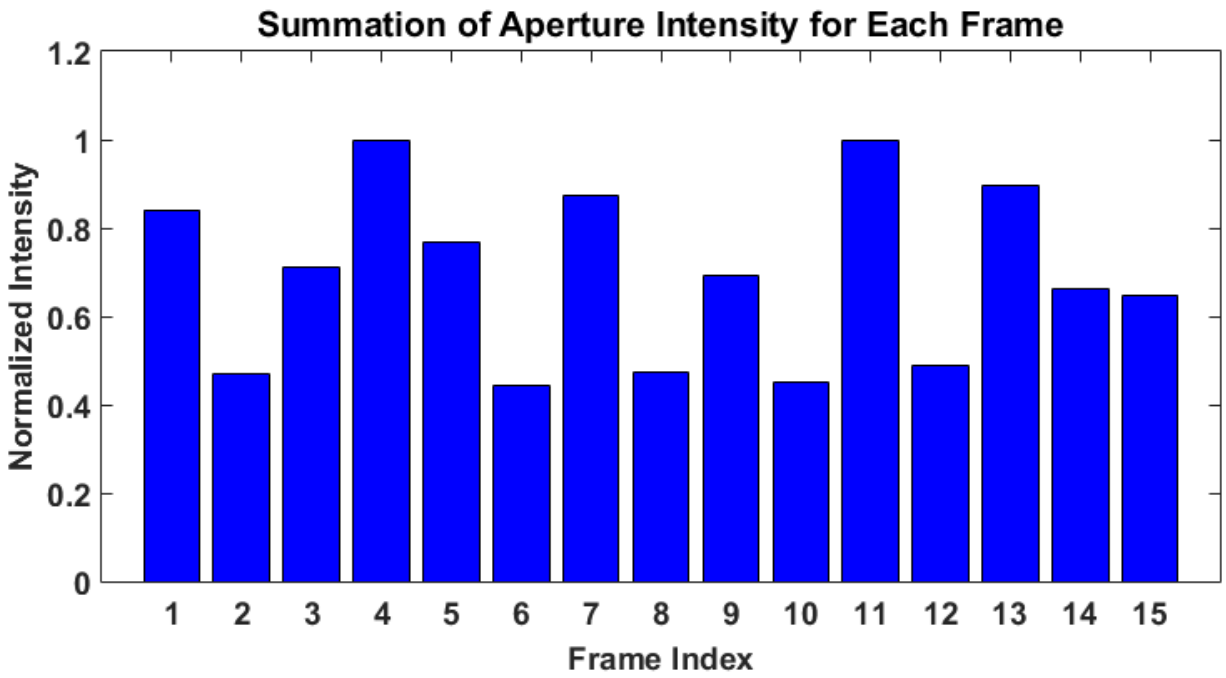

Figure 3.2.16: Normalized beam intensity of each frame from Figure 3.2.15.

Figure 3.2.16 shows the normalized beam intensity for each one of the frames in Figure 3.2.15. As mentioned previously, beam breakup effects are shown by the fluctuations in normalized intensity. Frames 2, 6, 8, 10, and 12 have a normalized intensity near 0.5 which indicates that significant portions of the overall beam are missing and not arriving at the Cassegrain telescope. The data collected by the Plenoptic Sensor can also be used to determine a C_n^2 value. Using the data from Figure 3.2.16 as well as other frames taken during the same minute, a C_n^2 value of $7.2 \times 10^{-13}\ m^{-2/3}$ is calculated. At the same instance of time, the C_n^2 value determined by the adjacent BLS900 scintillometer was $8.4 \times 10^{-13}\ m^{-2/3}$. This shows similarity in C_n^2 value determined by the Plenoptic Sensor and a traditional scintillometer reading.

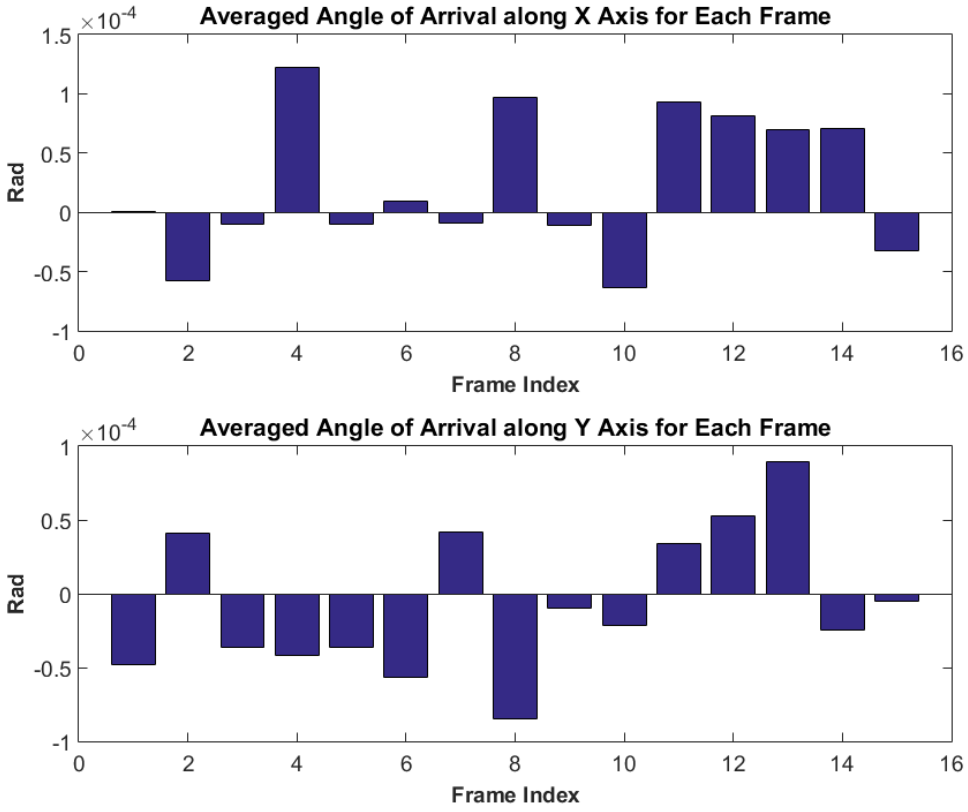

Figure 3.2.17: Angle of arrival data for Plenoptic images obtained in Figure 3.2.14.

Another interesting use of the Plenoptic Sensor is looking at the averaged angle of arrival in the X and Y axis. This can be determined by analyzing the location of the intensity in the Plenoptic images from Figure 3.2.14. After determining the different angle of arrivals, a corresponding C_n^2 value can be determined for the X and Y axis separately. A C_n^2 value of $5.3 \times 10^{-13}\ m^{-2/3}$ is determined for the X component of the incoming wavefront and a C_n^2 value of $7 \times 10^{-13}\ m^{-2/3}$ is determined for the Y component. These numbers generally agree with the reading of $8.4 \times 10^{-13}\ m^{-2/3}$ from the BLS900 scintillometer and also provide a "2-

dimensional" C_n^2 reading that is not possible to obtain from a single-aperture scintillometer.

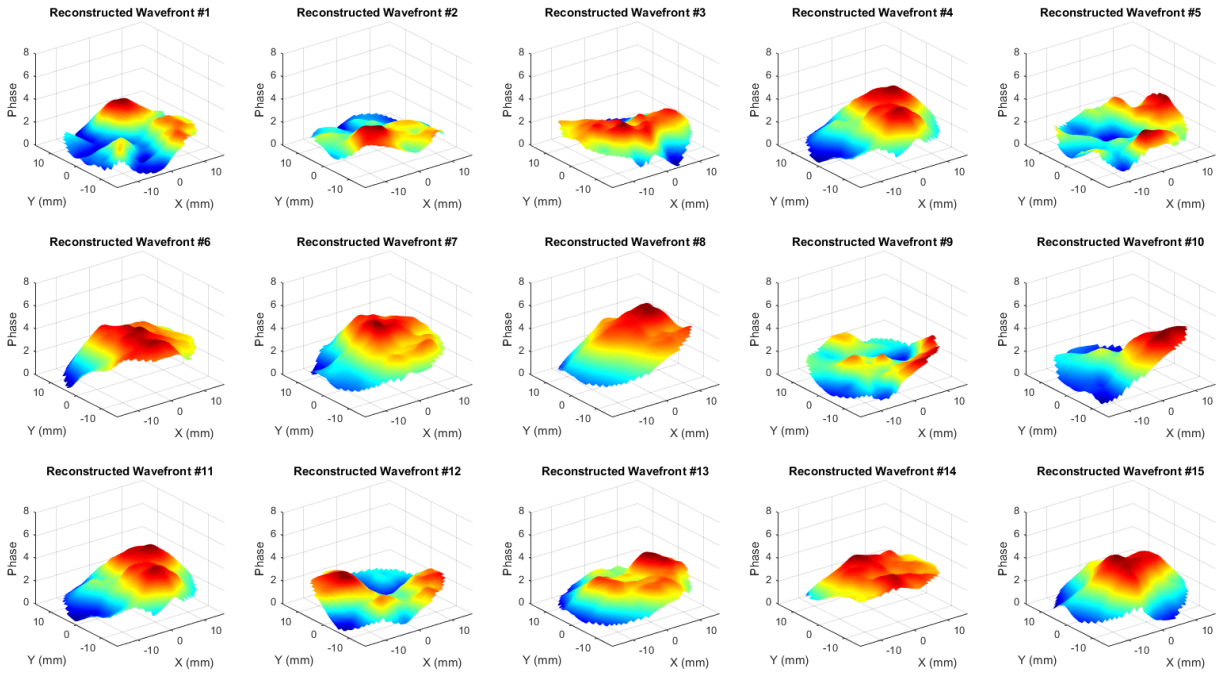

Figure 3.2.18: Wavefront reconstruction from Plenoptic images.

Finally, Figure 3.2.18 shows wavefront reconstructions of the Plenoptic Images from Figure 3.2.14. The checkerboard reconstruction algorithm (from Section 2.2.1) is used to reconstruct the wavefront. An intensity weighted averaging approach is taken when dealing with overlapped patches of light with different phase information (which are previously mentioned in Section 2.3.3) in order to make sense of the complex wavefront situations arising in strong atmospheric turbulence. The initial Plenoptic Sensor field test demonstrates the flexibility of a wavefront sensor

capable of working in strong atmospheric turbulence. Not only can the wavefront be reconstructed, but a corresponding C_n^2 along two transverse dimensions can be calculated to aid in atmospheric characterization.

3.2.1d) Transmissometer

A transmissometer was developed to measure the attenuation coefficient through the atmosphere. Beer's Law is used as the basis for determining the attenuation coefficient:

$$I(x) = I_0 e^{-\alpha x} \tag{37}$$

where x represents a propagation distance in m, I_0 is the initial intensity in $watts/m^2$, $I(x)$ is the measured intensity a distance x from I_0 in $watts/m^2$, and α is attenuation coefficient in m^{-1}. Therefore, with knowledge of I_0, $I(x)$, and x, the attenuation coefficient α can be calculated.

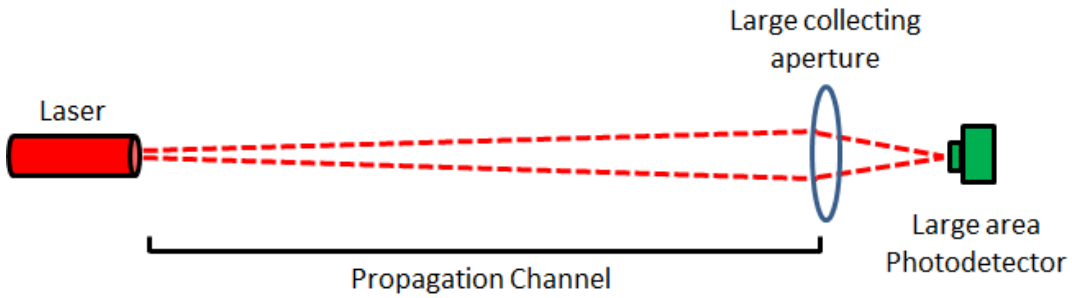

Figure 3.2.19: Basic principle of a transmissometer.

Figure 3.2.19 is a diagram of the prototype transmissometer system. The prototype transmissometer operates under the simple principle of comparing the initial beam intensity I_0 at the transmitter to the beam intensity at the receiver $I(x)$. A laser of known power is emitted at the transmitter side while the receiver end is a

large collection aperture and large area photodetector. The collection aperture must be large enough to accommodate for atmospheric turbulence effects such as beam expansion and beam wander. This ensures that an accurate received power reading is recorded at the receiver despite the presence of mild misalignment and beam expansion effects.

Figure 3.2.20: Transmissometer testing at the Shuttle Landing Facility.

Initial testing of the prototype transmissometer was conducted at the Shuttle Landing Facility (SLF) at the Kennedy Space Center (KSC). A propagation distance of 150 m was used between the collimated 640 nm Coherent fiber laser transmitter and the receiver. The receiver is pictured in Figure 3.2.20 and consists of a Pelican case acting as the waterproof housing that is mounted onto a tripod. The Pelican case has a hole cut out of the lid so that an aspheric Fresnel lens can be embedded into it. The aspheric Fresnel lens with 10.4 inch diameter and 9 inch focal length is used to

collect the incoming beam and focus it onto a large area 9.5 mm Thorlabs power S120C photodiode power sensor.

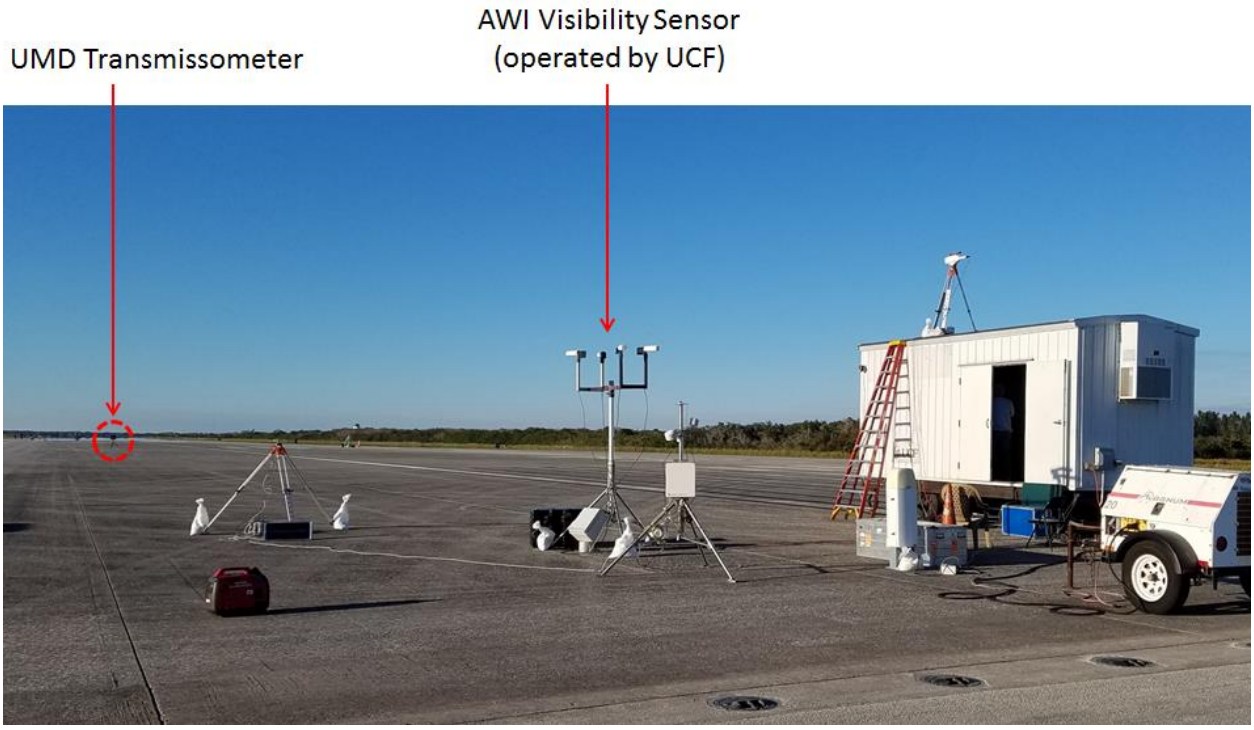

Figure 3.2.21: MOG Transmissometer + AWI Visibility Sensor.

During the transmissometer test, an AWI Visibility Sensor was available near the transmitter side to provide a point of reference for the transmission data. A visibility sensor can convert a visibility reading to the attenuation coefficient through the Koschmieder equation [47].

$$C_v(x) = e^{-\alpha x} \tag{38}$$

where $C_v(x)$ represents the contrast ratio, α is the atmospheric attenuation coefficient in m^{-1}, and x represents the visibility in m. The contrast ratio is based on the minimum observable contrast between a perfectly black object and the horizon sky.

Koschmieder initially determined this contrast ratio to be 0.02 although more recent studies find 0.05 to be a more realistic value for $C_v(x)$ [47]. Using $C_v(x) = 0.05$, the atmospheric attenuation coefficient can be extracted from the visibility data by the following relation [47]:

$$\alpha = \frac{\ln(0.05)}{x} \tag{39}$$

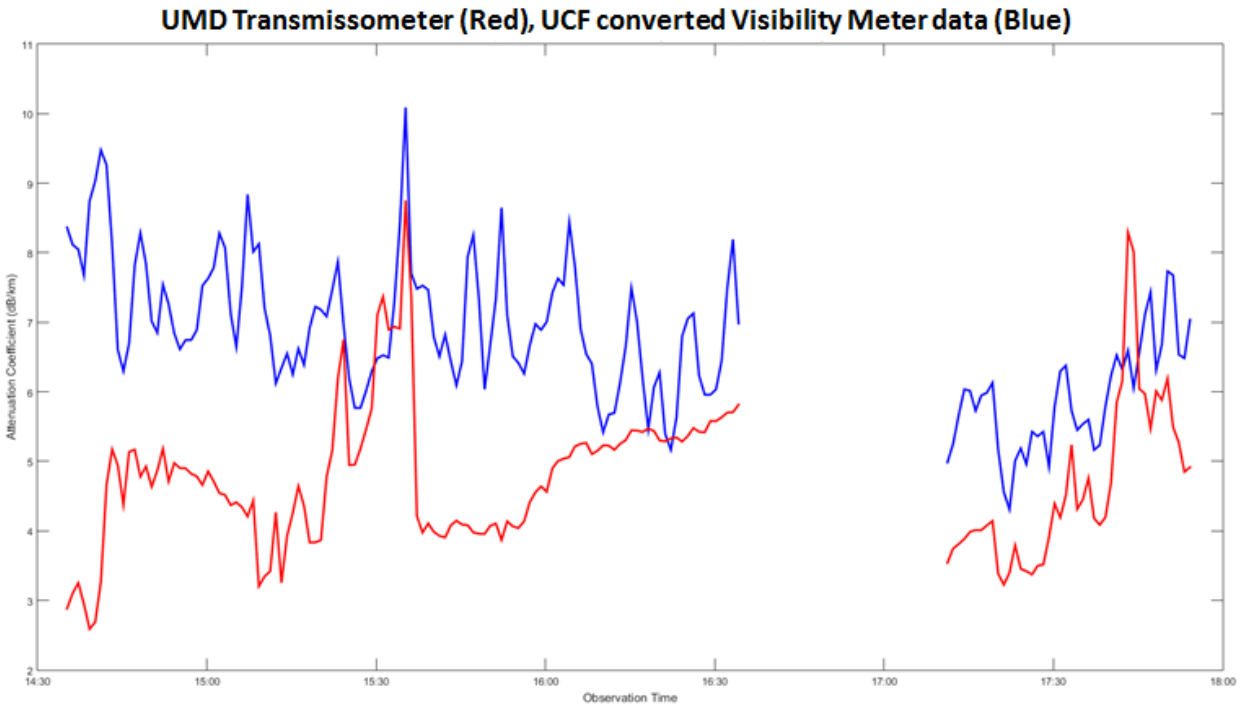

Figure 3.2.22: Atmospheric attenuation coefficient data.

Figure 3.2.20 shows the values of α in *dB/km* for the MOG Transmissometer (red curve) and the AWI Visibility Meter (blue curve). Both devices use optical methods to determine the attenuation coefficients and show values roughly on the same order of magnitude. An interesting point to note is that although these optical methods of determining the attenuation coefficients produced similar values, other methods may not follow suit. Figure 3.2.21 shows visibility data collected by the

AWI Visibility Meter (which reasonably agrees with the MOG Transmissometer) as well as visibility measurements from a hand held sun photometer and two different particle counters. The sun photometer and particle counters show visibility measurements anywhere from 5 to 10 times higher than the AWI Visibility meter. The disagreement in visibility readings is not surprising due to the different data acquisition methodologies but more work needs to be done to determine which values are more realistic.

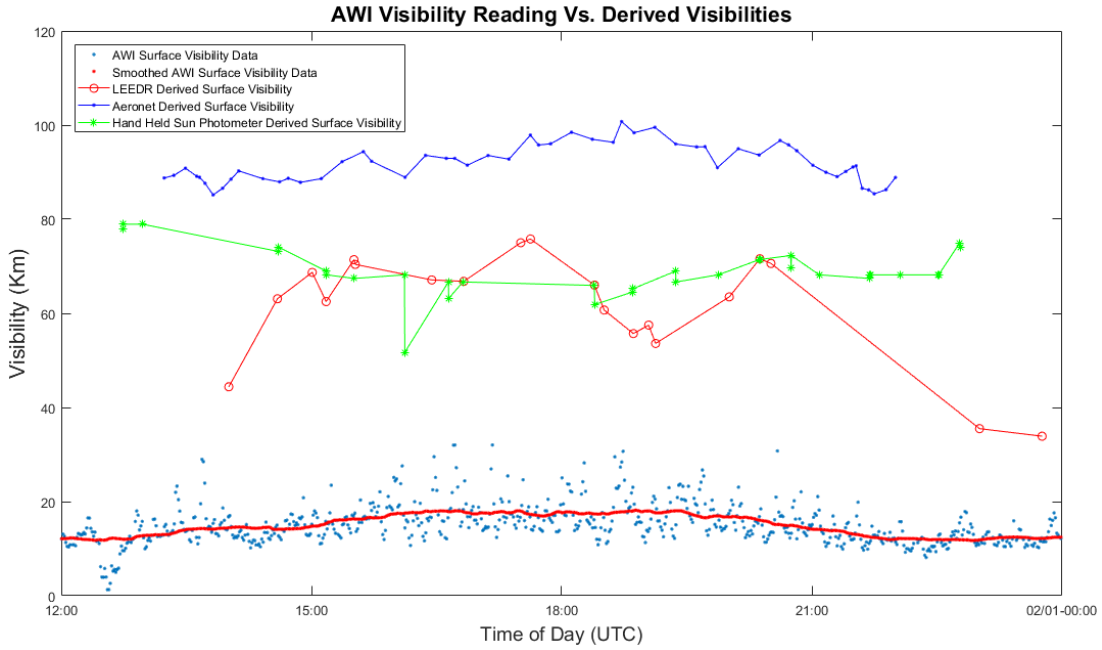

Figure 3.2.21: Visibility readings from visibility sensor, sun photometer, and particle counters.

3.3) Field deployment of MOG equipment

The equipment presented in the previous section has been deployed in well documented field tests. The UMD Maryland Optics Group (MOG) and UCF Wave

Propagation Research Group (WPRG) have been involved in joint atmospheric characterization tests to further the understanding of the atmosphere on optical properties. In addition, the MOG and WPRG have been called upon to provide atmospheric data alongside other organizations that are conducting field testing. The experimental setup from a week long field test in January of 2017 is presented below. The testing was conducted at the KSC SLF from January 30th 2017 to February 3rd 2017.

Figure 3.3.1: MOG LED Large Aperture Scintillometer.

Figure 3.3.1 shows the MOG LED Large Aperture Scintillometer on the KSC SLF. The transmitter and receiver were separated by 100 m. The receiver was located roughly 500 m from the south side of the SLF while the transmitter was located roughly 600 m from the south side of the SLF. A laptop is attached to the receiver for data logging. The transmitter, receiver, and laptop are powered by a Honda EU2000i gasoline generator.

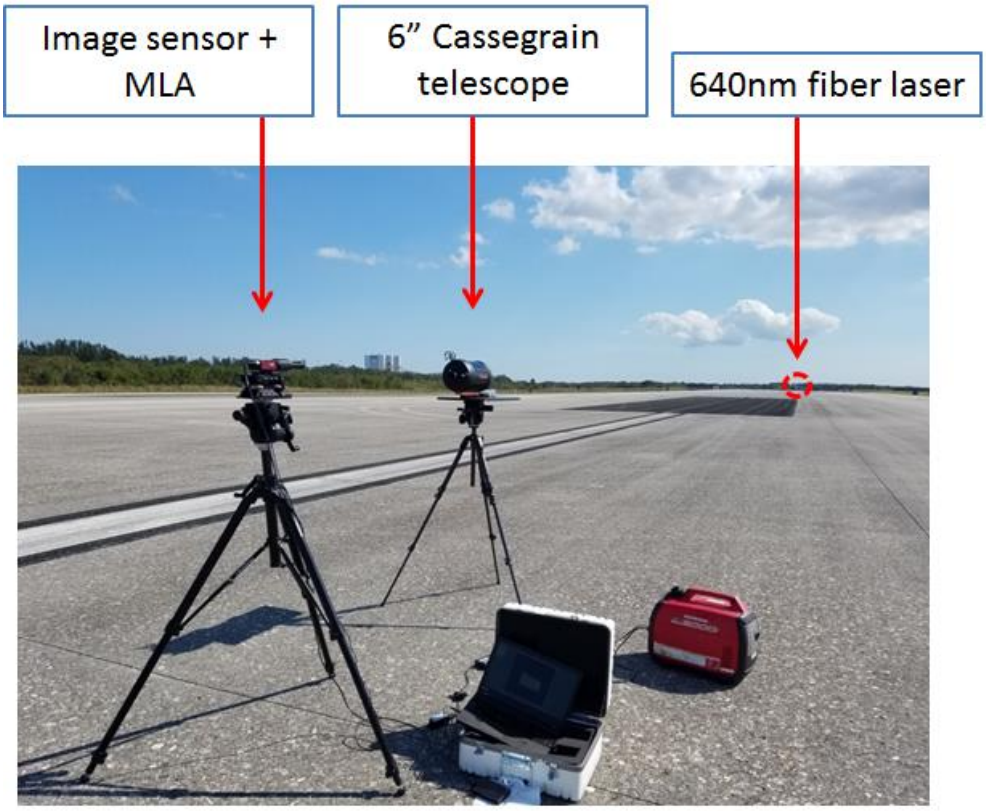

Figure 3.3.2: Plenoptic Sensor testing on SLF.

Figure 3.3.2 shows the Plenoptic Sensor on the SLF. The transmitting laser is a collimated 640 nm Coherent fiber laser outputting 25 mW and is located at the south end of the SLF. The transmitting laser and the Plenoptic Sensor are separated by 850 m. The Plenoptic Sensor and data acquisition laptop are both powered by a Honda EU2000i gasoline generator.

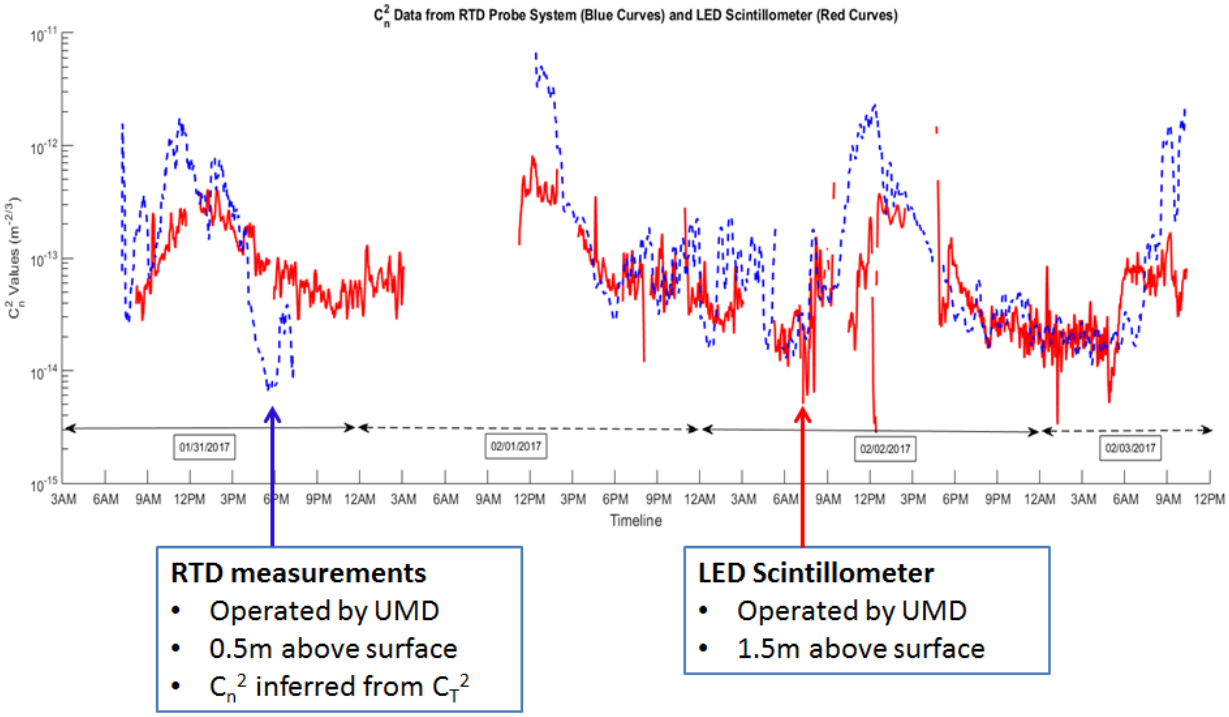

Figure 3.3.3: RTD and LED scintillometer results.

Figure 3.3.3 shows data collected by the MOG LED Scintillometer and the MOG RTD C_T^2 device. The data stretched a span of almost 4 days and included 24 hour data collection except in situations where equipment was moved or there were other interfering issues. For example, large spikes in the C_n^2 data later in the week from the LED scintillometer were mainly due to interference from a nearby laser scintillometer. Despite these issues, the LED Scintillometer and RTD C_T^2 device showed similar trends in turbulence strength throughout the week. Both devices were capable of reliably logging C_n^2 data without constant monitoring and recalibration.

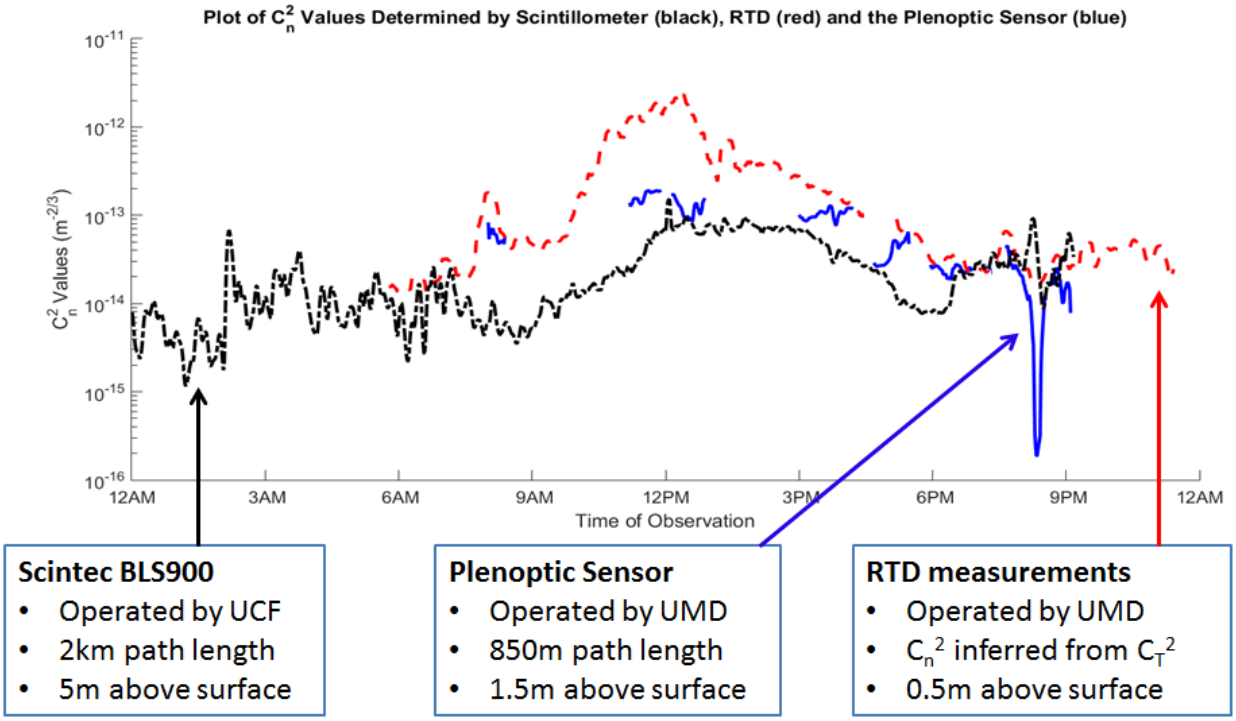

Figure 3.3.4: Comparison of C_n^2 data from 2/2/2017.

Figure 3.3.4 shows C_n^2 data from 2/2/2017 which is the only day the Plenoptic Sensor was able to be set up for long term data collection. In Figure 3.3.4, C_n^2 data from the Plenoptic Sensor, the RTD C_T^2 device and the Scintec BLS900 is displayed. The BLS900 was the only device operating much higher above the surface of the SLF but still showed C_n^2 values that were comparable in magnitude to the Plenoptic Sensor. The RTD device recorded higher C_n^2 values during the peak of the afternoon heat compared to the BLS900 and the Plenoptic Sensor but recorded similar C_n^2 values during the low turbulence parts of the day. Part of the reason for the high readings during the afternoon can be attributed to the very close proximity to the ground (only 0.5 m above the SLF surface) which results in much more significant temperature fluctuations.

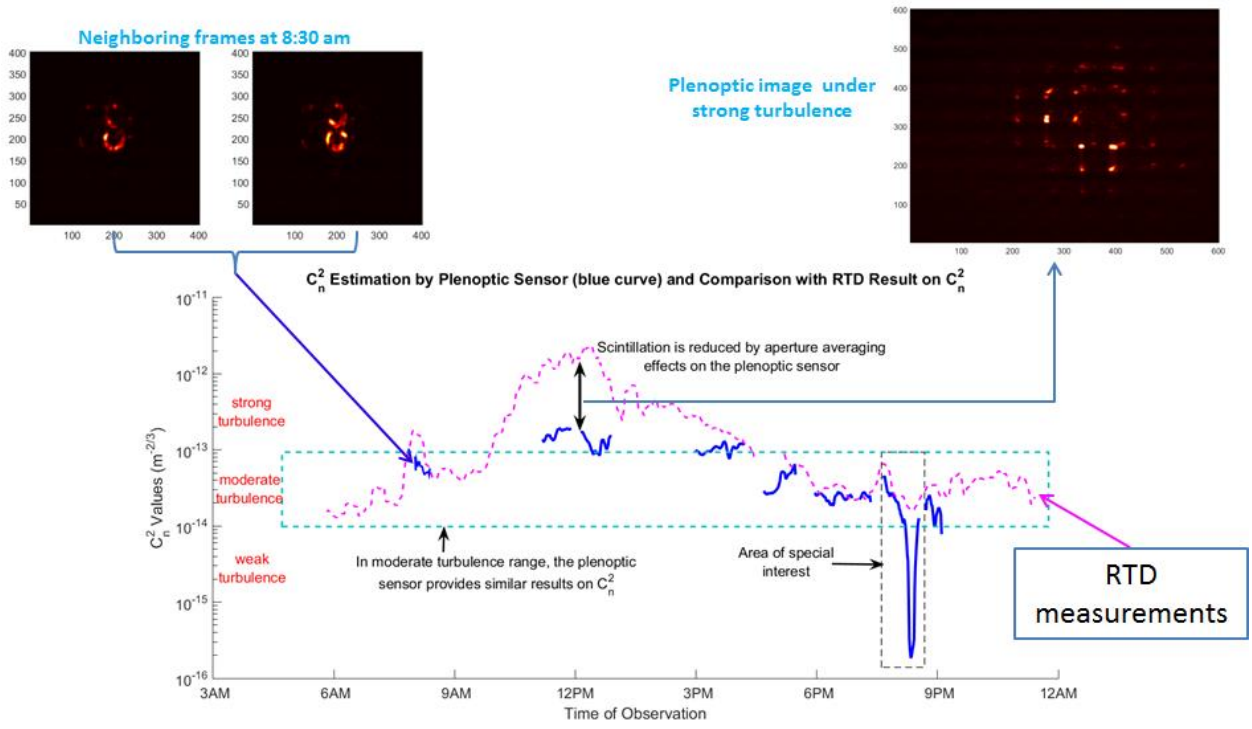

Figure 3.3.5: Plenoptic Sensor C_n^2 data from 2/2/2017.

In Figure 3.3.5 we examine the Plenoptic Sensor C_n^2 data and RTD C_n^2 data in more detail. The 2 Plenoptic images shown from 8:30 am give a visual representation of the wavefront distortions present during moderate turbulence conditions. As expected, most of the intensity remains focused in a minimal number of the Plenoptic Sensor's MLA sub-apertures. In addition, both of the 8:30 am Plenoptic images are visibly similar which is indicative of lower scintillation values. In contrast, the Plenoptic image from around 12 pm shows many MLA sub-apertures illuminated. The Plenoptic images from around that time are very different between neighboring frames which corresponds to higher scintillation values.

Also, in Figure 3.3.5 there is a noticeably large dip in the Plenoptic Sensor C_n^2 data around 8:20 pm. This is interesting because 8:30 pm is generally a few hours after the normal C_n^2 diurnal dip that occurs around sunset. Figure 3.3.6 below takes a closer look at this area of interest.

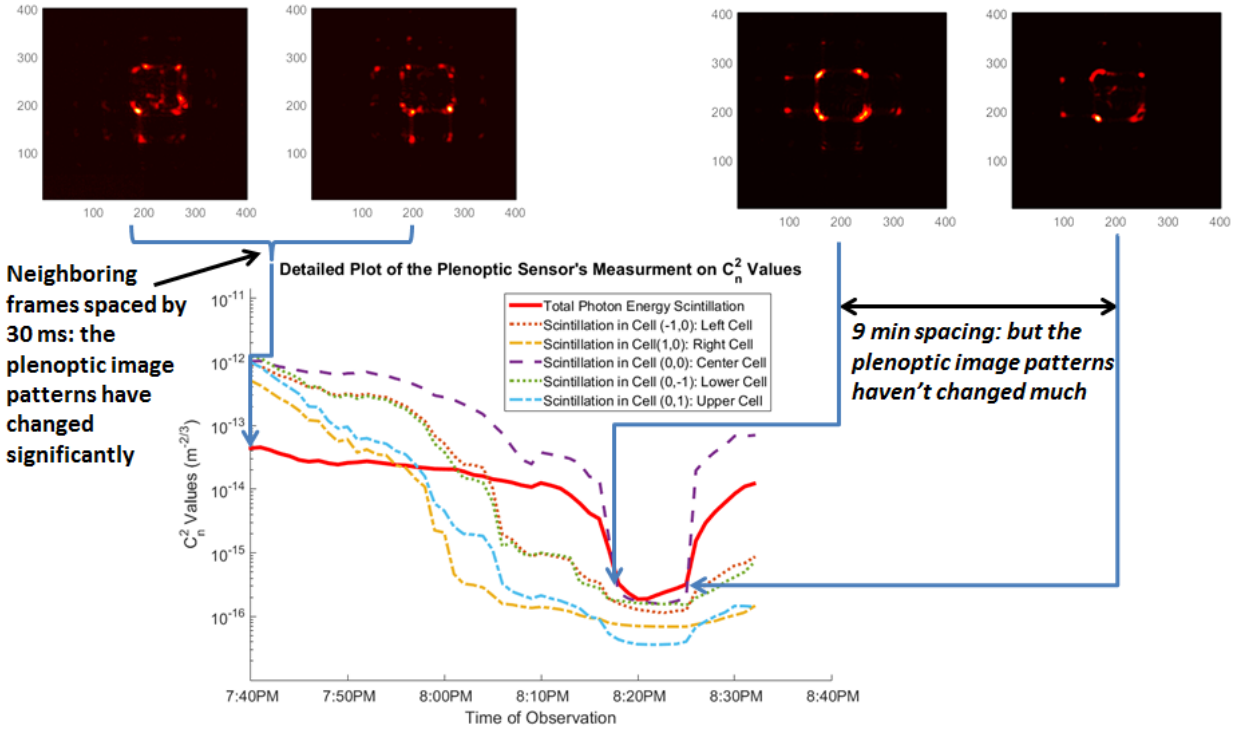

Figure 3.3.6: Closer look at Plenoptic Sensor C_n^2 data at 8:20 pm.

The first two Plenoptic images on the left side of Figure 3.3.6 are taken around 7:40 pm during the moderate turbulence conditions that occur after the C_n^2 diurnal dip. As expected, the variation between the Plenoptic images at 7:40 pm is rather significant which leads to higher C_n^2 values. In comparison, the two Plenoptic images on the right side of Figure 3.3.6 are extremely similar despite being taken over 9 minutes apart. This abnormal "quiet window" of atmospheric turbulence was also confirmed by the C_n^2 dips from the BLS900 and RTD C_T^2 device. Situations like this

do not commonly arise during this part of the day and present a “lucky” period of time in which long range laser propagation can occur without needing significant wavefront correction from adaptive optics. In addition, the graph in Figure 3.3.6 demonstrates aperture averaging in effect on the Plenoptic Sensor. The graph has a solid red line for the overall C_n^2 value calculated by the Plenoptic Sensor, and also other colored dotted lines for individual C_n^2 values calculated by individual sub-apertures. The aperture averaging effect can clearly be seen because the overall C_n^2 value only drops by two orders of magnitude in the same period of time that the individual C_n^2 values for each MLA sub-aperture drop up to four orders of magnitude. This aperture averaging effect allows the Plenoptic Sensor to perform C_n^2 measurements in a wide range of turbulence conditions without the risk of saturation effects.

4) Conclusions

Atmospheric characterization is of great importance to many fields. Evaluating the strength of atmospheric turbulence is crucial in determining what steps must be employed to counteract its negative effects. For example, conventional wavefront sensors and "lucky imaging" techniques are effective tools when dealing with weak atmospheric turbulence but their effectiveness dwindles as the atmospheric turbulence enters the strong regime. We have developed and field tested a large aperture LED scintillometer and an RTD C_T^2 device. Both devices have shown that they can produce accurate C_n^2 readings when compared to commercially available scintillometers. The Plenoptic Sensor is also able to calculate C_n^2 readings and provides an even deeper information set that allows for separate C_n^2 readings in 2 dimensions. In addition, a transmissometer has been developed and is useful in determining the atmospheric attenuation coefficient.

The Plenoptic Sensor's usage goes further beyond atmospheric characterization. The Plenoptic Sensor is able to provide wavefront information in strong turbulence conditions. In strong turbulence conditions, the wavefront often consists of intensity nulls and overlapping patches of light, both of which cannot be correctly identified and reconstructed in a Shack-Hartmann sensor. The Plenoptic Sensor provides an approach to wavefront sensing in these strong turbulence conditions due to its resistance against strong scintillation effects and other self-interference effects in the distorted wavefront.

Future efforts have been planned in the characterization of the atmosphere. An improved RTD C_T^2 device can be developed with finer temperature resolution in order

to improve C_n^2 characterization in the low turbulence regime. In addition, a new transmissometer is being developed which doesn't require a large collection aperture capable of collecting the entire beam on the receiver end. Instead, multiple point detectors are used to fit a beam to its Gaussian shape and then extract the received intensity information from the fitting. This allows for use at much greater distances as well as in strong turbulence conditions where the beam becomes very large and it becomes not physically feasible to have an equally as large receiving aperture.

Future work is also possible in the correction of atmospheric turbulence. Although the adaptive optics system utilizing the Plenoptic Sensor has been effective in lab based strong turbulence environments, the system hasn't yet been tested in outdoor atmospheric turbulence. Several steps must be completed prior to that happening. FPGA implementation is being developed to break the 250 Hz closed-loop wavefront correction speed that is currently limited by computing power. In addition, a proper weatherized enclosure must be developed to protect the deformable mirror membrane from being damaged by outdoor effects such as heat and humidity. An outdoor demonstration of the adaptive optics system utilizing the Plenoptic Sensor will hopefully present a new angle towards wavefront reconstruction and correction in strong atmospheric turbulence.

Bibliography

[1] R. K. Tyson, Principles of Adaptive Optics, 3rd ed., Optics and Optoelectronics (CRC Press, 2011).

[2] L. C. Andrews and R. L. Phillips, *Laser Beam Propagation through Random Media*, 2nd ed. (SPIE, 2005).

[3] J. C. Wyngaard and S. F. Clifford, “Taylor’s hypothesis and high-frequency turbulence spectra,” J. Atmos. Sci. 34(6), 922–929 (1977).

[4] L. C. Andrews, R. L. Phillips, C. Y. Hopen, and M. A. Al-Habash, "Theory of optical scintillation," J. Opt. Soc. Am. A 16, 1417-1429 (1999).

[5] R. J. Hill and G. R. Ochs, "Fine calibration of large-aperture optical scintillometers and an optical estimate of inner scale of turbulence," Appl. Opt. 17, 3608-3612 (1978)

[6] Chehbouni, A., C. Watts, J-P. Lagouarde, Y. H. Kerr, J-C. Rodriguez, J-M. Bonnefond, F. Santiago, G. Dedieu, D. C. Goodrich, and C. Unkrich. "Estimation of heat and momentum fluxes over complex terrain using a large aperture scintillometer." Agricultural and Forest Meteorology 105, no. 1 (2000): 215-226.

[7] R. J. Hill, "Saturation resistance and inner-scale resistance of a large-aperture scintillometer: a case study," Appl. Opt. 20, 3822-3824 (1981)

[8] L. C. Andrews, R. L. Phillips, R. J. Sasiela, and R. R. Parenti, “Strehl ratio and scintillation theory for uplink Gaussian-beam waves: beam wander effects,” Opt. Eng. 45, 076001 (2006).

[9] T. Adelson and J. Y. A. Wang, “Single lens stereo with a plenoptic camera.” IEEE Transactions on Pattern Analysis and Machine Intelligence 14, 2 (1992), 99–106.

[10] M. Levoy and P. Hanrahan, “Lightfield rendering,” in Proceedings of ACM SIGGRAPH (1996).

[11] R. Ng, M. Levoy, M. Bredif, G. Duval, M. Horowitz, and P. Hanraham, "Light field photography with a hand-held plenoptic camera" Stanford Tech Report CTSR 2005-02 (2005).

[12] Christopher Hahne, Amar Aggoun, Vladan Velisavljevic, Susanne Fiebig, and Matthias Pesch, "Refocusing distance of a standard plenoptic camera," Opt. Express 24, 21521-21540 (2016).

[13] T. Georgeiv, K. C. Zheng, B. Curless, D. Salesin, S. Nayar, and C. Intwala, “Spatio-angular resolution tradeoff in integral photography,” in Proceedings of Eurographics Symposium on Rendering, (2006), pp. 263–272.

[14] A. Lumsdaine and T. Georgiev, "The focused plenoptic camera," 2009 IEEE International Conference on Computational Photography (ICCP), San Francisco, CA, (2009), pp. 1-8.

[15] J. Rodríguez-Ramos, et al. "Wavefront and distance measurement using the CAFADIS camera." SPIE Astronomical Telescopes+ Instrumentation. International Society for Optics and Photonics, (2008).

[16] P. Jiang, J Xu, Y. Liang, and H Mao, “Comparison of the shack–hartmann and plenoptic sensor in closed-loop adaptive optics system,” Opt. Eng. (2016).

[17] C. Wu, J. Ko, and C. C. Davis, “Plenoptic mapping for imaging and retrieval of the complex field amplitude of a laser beam,” Opt. Express 24, 29852–29871 (2016).

[18] C. Wu, J. Ko, and C. C. Davis, “Determining the phase and amplitude distortion of a wavefront using a plenoptic sensor,” J. Opt. Soc. Am. A 32, 964–978 (2015).

[19] J. Goodman, “Wave-optics analysis of coherent optical systems,” in Introduction to Fourier Optics, 2nd ed. (McGraw-Hill, 1996), pp. 101–107.

[20] J. Ko, C. Wu, and C. C. Davis, “An adaptive optics approach for laser beam correction in turbulence utilizing a modified plenoptic camera,” Proc. SPIE 9614, 96140I (2015).

[21] W. H. Southwell, “Wave-front estimation from wave-front slope measurements,” J. Opt. Soc. Am. 70, 998–1006 (1980).

[22] B. C. Platt and R. Shack, “History and principles of Shack–Hartmann wavefront sensing,” J. Refractive Surg. 17, S573–S577 (2001).

[23] D. L. Fried and J. L. Vaughn, “Branch cuts in the phase function,” Appl. Opt. 31, 2865–2882 (1992).

[24] A. Agrawal, R. Chellappa, and R. Raskar, “An algebraic approach to surface reconstruction from gradient fields,” IEEE International Conference on Computer Vision, (2005).

[25] J. Ko, C. Wu, and C. C. Davis, “Implementation of a rapid correction algorithm for adaptive optics using a plenoptic sensor,” Proc. SPIE 9979, 99790O (2016).

[26] D. G. Sandler, J. R. P. Angel, M. Lloyd-Hart, S. Stahl, and D. McCarthy, "Adaptive optics for diffraction-limited infrared imaging with 8-m telescopes," J. Opt. Soc. Am. A 11, 925-945 (1994).

[27] M. Nicolle, T. Fusco, G. Rousset, and V. Michau, "Improvement of Shack–Hartmann wave-front sensor measurement for extreme adaptive optics," Opt. Lett. 29, 2743-2745 (2004).

[28] Olivier Lardière, Rodolphe Conan, Richard Clare, Colin Bradley, and Norbert Hubin, "Performance comparison of centroiding algorithms for laser guide star wavefront sensing with extremely large telescopes," Appl. Opt. 49, G78-G94 (2010).

[29] Junzhong Liang, Bernhard Grimm, Stefan Goelz, and Josef F. Bille, "Objective measurement of wave aberrations of the human eye with the use of a Hartmann–Shack wave-front sensor," J. Opt. Soc. Am. A 11, 1949-1957 (1994).

[30] Pedro M. Prieto, Fernando Vargas-Martín, Stefan Goelz, and Pablo Artal, "Analysis of the performance of the Hartmann–Shack sensor in the human eye," J. Opt. Soc. Am. A 17, 1388-1398 (2000).

[31] Thomas O. Salmon, Larry N. Thibos, and Arthur Bradley, "Comparison of the eye's wave-front aberration measured psychophysically and with the Shack–Hartmann wave-front sensor," J. Opt. Soc. Am. A 15, 2457-2465 (1998).

[32] J. D. Barchers, D. L. Fried, and D. J. Link, "Evaluation of the performance of Hartmann sensors in strong scintillation," Appl. Opt. 41, 1012–1021 (2002).

[33] D. L. Fried, "Branch point problem in adaptive optics," J. Opt. Soc. Am. A 15, 2759–2768 (1998).

[34] D. L. Fried, "Adaptive optics wave function reconstruction and phase unwrapping when branch points are present," Opt. Commun. 200, 43–72 (2001).

[35] K. Murphy, D. Burke, N. Devaney, and C. Dainty, "Experimental detection of optical vortices with a Shack–Hartmann wavefront sensor," Opt. Express 18, 15448–15460 (2010).

[36] C. Wu, J. Ko, and C. C. Davis, "Using a plenoptic sensor to reconstruct vortex phase structures," Opt. Lett. 41, 3169–3172 (2016).

[37] V. V. Voitsekhovich, D. Kouznetsov, and D. K. Morozov, "Density of turbulence-induced phase dislocations," Appl. Opt. 37, 4525–4535 (1998).

[38] K. Murphy and C. Dainty, "Comparison of optical vortex detection methods for use with a Shack–Hartmann wavefront sensor," Opt. Express 20, 4988–5002 (2012).

[39] A. Mobashery, M. Hajimahmoodzadeh, and H. R. Fallah, “Detection and characterization of an optical vortex by the branch point potential method: analytical and simulation results,” Appl. Opt. 54, 4732–4739 (2015).

[40] D. C. Ghiglia and M. D. Pritt, Two-Dimensional Phase Unwrapping: Theory, Algorithms, and Software (Wiley, 1998).

[41] F. A. Starikov, G. G. Kochemasov, S. M. Kulikov, A. N. Manachinsky, N. V. Maslov, A. V. Ogorodnikov, S. A. Sukharev, V. P. Aksenov, I. V. Izmailov, F. Y. Kanev, V. V. Atuchin, and I. S. Soldatenkov, “Wavefront reconstruction of an optical vortex by a Hartmann-Shack sensor,” Opt. Lett. 32, 2291–2293 (2007).

[42] K. L. Baker and M. M. Moallem, “Iteratively weighted centroiding for Shack–Hartmann wave-front sensors,” Opt. Express 15, 5147–5159 (2007).

[43] C. Leroux and C. Dainty, “Estimation of centroid positions with a matched-filter algorithm: relevance for aberrometry of the eye,” Opt. Express 18, 1197–1206 (2010).

[44] J. Pfund, N. Lindlein, and J. Schwider, “Dynamic range expansion of a Shack–Hartmann sensor by use of a modified unwrapping algorithm,” Opt. Lett. 23, 995–997 (1998).

[45] L. C. Andrews, R. L. Phillips, and C. Y. Hopen, *Laser Beam Scintillation with Applications* (SPIE Press, 2010).

[46] H. Song, G. Vdovin, R. Fraanje, G. Schitter, and M. Verhaegen, "Extracting hysteresis from nonlinear measurement of wavefront-sensorless adaptive optics system," Opt. Lett. 34, 61-63 (2009).

[47] Ariel Cohen, "Horizontal visibility and the measurement of atmospheric optical depth of lidar," Appl. Opt. 14, 2878-2882 (1975)

[48] Jonathan Ko and Christopher C. Davis, "Comparison of the plenoptic sensor and the Shack- Hartmann Sensor," Appl. Opt. 56, 3689-3698 (2017).